Scuola Internazionale Superiore di Studi Avanzati

PhD course in Theory and Numerical Simulation of Condensed Matter

Ab-initio Characterization of a Novel Photocathode for Water Splitting: Bulk and Surface Properties of $CuFeO_2$

A thesis submitted for the degree of *Doctor Philosophiæ*

Candidate
Matteo Ferri

Supervisors
Dr. Simone Piccinin
Dr. Stefano Fabris
Prof. Stefano De Gironcoli

September 2020

List of publications

The main outcomes of this thesis have been published in the following articles:

[1] Matteo Ferri, Joshua Elliott, Matteo Farnesi Camellone, Stefano Fabris and Simone Piccinin, "Thermodynamic Stability and Native Point Defects of $CuFeO_2$ Photocathodes in Dry and Electrochemical Environments". *The Journal of Physical Chemistry C* **123** (49), 29589-29598 (2019)

[2] Matteo Ferri, Joshua Elliott, Stefano Fabris and Simone Piccinin, "Establishing best practices to model the electronic structure of $CuFeO_2$ from first principles". *Physical Review B* **101** (15), 155201 (2020)

Matteo Ferri, Joshua Elliott, Matteo Farnesi Camellone, Stefano Fabris and Simone Piccinin, "First-principles modeling of the interface between $CuFeO_2$ photocathode surfaces and water: Structure and catalytic activity for hydrogen evolution". *Ready for submission*

Acknowledgements

We acknowledge the CINECA award under the ISCRA initiative, for the availability of high performance computing resources and support. Most of the calculations of this work were performed under the ISCRA B projects PHOTOSOL and CUPHERO.

Personally, I want to thank Simone and Stefano for giving me the opportunity to work with them on this stimulating project. I learned many things from the conversation with them during these years. The contribution of Josh and Matteo in this work is also highly appreciated.

I had a great time during these four years in Trieste. I will not mention all the people one by one, but I want to thank anyone who contributed to these good moments, both in SISSA and outside.

Finally, I want to thank my parents for the support and Francesca for the continuous love and care.

Contents

1

Introduction

The critical global climate change situation is stimulating a very active research into renewable energy technologies in a bid to limit CO_2 and other greenhouse gases emissions. The global need for energy is expected to double by 2050 and triple by the end of the century and the existing carbon-based fuels do not allow to supply the demand in a sustainable way [3]. The urgent need to transition from fossil fuels to renewable energy sources to reach a sustainable carbon-neutral society is driving several avenues of intense research.

Solar energy is an inexhaustible natural resource, one of the most promising among of all carbon-neutral energy sources. The amount of energy from sunlight striking the Earth in one hour ($4.3 \cdot 10^{20}$ J) would supply the energy demanded by the planet in one year ($\sim 4.1 \cdot 10^{20}$ J) [3]. Solar energy can be converted into electricity (photovoltaics), thermal energy or chemical fuels. The harnessing of solar radiation via photoelectrochemical (PEC) conversion and its use within the energy sector is one example of a strategy that could reduce carbon consumption, thereby limiting CO_2 production.

PEC cells [4] offer the possibility to convert sunlight into chemical fuels, mimicking the natural process of photosynthesis. While in the natural photosynthesis the energy of the sunlight is used to convert carbon dioxide and water into sugars and oxygen, the application of PEC cells for water splitting enables the conversion and storage of solar radiation within the chemical bonds of the molecular oxygen and hydrogen. In particular, hydrogen is nonpolluting, renewable, inexhaustible, and very flexible with respect to conversion to other forms of energy [5]. Hydrogen can be employed in fuel cells to produce electricity, heat and water with potential use in a vast range of applications, from the industrial to the field of transportation.

Similarly to traditional electrochemical devices, water splitting PEC cells are composed of two electrodes immersed in an aqueous electrolyte and a membrane to separate the products of the two half-cell reactions, with the difference that, in PEC cells, at least one of the two electrodes is able to absorb solar radiation and generate electron-hole pairs. The photogenerated charge carriers are then transported towards the surface of

the anode and the cathode, where the holes oxidize H_2O molecules producing O_2 and releasing protons in solution, while electrons reduce protons to H_2, respectively.

The feasibility of using PEC cells on a large scale requires efficient and stable catalysts for which transition metal oxides would be the ideal candidates. However, each step of the overall process, namely absorption, transport and catalysis, introduces very specific constraints that are difficult to fulfil in a single material. The availability of Earth-abundant semiconducting photoelectrode materials increases the flexibility in the design of PEC cells by incorporating photoactive *n*-type and *p*-type materials for the anode and cathode, respectively. While a large number of *n*-type semiconductors have been largely characterized as photoanodes, comparatively very little work has been done on *p*-type photocathodes.

Among the class of Cu(I)-oxides, recent PEC measurements have highlighted the delafossite $CuFeO_2$ as a promising candidate in the role of the photocathode [6, 7]. Despite the encouraging favorable properties, the maximum photocurrent densities measured in $CuFeO_2$ photocathodes is one order of magnitude lower than the theoretical limit [8, 9]. There are conflicting explanations for the relatively poor PEC performance, which is attributed to both bulk recombination [10] and Fermi-level pinning at the solid-liquid interface [11, 12].

Beside these experimental works, there is not a solid theoretical literature to provide a complete picture. Given the increasing complexity of PEC devices, understanding the interplay between the electronic structure, surface dynamics and structure of the surface-solvent interface is pivotal for the prediction of the performance of a material as a photoelectrode. Theoretical and computational investigations provide the atomistic insight required to understand these features and complement experiments. Systematic advances in hardware and software engineering, along with developments in sophisticated theoretical models have led to an increasing use of computational tools in materials science. Most of them are based on density functional theory (DFT), which has become well suited for the study of complex PEC interfaces.

The aim of this thesis is to adopt the tools provided by DFT to perform a full theoretical characterization of the bulk and surface properties of CFO, in order to provide new insight and facilitate further investigations of this material.

We first benchmarked our theoretical predictions against experimentally known quantities, in order to establish the strength and limitations of our models and understand how to use them properly to predict with a good level of confidence quantities that are difficult to achieve experimentally. After a complete bulk characterization, we

performed the first *ab-initio* static and dynamic simulations of CFO surfaces, both in vacuum and in contact with the electrolyte.

This thesis is organized as follows: we introduce the water splitting reaction and the underlying physics and chemistry in Chapter 2. In Chapter 3 we briefly review the most commonly used photoelectrodes materials, focusing specifically on $CuFeO_2$. In Chapter 4, we describe the computational methods adopted in this work, starting from DFT. The characterization of the electronic structure of the bulk $CuFeO_2$ is reported in Chapter 5, while its thermodynamic stability in Chapter 6. These two chapters are largely taken from our published works [1, 2]. In Chapter 7 we discuss the thermodynamic stability of $CuFeO_2$ surfaces and the band alignment in dark conditions and under illumination. Finally, the conclusion and perspectives are discussed in Chapter 8

2

Photoelectrochemistry

CONTENTS

Photoelectrochemistry is the branch of the physical chemistry which studies reactions involving charge transfer processes, and hence current flows, across the solid-liquid interface under illumination. The first PEC experiment in the history was performed in 1839 by Becquerel, who observed a voltage and an electric current on an illuminated silver chloride electrode immersed in an electrolytic solution and connected to a counter electrode [13]. However, the origin of this phenomenon had remained unknown for more than a century, until the work of Brattain and Garrett on germanium electrodes [14], which opened the way for the study of the semiconductor photoelectrochemistry [15]. In 1972 Fujishima and Honda showed the possibility of splitting water into hydrogen and oxygen using an illuminated TiO_2-electrolyte junction [16]. This work has generated a growing interest in solar water splitting as an alternative and sustainable energy source, especially after the 1973 oil crisis [17]. Despite the initial enthusiasm, researchers encountered several difficulties in building stable, efficient electrodes at a competitive cost. A breakthrough occurred with the advent of nanostructured electrodes and dye-sensitized solar cells in the early 90s [18]. This discovery has rekindled interest in the study of water splitting tandem cells, towards the research for new nanostructured materials for both the anodic and cathodic processes.

In this chapter we will explain the functioning of a cell, focusing on the mechanisms that underlie the operation.

2.1 Water splitting reaction

The solar water splitting reaction consists in breaking down two water molecules into one oxygen and two hydrogen molecules using the energy of photons from sunlight:

$$2H_2O \xrightarrow{h\nu} O_2 + 2H_2\,. \tag{2.1}$$

The free energy change for this reaction at standard conditions is 4.92 eV [19]. In the PEC water splitting, the overall reaction occurs through two different redox half-reactions, namely the oxygen evolution reaction (OER):

$$\text{OER}: \quad 2H_2O + 4h^+ \rightarrow O_2 + 4H^+\,, \tag{2.2}$$

in which gaseous oxygen is formed and protons are released into the solution, and the hydrogen evolution reaction (HER) for the hydrogen production:

$$\text{HER}: \quad 2H^+ + 2e^- \rightarrow H_2\,. \tag{2.3}$$

At the most basic level, a PEC water splitting device is composed of an electrolyte and two electrodes, where the two electrochemical half-reactions take place. In particular, at the anodic surface-solute interface, photogenerated holes drive the OER, while at the cathode, the electrons are consumed during the HER.

Eq.(2.2) and (2.3) represent the overall OER and HER, which are multi-step processes. Different mechanisms based on kinetic studies or DFT calculations have been proposed for the OER [20]. One of the most widely used, and computationally easy to treat, is the following four-step process, in which each step is a proton-coupled electron transfer (PCET) process:

$$2\,H_2O + \star + h^+ \rightarrow OH^* + H_2O + H^+ \quad , \tag{2.4}$$

$$OH^* + H_2O + h^+ \rightarrow O^* + H_2O + H^+ \quad , \tag{2.5}$$

$$O^* + H_2O + h^+ \rightarrow OOH^* + H^+ \quad , \tag{2.6}$$

$$OOH^* + h^+ \rightarrow O_2 + H^+ \quad , \tag{2.7}$$

where $\star$ represents an active site on the surface with possible adsorbed species, indicated, for instance, as OH^*. The reactions written above describe the processes that constitute the OER in an acidic solution. However, the vast majority of the OER electrocatalysts are chemically unstable in acidic media. Iridium oxide IrO_2 is an exception, being stable and highly active in acidic environment [21]. PbO_2 is stable at low pH, but with a limited

activity. A Co-Pi catalyst operating at neutral pH was also reported [22]. The OER steps written above take the following form in alkaline media:

$$\mathrm{OH^-} + \star + h^+ \rightarrow \mathrm{OH^*} \quad , \tag{2.8}$$

$$\mathrm{OH^*} + \mathrm{OH^-} + h^+ \rightarrow \mathrm{O^*} + \mathrm{H_2O} \quad , \tag{2.9}$$

$$\mathrm{O^*} + \mathrm{OH^-} + h^+ \rightarrow \mathrm{OOH^*} \quad , \tag{2.10}$$

$$\mathrm{OOH^*} + \mathrm{OH^-} + h^+ \rightarrow \mathrm{O_2} + \mathrm{H_2O} \quad . \tag{2.11}$$

Two mechanisms have been proposed to model the HER, namely the Volmer-Tafel or the Volmer-Heyrovsky steps. The Volmer step consists in an electrochemical hydrogen adsorption on the surface of the cathode, mediated by an electron in the conduction band:

$$\mathrm{H^+_{aq}} + \star + e^- \rightarrow \mathrm{H^*} + \mathrm{H_2O} \qquad \text{(acidic solution)}, \tag{2.12}$$

$$\mathrm{H_2O} + \star + e^- \rightarrow \mathrm{H^*} + \mathrm{OH^-} \qquad \text{(alkaline solution)}. \tag{2.13}$$

In acidic conditions, the Volmer step occurs via the discharge of a solvated proton and the subsequent adsorption on the catalyst surface. The simplest model of a solvated proton is an hydronium ion $\mathrm{H_3O^+}$, which however, can have a complicated solvation shell. Other well-known structures are the Zundel ($\mathrm{H_5O_2^+}$) or Eigen ($\mathrm{H_9O_4^+}$) cations.

Conversely, in alkaline conditions, the Volmer step involves the adsorption and dissociation of a water molecule on the surface, forming a $\mathrm{H^*}$ and releasing an $\mathrm{OH^-}$ [23]. The adsorbed hydrogen atoms are then desorbed chemically (Tafel) or electrochemically (Heyrovsky) to form $\mathrm{H_2}$. The Tafel step consists in a desorption of two $\mathrm{H^*}$ from the surface and it is independent on the pH of the solution:

$$2\mathrm{H^*} \rightarrow \mathrm{H_2} + 2\star \tag{2.14}$$

In the Heyrovsky mechanism the adsorbed hydrogen desorbs from the surface, combining with a solvated proton (in acidic solutions) or a hydrogen atom from water (in alkaline solutions) to form $\mathrm{H_2}$:

$$\mathrm{H^*} + \mathrm{H^+_{aq}} + e^- \rightarrow \star + \mathrm{H_2} \qquad \text{(acidic solution)}, \tag{2.15}$$

$$\mathrm{H^*} + \mathrm{H_2O} + e^- \rightarrow \star + \mathrm{H_2} + \mathrm{OH^-} \qquad \text{(alkaline solution)}. \tag{2.16}$$

Therefore, the overall (photo)electrochemical water splitting can be conducted in both acidic and alkaline solutions, following different mechanism both for OER and for HER. However, both of them show important drawbacks. Indeed, the acidic HER is usually limited by the poor stability of the catalyst [24], while the alkaline HER suffers from a sluggish kinetics [25].

2.2 Photoelectrochemical cells

The simplest PEC device is composed of a single absorber material, acting as the photoanode, in conjunction with a metal cathode, which is in general a platinum electrode, considered the most effective electrocatalyst for HER. When the photoanode material is exposed to sunlight, the incident photons with energy higher than the bandgap can generate electron-hole pairs, upon the absorption. The charge carriers are physically and energetically separated by the electric field generated at the interface when the semiconductor is put in contact with the electrolyte. While the photogenerated electrons in the conduction band travel towards the cathode to participate to the reaction (2.3), at the photoanode the holes drift to the surface to oxidize water into O_2, according to the reaction (2.2).

Even the most basic single-absorber PEC cell rests on the simultaneous fulfillment of several interconnected criteria [5]. First of all, to ensure an optimal absorption of photons, the photoanode must absorb light in a wavelength region that overlaps the solar spectrum, in particular the sun-radiance peak [26]. While the photogenerated charge carriers travel towards the surfaces, recombination events must be minimized in order to bring the maximum number of carriers to the surface. Once on the surface, the charge carriers must have enough energy to drive the two half-reactions, that means that the position of the valence and conduction bands must straddle the redox potentials of water. The implication is threefold: i) the optical gap must be larger than 1.23 eV, ii) the energy of the valence band maximum (VBM), E_{VBM} must be below the OER redox potential and iii) the energy of the conduction band minimum (CBM), E_{CBM}, must be higher than the HER redox potential. Even stricter requirements must be satisfied if we consider the overpotential needed to drive both the anodic and the cathodic reactions. The material should also promote the reactivity at the surfaces, allowing a rapid charge transfer at the interface with water. Finally, to reduce the costs of production, the electrodes should be composed of Earth-abundant materials which must be stable under aqueous conditions to guarantee the longevity of the electrode.

The simultaneous fulfillment of these requirements within a single semiconductor has proven elusive [28, 29], even half-a-century after the pioneering work of Honda and Fujishima on TiO_2 [16]. However, these constraints can be relaxed in a tandem cell, which is composed of two light absorbing, semiconducting electrodes: an n-type material is used for the photoanode and a p-type for the photocathode, as it is shown in Figure 2.1, taken from Ref.[27]. In such a setup, the material for each electrode can

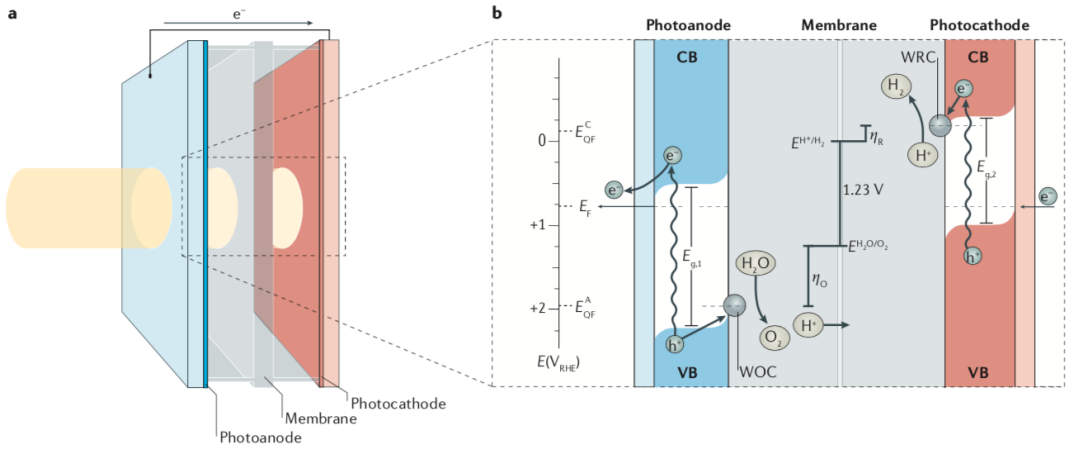

Figure 2.1

Schematic view (a) and energetics (b) of a tandem cell with two semiconductors with bandgap E_{g1} and E_{g2} under illumination. WOC (WRC) and η_O (η_R) are the water oxidation (reduction) catalysis site and the overpotential for oxidation (reduction), respectively. Figure taken from Ref.[27].

be optimally selected, with the band edges aligned to only one of the two coupled redox reactions and can absorb light at any frequency coincidental with the range spanned by solar radiation. These advantages have translated into improved performances, with experimental reports of higher photoconversion efficiencies when compared with single absorber cells [19, 27, 30].

2.3 Semiconductor-Liquid junction

A key aspect of PEC devices is the energetic and spatial separation of the charge-carriers, which is driven by the band bending at the semiconductor-liquid junction (SLJ) [4, 19, 31]. The SLJ is similar to a rectifying metal-semiconductor Schottky junction, in which an electric field separates the photogenerated charge carriers and the minority carriers move towards the surface. Analogously, the contact between a semiconductor and an electrolyte containing a redox couple generates a charge transfer across the junction until electronic equilibrium is established, i.e. when the electrochemical potential of the electron in the semiconductor (Fermi level) is aligned with the electrochemical potential of the redox couple [17]. As a result, the regions close to the interface lose their charge

neutrality, forming the so-called space charge layer. As a consequence of the semiconductor surface being charged, a double layer forms in the electrolyte, composed of a narrow ($0.4 - 0.6$ nm) layer of ions close to surface (Helmholtz layer) and a region of diffuse ions in the solution (Gouy–Chapman layer).

In the semiconductor, the charge transfer creates a region close to the interface with a depletion of the majority charge carriers, whose dimension W depends on several factors:

$$W = \left[\frac{2\epsilon}{qN_D} V_{bi}\right]^{\frac{1}{2}} \quad . \tag{2.17}$$

Here, ϵ is the dielectric constant of the semiconductor, q the elementary charge, N_D is the concentration of dopants in the semiconductor and V_{bi} is the built-in potential, which corresponds to the difference between the Fermi level in the semiconductor and the redox potential in the solution before contact. An electric field is generated inside the depletion region and the associated potential has the effect of bending the electronic bands. The difference between the energy of the bands at the interface and in the bulk region, V_{SC}, is equal to the built-in potential V_{bi}. The direction of the band bending depends on the position of the Fermi level in the material, as it is schematically represented in Figure 2.2.

An n-type semiconductor is required for an upward bending of the valence and the conduction band, to provide an energetic drive for the migration of the photogenerated holes towards the interface encouraging reaction (2.2). Conversely, p-type materials are employed as photocathodes, since the downward bending of the bands favors the transfer of photogenerated electrons towards the surface, to drive the HER.

The right-hand side of Figure 2.2 represents the energetics of the SLJ under illumination. When the electrode is illuminated, the populations of the valence and conduction bands are displaced from the equilibrium and two different Fermi levels (quasi-Fermi levels) describe separately the distribution of the photogenerated electrons and holes. The photovoltage V_{ph} arises from the splitting of the original Fermi level into the two quasi-Fermi levels. Several kinetic processes govern the electron and hole concentrations under these quasi-equilibrium conditions. On the one hand, there are fast thermalization processes of the photogenerated charge carriers within each band. On the other hand, recombination effects occur in the bulk of the semiconductor (J_{br}), in the depletion region (J_{dr}) or in defect or surface states (J_{ss}) Moreover, the charge carriers can surmount the barrier at the interface by tunneling (J_t) or through thermoionic emission (J_{et}) [19]. In general, the dominant recombination processes are the surface recombination J_{ss} and the charge transfer at the interface J_{et} [32]. However, the faster thermalization

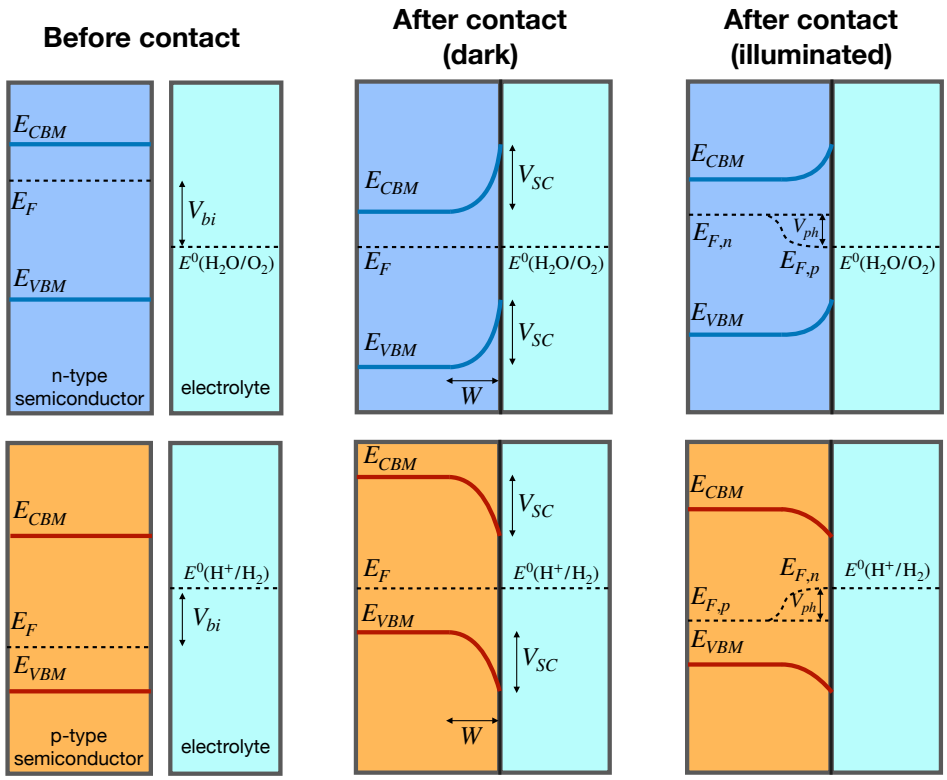

Figure 2.2

Band energetics of a semiconductor-liquid junction for a n-type (top panel) and a p-type semiconductor (bottom panel). From left to right: before contact, after contact (dark conditions) and after contact under illuminations.

effects leave the population of electrons and holes in quasi-thermal equilibrium under steady-state illumination. The quasi-Fermi level of the minority carriers is aligned with the redox potential of the solution, determining a smaller band bending. The minority-carrier concentrations at the surface are described by the energy difference between the quasi-Fermi level and the band edge.

The energetics depicted in Figure 2.2 refers to a situation in which no external bias is applied to the electrode. Given the low dielectric constant of semiconductors compared to the electrolytes commonly employed in PEC devices, the application of an external bias V to the electrode does not change the position of the band edges at the surface. However, the relative position of the Fermi level in the semiconductor w.r.t. the redox potential in the solution is modified by the bias, as shown in Figure 2.3. As a consequence, the different built-in potential determines a different band bending, hence a different concentration of charge carriers at the surface. Particularly relevant is

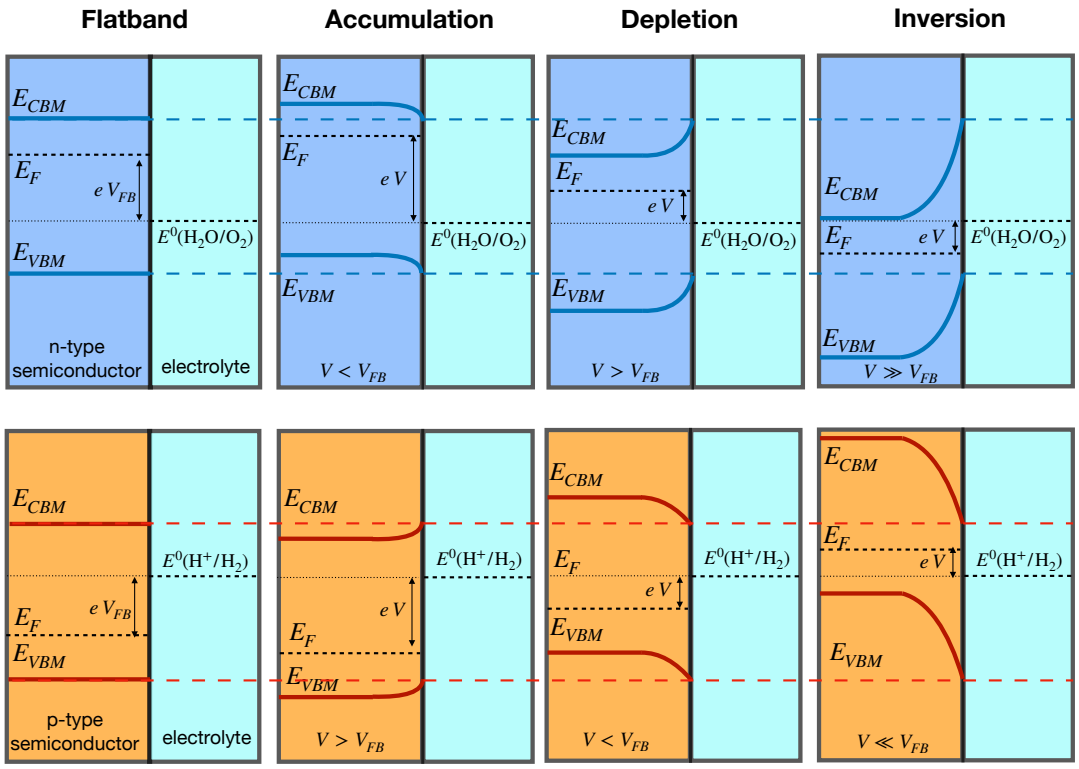

Figure 2.3

Band energetics of a semiconductor-liquid junction for a *n*-type (top panel) and a *p*-type (bottom panel) semiconductor for different applied bias. The dashed lines indicate the position of the pinned bands at the interface.

the flatband potential, V_{FB}, which corresponds to the applied bias for which no band bending occurs at the interface, hence there is no excess charge on the semiconductor side of the junction

In a *n*-type semiconductor, if a bias more negative than the flatband potential is applied, electrons are injected in the solid, producing a downward bending of the bands and an accumulation layer at the interface. Conversely, when the bias is more positive than the flatband potential, electrons are transferred from the semiconductor to the electrolyte, forming a depletion region in the semiconductor side of the interface. In this case, the Fermi level is shifted towards lower energies, increasing the band bending. In the extreme case in which the Fermi levels falls below the intrinsic Fermi level, the electrons are no more the majority carriers in an inversion region close to the surface. Following the same reasoning, in a *p*-type semiconductor the accumulation and the

depletion/inversion regions are found for bias more positive and negative than V_{FB}, respectively.

The flatband potential is particularly relevant because it allows to calculate the position of the band edges on an absolute scale. The value of V_{FB} can be determined from measurements of the capacitance of the SLJ, whose main contribution comes from the capacitance of the semiconductor C_{SC}. Indeed, the potential drop across the junction has one component in the semiconductor, V_{SC}, and one in the electrolyte, in which the main contribution comes from the Helmholtz layer, V_H. An equivalent circuit composed of two capacitors in series, with capacitance C_{SC} and C_H, is a simple model to describe the interface. The dimension of the space charge region in the semiconductor ($10-1000$ nm) is much larger than the Helmholtz layer ($0.4-0.6$ nm), with the consequence that the capacitance C_{SC} is smaller than C_H, hence giving a larger contribution to the total capacitance, in the model in which the two capacitors are connected in series. The Mott-Schottky equation relates the capacitance of the semiconductor with the applied voltage. For a n-type semiconductor the Mott-Schottky equation reads:

$$\frac{1}{(C_{SC})^2} = \frac{2}{\epsilon\epsilon_0 A^2 e N_D}\left(V - V_{FB} - \frac{k_B T}{e}\right) \quad , \tag{2.18}$$

while for a p-type:

$$\frac{1}{(C_{SC})^2} = -\frac{2}{\epsilon\epsilon_0 A^2 e N_A}\left(V - V_{FB} + \frac{k_B T}{e}\right) \quad , \tag{2.19}$$

where A is the contact area, k_B the Boltzmann constant, T the absolute temperature, e the electronic charge and N_D and N_A are the donor and acceptor densities, respectively. From the plot of $\frac{1}{(C_{SC})^2}$ as a function of V, one can derive the value of V_{FB} by extrapolating to $\frac{1}{(C_{SC})^2} = 0$. Once V_{FB} is known, the position of the band edges is easily determined from the doping densities.

2.4 Fermi level pinning

In the ideal SLJ, the band bending within the semiconductor depends on the potential of the redox couple in solution and on the external bias, while the position of the band edges E_{VBM} and E_{CBM} at the interface is independent of those quantities, but depends only on the pH of the solution with a Nernstian behaviour. Therefore, a different redox couple in solution would give rise to a different alignment with the Fermi level in the semiconductor without changing the position of the band edges.

However, if the density of the semiconductor surface states is sufficiently high, the band bending is independent of the redox species in solution, since the Fermi level becomes pinned to the energy of the surface states independently of the solution. This phenomenon is known as Fermi level pinning (FLP) and it is a limiting factor in PEC performance, since the output photovoltage is limited to a value determined by the surface states of the semiconductor [33]. FLP becomes important when the charge of the surface states becomes significantly larger than the charge of the semiconductor in the depletion region. In this case, a sort of Schottky junction between the surface states and the bulk semiconductor is formed, leading to a band bending within the semiconductor even in absence of the electrolyte [33].

Under these conditions, modelling the interface as two capacitors C_{SC} and C_H in series is not realistic anymore. A more appropriate scheme is represented by the parallel of the two capacitor relative to the semiconductor, C_{SC}, and the surface states, C_{SS}, connected in series with the capacitor C_H of the Helmholtz layer. When a potential difference across the SLJ is applied, a significant part of the potential drop occurs in the Helmholtz layer rather than in the semiconductor, leaving essentially unchanged the band bending. As a result, the photovoltage does not depend on the redox couple in solution, and any additional voltage applied to the system occurs inside the Helmholtz layer, until the surface states are completely full or empty.

2.5 Standard Hydrogen Electrode

In electrochemistry, the potential of an electrode is measured as the potential difference between the electrode itself and a reference electrode, whose potential is stable and well-defined. The reference electrode is commonly employed as half-cell in which a specific electrochemical reaction takes place. Several different reference electrodes can be chosen, each one of them based on a different redox reaction. One of the most commonly used reference electrodes is the standard hydrogen electrode (SHE), which is based on the equilibrium of following redox reaction:

$$\frac{1}{2}\mathrm{H_2} \rightleftharpoons \mathrm{H^+} + e^- \,, \tag{2.20}$$

so that at 0 V with respect to SHE equilibrium is established between a platinum electrode immersed in a 1 M $\mathrm{H^+_{aq}}$ solution (pH = 0) and gas phase $\mathrm{H_2}$ at 1 bar and 298.15 K, which is flushed around the electrode.

SHE forms the basis of the thermodynamic scale of oxidation-reduction potentials.

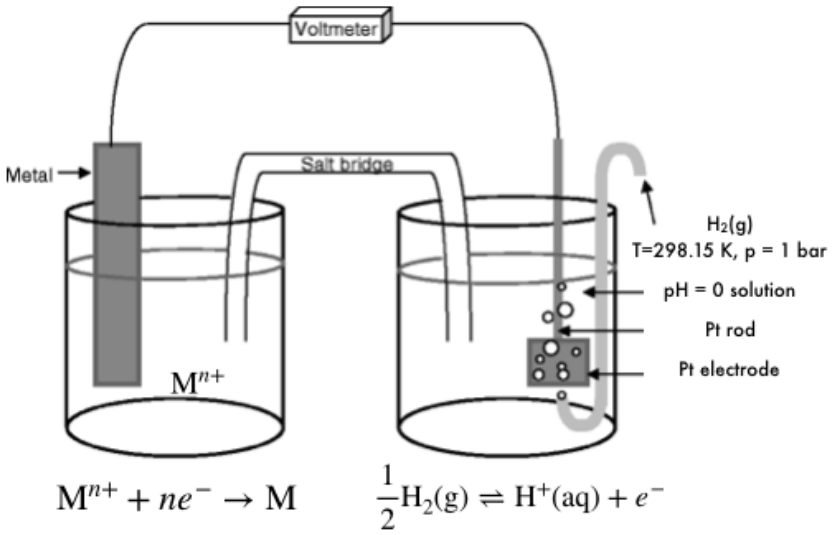

Figure 2.4

Schematic representation of the setup required to measure the potential of a metallic electrode, based on the M/M^{n+} redox reaction, with respect to SHE.

As it is schematically shown in Figure 2.4, the potential difference between the metallic electrode on the left, based on a generic M^{n+}/M redox reaction, and SHE, on the right, is measured by the voltmeter that connects the two electrodes. Since the SHE potential is set to zero by definition, this value V indicated on the voltmeter represents the potential of the electrode, hence of the underlying reaction, measured w.r.t. SHE. The potential difference V is connected with the Gibbs free energy change of the reaction, ΔG as:

$$\Delta G = -nFV\,, \tag{2.21}$$

where n is the number of electrons involved in the reaction and F is the Faraday constant. This relation holds for electrochemical reactions in generic conditions. However, in textbooks it is common to report the standard potential V^0, which refers to standard conditions of temperature (298.15 K), pressure (1 bar) and activity of the products and the reactants (1). The Nernst equation relates the potential V with the potential at standard conditions:

$$V = V^0 - \frac{RT}{nF} \ln \frac{a_{ox}}{a_{red}}\,, \tag{2.22}$$

where R is the gas constant, T the temperature and a_{ox}/a_{red} the activities of the oxidized/reduced species in solution. When an external bias ΔV is applied to the working

electrode, the corresponding potential difference measured w.r.t. SHE indicated on the voltmeter is shifted by the same quantity ΔV.

2.5.1 Absolute potential of SHE

As explained in the previous paragraph, SHE represents the reference state for measuring the potential of redox reactions in the electrochemists community. However, in semiconductor solid-state physics, the electron energy in vacuum is taken as a reference, and the position of the valence and conduction band are measured with respect to this value. One of the main requirements for a material to be employed as a photoelectrode, is that the VBM (CBM) must be in a suitable position to drive the OER (HER). It is not obvious how to compare an energy level, measured with respect to the vacuum level, with a redox potential, defined with respect to SHE.

The concept of absolute electrode potential allows to compare two quantities which apparently belong to two different worlds. In analogy with the well-known concept of work function in physics, the absolute potential of an electrode is defined as the difference in electronic energy between a point inside the electrode (Fermi level) and a point in vacuum just outside the electrolyte in which the electrode is immersed [34]. Since SHE is the reference state for electrochemists, once its absolute potential is determined, so it is the absolute potential of any other electrode.

The value of the absolute potential of SHE at ambient conditions has been determined by Trasatti to be (4.44 ± 0.02) V [34], which means, in the physicists language, that the SHE level lies (4.44 ± 0.02) eV below the vacuum level. According to the definition given above, the absolute potential of an electrode M immersed in a solution S could be expressed as the sum of physically measurable quantities:

$$V_M^{abs} = \phi_M + \Delta_S^M \psi \,, \tag{2.23}$$

where ϕ_M is the work function of the metal and $\Delta_S^M \psi$ is the electrostatic potential difference between the metal and the solution in thermodynamic equilibrium, also known as Volta potential. For practical purposes, it is more convenient to determine first the absolute potential at zero charge ($\sigma = 0$) of an ideally polarizable Hg electrode:

$$V_{\mathrm{Hg},\sigma=0}^{abs} = \phi_{\mathrm{Hg}} + \Delta_S^{\mathrm{Hg}} \psi_{\sigma=0} \,, \tag{2.24}$$

and then the absolute potential of SHE, subtracting the standard potential of the Hg electrode, $V_{\mathrm{Hg},\sigma=0}^{SHE}$, measured with respect to SHE:

$$\begin{aligned} V_{SHE}^{abs} &= V_{\mathrm{Hg},\sigma=0}^{abs} - V_{\mathrm{Hg},\sigma=0}^{SHE} \\ &= \phi^{\mathrm{Hg}} + \Delta_S^{\mathrm{Hg}} \psi_{\sigma=0} - V_{\mathrm{Hg},\sigma=0}^{SHE} \quad . \end{aligned} \tag{2.25}$$

The sum of the experimental values of the quantities contained in this last expression provides the well-known value of (4.44 ± 0.02) V as the absolute potential of SHE [34].

2.5.2 Reversible Hydrogen Electrode

Despite its simple definition and its versatility, SHE is an ideal electrode but not of practical use in a laboratory, where the use of the reversible hydrogen electrode (RHE) is preferred. The definition of RHE is similar to that of SHE, except from the fact that the electrode is directly immersed in the electrolytic solution and not separated by a salt bridge. Therefore, the concentration of protons is not 1 M, but it is determined by the pH of the solution and the measured potential changes with the pH with a Nernstian behaviour:

$$V_{\mathrm{RHE}} = V_{\mathrm{SHE}} + (0.059\ \mathrm{V}) \times \mathrm{pH}\,, \tag{2.26}$$

where the slope, 0.059 V, corresponds to $\frac{RT}{F}$ at ambient temperature.

3

Semiconducting photoelectrodes

CONTENTS

Semiconducting materials are the basis of every system for the artificial photosynthesis, due to their ability to absorb light and create electron-hole pairs. Transition metal (TM) oxides are an attractive class of materials for PEC applications, since they satisfy many of the criteria for an efficient hydrogen production. In particular, their abundance on earth, non-toxicity and low-cost fabrication make them good candidates in the field of the water splitting. However, the current technology is still far from the production of an efficient device, since their PEC performance is limited by different factors.

This chapter opens with a brief description of some parameters used to assess the PEC performance of the materials. Then, we will briefly describe the most promising materials for PEC applications, highlighting their strength and weaknesses.

3.1 Evaluation of PEC performance

The evaluation of the PEC performance of a material as a photoelectrode does not require the construction of a complete cell, and is typically assessed in laboratories by evaluating one or more of the following parameters [27]:

- *Applied-bias photon-to-current efficiency* (ABPCE). The photocurrent density J_{ph} flowing from an illuminated photoelectrode in a solution towards the counter electrode is measured as a function of the applied potential V, defined relative to a reference electrode. The ABPCE for the OER taking place at the photoanode is

computed as:

$$\text{ABPCE} = \frac{J_{ph} \times (V^{\text{OER}} - V)}{P_{in}}\,, \tag{3.1}$$

where V^{OER} is the standard potential of the OER reaction, 1.23 V relative to the reversible hydrogen electrode potential V_{RHE}, and P_{in} is the illumination power density.

- *Incident photon-to-current efficiency (IPCE).* In order to determine the contribution of each wavelength to the solar spectrum, the photocurrent $J_{ph\,,\lambda}$ density is measured at a fixed applied potential V as a function of the wavelength λ and the IPCE is computed as:

$$\text{IPCE} = J_{ph,\lambda} \times \frac{\frac{hc}{e}}{P_\lambda \times \lambda}\,. \tag{3.2}$$

- *Absorbed photon-to-current efficiency (APCE).* This value can be simply obtained by dividing the IPCE by the fraction of photons absorbed at each wavelength.

- *Solar-to-hydrogen efficiency (STHE).* The time-integrated operating photocurrent density J_{op} provides the total charge flowed in the system during the operation time. The total charge compared with the amount of gas evolved gives rise to the faradaic efficiency η_F. The STH of the overall water splitting reaction is calculated as:

$$\text{STH} = J_{op} \times (1.23\ V) \times \frac{\eta_F}{P_{in}}\,. \tag{3.3}$$

The experimental setups for measuring the PEC efficiency are shown in Figure 3.1, which is taken from Ref.[27].

3.2 Photoanode materials

Oxygen evolving materials are n-type semiconductors, whose band bending at the interface allows the drifting of photogenerated holes from the valence band towards the surface. Therefore, controlling the valence band level in these compounds is extremely important.

TM oxides in which the cation has the d^0 electronic band, such as TiO_2 or WO_3, have in general large bandgap, given their high ionic character, and a VBM with a main O $2p$ character. The prototypical materials for PEC water splitting is TiO_2 [16], whose catalytic properties have attracted enormous attention for decades [35]. The

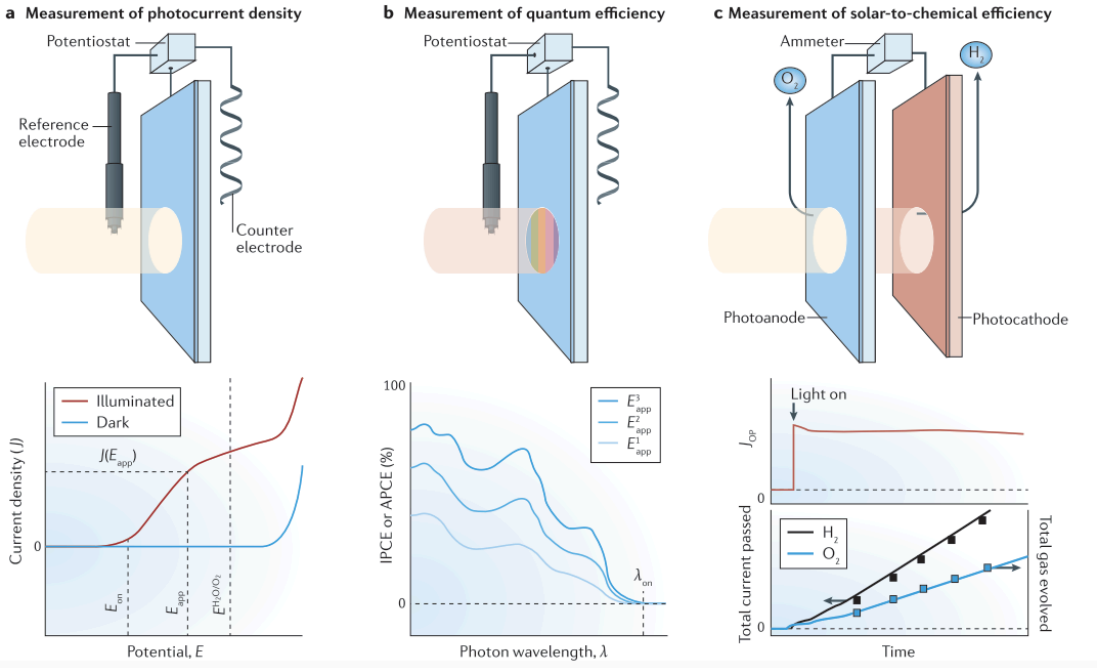

Figure 3.1

Photocurrent density and conversion efficiency as device performance metrics. Figure taken from Ref.[27]

position of the band edges of TiO_2 is suitable for the water splitting reaction in a single-absorber PEC cell. However, the large bandgap of TiO_2, $3.0 - 3.2$ eV, does not allow an efficient absorption of the solar spectrum. In order to increase the light adsorption, mid-gap states can be introduced by doping [36] or defects. However, the slow transport of photogenerated carriers between the spatially isolated impurities leads to a high recombination rate, limiting the PEC performace [27]. The tungsten oxide WO_3 suffers from similar limitations and much effort has been made to tune the electronic structure in order to enhance the PEC performance [37].

TM oxides based on cation with the d^n configuration usually have smaller bandgaps and a good stability in water. Among them, binary Fe_2O_3 [38], Co_3O_4 [39] and ternary $BiVO_4$ [40] have emerged as promising candidates for the anodic reaction, yet showing a low polaron conductivity that affects the transport and the charge separation.

3.3 Photocathode materials

The development of stable and efficient semiconducting photocathodes is an open challenge in the scientific community [27]. Different classes of materials has been investigated in the recent years, including ferrites hybridized with high-energy Ca $3d$ states [41], metal chalcogenides [42–44], transition-metal dichalcogenides [45] and copper(I)-based oxides [6, 46–51].

This last class of materials has received significant attention because the binary cuprous oxide, Cu_2O, a p-type semiconductor with a direct band gap of 2.17 eV [52], possesses an energetic alignment of its conduction band edge suitable for the HER [46]. However, Cu_2O is unstable in aqueous environments under illumination since the redox potentials of the material lie within the redox potentials of water and, therefore, a photoexcited electron tends to reduce Cu_2O into Cu rather than reducing protons. Consequently, without the application of a surface protective layer, Cu_2O degrades and the performance is lost, making its application as a photocathode more difficult and expensive and therefore less practical [53].

Building on the work already carried out on Cu_2O, other copper-based oxides emerged as candidates for the photocathode [51], in particular, ternary oxides that crystallize in the delafossite structure, like $CuFeO_2$ [6] or $CuRhO_2$ [50].

3.3.1 $CuFeO_2$ as a promising photocathode material

The delafossite $CuFeO_2$ (CFO), previously investigated for its low-temperature multiferroic effects [54–57], has recently emerged as a promising photocathode material [6–8, 10, 11, 58]. This compound is particularly attractive because it is an intrinsic p-type semiconductor with an optical gap of roughly 1.5 eV and CBM suitably aligned to promote the HER under illumination [11]. Moreover, it benefits from high stability in water, alleviating the need for a surface-protective layer. CFO is based on earth abundant elements and different techniques for its growth and synthesis have been reported, including solid state reactions [59], electrodeposition [6], pulsed laser deposition (PLD) [60] and sol-gel [7]. Thin films synthesized with a scalable, solution-based sol-gel methods on top of fluorine-doped tin oxide (FTO) substrate have shown good light absorption properties and favorable band-edges positions [7, 8].

In particular, the band edges positions were determined from the Mott-Schottky plot, in which the space-charge layer capacitance, cf. Eq.(2.19), is plotted as a function

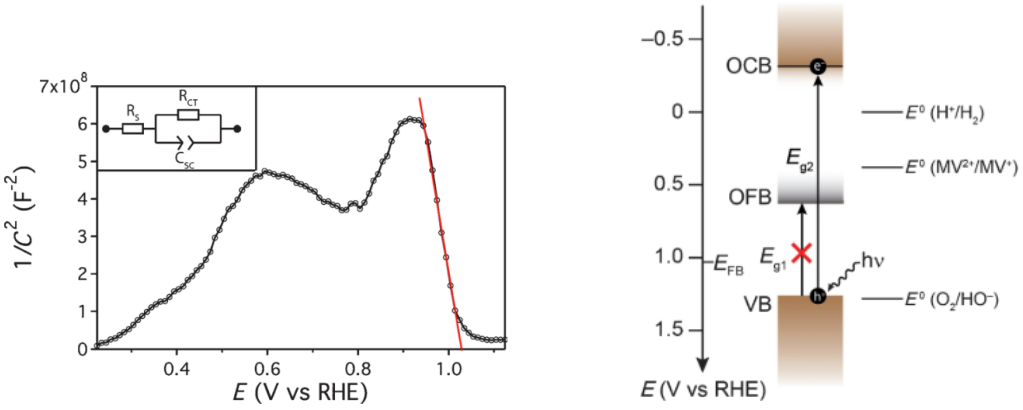

(a) (b)

Figure 3.2

(a) Mott–Schottky diagram of a $CuFeO_2$ film on FTO. The red line indicates the linear region that corresponds to the depletion regime of the p-type material:it intercepts the x axis at the flat-band potential. (b) Band energy diagram under flatband conditions. Figures reproduced from Ref.[7].

of the potential. From a typical Mott-Schottky plot it is possible to reconstruct the band energetics of a SLJ, as it was previously introduced in Figure 2.3. The Mott-Schottky plot and the band energy diagram proposed by Prévot et al. [7] are reported in Figure 3.2.

In the accumulation region, $1/C_{SC}$ is almost constant and close to zero, since the photogenerated electrons could not reach the surface because of the unfavorable band-bending. In the depletion region, $1/C_{SC}$ increases linearly with the voltage, since the band bending is now favorable for driving the electrons towards the surface. From a linear interpolation of $1/C_{SC}$ in the depletion region a flatband potential of +1.01 V was obtained. Finally, the inversion region with an opposite slope is expected. However, the oscillating behavior observed in the Mott-Schottky plot was attributed to the existence of an optically forbidden bandgap, smaller than the optical bandgap [7]. According to the band energy diagram under flatband conditions, reported in Figure 3.2(b), the CBM lies −0.3 V versus RHE, a favorable potential to drive the HER.

Nevertheless, the photocurrent measured in the bare CFO electrode was rather low and a surface functionalization with an electron scavenging molecule (O_2) yields to a marked increase in the photocurrent by a factor of 10 [6] or 42 [7]. However, even in presence of the electron scavenging molecule, the photocurrent is significantly lower then

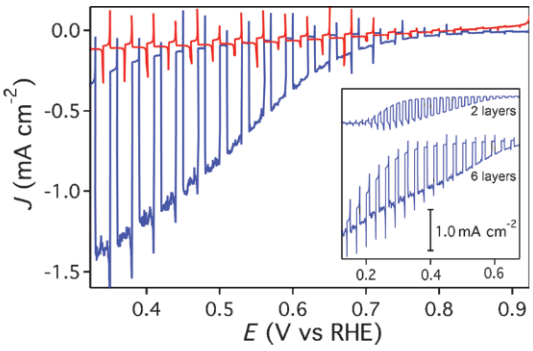

(a)

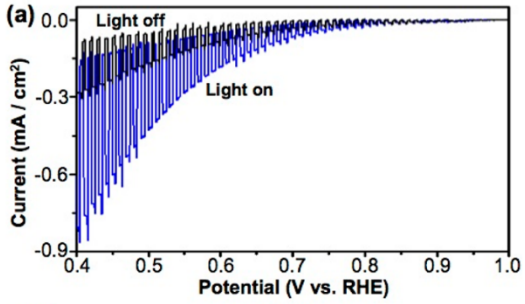

(b)

Figure 3.3

Linear sweep voltammogram of $CuFeO_2$ electrodes under intermittent illumination, taken from Ref.[7] (a) and Ref.[6](b).

the theoretical maximum value. Indeed, from the absorption spectrum of CFO and the number of photons created by a Xenon arc lamp at each wavelength, a theoretical maximum photocurrent of 14.8 mA/cm^{-2} is derived [7]. The steady-state current measured in a linear sweep voltammetry at +0.4 V versus RHE was only 1.05 mA/cm^{-2} [7] or even lower [6, 10]. Larger photocurrents, 2.4 mA/cm^{-2}, were measured in a $CuFeO_2$ decorated with a NiFe-layered double hydroxide/reduced graphene oxide electrocatalyst [9] and in a host-guest composite electrode supported by $CuAlO_2$ [8]. To date, these measurements represent the highest photocurrent obtained by CFO photoelectrodes, but still far from a good efficiency.

Understanding and ameliorating this low photocurrent density has become the main focus of research into CFO photocathodes. In general, the poor photoelectrode performance is linked to the presence of either surface or bulk defect states. While the former

issue can be circumvented by postprocessing treatments, intrinsic bulk trapping states could permanently inhibit the application of the material as a photoelectrode.

A high density of surface states (10^{14} cm^{-2}) inducing Fermi level pinning at the SLJ was found by interfacing a CFO photoelectrode with different redox systems [11]. The origin of these states, located around 0.6 eV above the valence band, was attributed to the presence of metal hydroxyl groups on the surface [11]. In a recent contribution, the Fermi level pinning at the same potential has been observed and attributed to the formation of bulk Fe^{3+}/Fe^{2+} polaronic levels [12].

A very long lifetime for photogenerated charge carriers ($\sim$ 200 ns) was found by time-resolved microwave conductivity measurements [11], excluding bulk properties as limiting factors. However, a recent investigation of the CFO performance bottlenecks highlighted short photogenerated electron diffusion lengths and polaron-mediated recombination as additional potential obstacles to be overcome [10], in contrast with the previous report. The low APCE, $3 - 10\%$ for wavelengths from 750 to 400 nm, indicates that only a small part of the photogenerated charge carriers is collected at the semiconductor-liquid junction, since most of them undergo bulk recombination [10].

In summary, there is still much debate in the literature about the origin of the low PEC performance of CFO. Theoretical investigations can help gaining the atomistic insight required to understand these features. However, an adequate theoretical characterization is currently not available to complement experimental results. The aim of this thesis is to help filling this gap, providing insight into the processes at the CFO-water interface.

4

Computational Methods

CONTENTS

First-principles calculations based on Density Functional Theory (DFT) are a well suited tool for screening materials and interfaces since DFT provides a favourable tradeoff between accuracy and computational cost. Beyond a static approximation, DFT can be combined with molecular dynamics (MD) giving rise to *ab-initio* molecular dynamics (AIMD), to be used to equilibrate and sample geometries for the heterogeneous interfaces. The atomistic insights obtained at the DFT level can be used to calculate thermodynamic potentials that determine the macroscopic properties of materials. Moreover, in recent years, DFT has also found applications in the field of the (photo)electrochemistry, as a tool both for simulating electrochemical reactions and for calculating level alignment. However, overcoming the well-known accuracy limitations of DFT is important for a correct interpretation of the results.

In this chapter we summarize the basic concepts of the computational methods used in this work, starting from DFT and showing how it can be employed in other fields.

4.1 Density Functional Theory

Density Functional Theory [61, 62] is a quantum mechanical theory with a large predictive power of the ground-states properties of atoms, molecules and extended systems. Although it was founded in the 60s, it is only from the 80s that DFT has become very popular, so much so that it was the most active field in physics during the period from 1980 to 2010 [63] and in 1998 its founder Walter Kohn was awarded with the Nobel prize. Although exact in principle, DFT would not be of practical use, unless some approximations to be used in practical calculations are provided.

4.1.1 Born-Oppenheimer approximation

First of all, the many body problem of a system of N_e electrons and N_n nuclei in mutual interaction cannot be solved exactly because the interactions couple the degrees of freedom of the particles. However, since nuclei are about 10^3 times heavier than the electrons, they move in different timescales and exhibit vastly different dynamics. The nuclear motion is slow enough not to induce transition to different electronic configurations, so that the nuclei can be considered at rest while studying the electronic problem. The nuclear and the electronic motion can be decoupled factorizing the total wavefunction as the product of two functions, a ionic wavefunction $\Phi(\mathbf{R})$, which depends on the nuclear coordinates $\mathbf{R} = \{\mathbf{R}_I\}$, and an electronic wavefunction $\psi_{\mathbf{R}}(\mathbf{r})$, which depends explicitly on the electronic coordinates $\mathbf{r} = \{\mathbf{r}_i\}$ and parametrically on $\mathbf{R}$:

$$\Psi(\mathbf{r}, \mathbf{R}) = \psi_{\mathbf{R}}(\mathbf{r})\Phi(\mathbf{R}) \quad . \tag{4.1}$$

This assumption proposed by Born and Oppenheimer [64] is known as adiabatic approximation. The ionic wavefunction $\Phi(\mathbf{R})$ is solution of the Schrödinger equation:

$$\left(-\sum_I \frac{\hbar^2}{2M_I} \frac{\partial^2}{\partial \mathbf{R}_I^2} + E(\mathbf{R}) \right) \Phi(\mathbf{R}) = \varepsilon \Phi(\mathbf{R}) \quad , \tag{4.2}$$

where M_I is the mass of the I-th nucleus and $E(\mathbf{R})$ is the ground-state energy of the electronic problem for the configuration $\mathbf{R}$:

$$\left(-\sum_i \frac{\hbar^2}{2m} \frac{\partial^2}{\partial \mathbf{r}_i^2} + \frac{e^2}{2} \sum_{i \neq j} \frac{1}{|\mathbf{r}_i - \mathbf{r}_j|} - \sum_{i,I} \frac{Z_I e^2}{|\mathbf{r}_i - \mathbf{R}_J|} + \frac{e^2}{2} \sum_{I \neq J} \frac{Z_I Z_J}{|\mathbf{R}_I - \mathbf{R}_J|} \right) \psi_{\mathbf{R}}(\mathbf{r}) = \\ = E(\mathbf{R}) \psi_{\mathbf{R}}(\mathbf{r}) \,. \tag{4.3}$$

Here, m and $-e$ are the electronic mass and charge, and $e\,Z_I$ is the charge of the I-th nucleus. Solving Eq.(4.3) is still challenging because the electrons interact among them-

selves, thus the electronic wavefunction $\psi_{\mathbf{R}}(\mathbf{r})$ cannot be simply factorized in a product of single-particle wavefunctions. In the DFT scheme, the ground-state energy of a many-particle system depends only on the electronic density $n(\mathbf{r})$ which is obtained solving one-electron Schrödinger equations with a local, mean-field-like effective potential.

4.1.2 Hohenberg-Kohn Theorems

The description of the ground-state properties in terms of the ground-state electron density is based on the Hohenberg-Kohn theorems [61]. The first Hohenberg-Kohn theorem states that there is a one-to-one correspondence between the ground-state electron density distribution of a N_e electron system and the external potential such that the external potential, hence the Hamiltonian, is uniquely determined by the electron density. This statement leads to the second Hohenberg-Kohn theorem in which a variational principle for the total energy functional

$$E[n(\mathbf{r})] = F[n(\mathbf{r})] + \int n(\mathbf{r})\, V_{ext}(\mathbf{r}) d\mathbf{r} \tag{4.4}$$

is formulated, defining a universal functional of the ground-state density $F[n(\mathbf{r})]$, which does not depend on the external potential and contains only the kinetic energy and the mutual interaction of the electrons:

$$F[n(\mathbf{r})] = T[n(\mathbf{r})] + V_{ee}[n(\mathbf{r})]\,. \tag{4.5}$$

The minimization of the total energy functional $E[n(\mathbf{r})]$ with respect to the electron density, with the constraint that the number of electrons is preserved $\int n(\mathbf{r}) d\mathbf{r} = N_e$, provides the ground-state charge density $n_0(\mathbf{r})$ and the ground-state energy E_0 [61]:

$$\min_{n(\mathbf{r})} E[n(\mathbf{r})] = F[n_0(\mathbf{r})] + \int n_0(\mathbf{r})\, V_{ext}(\mathbf{r}) d\mathbf{r} = E_0\,. \tag{4.6}$$

However, the universal functional $F[n(\mathbf{r})]$ of a system of interacting electrons is not known. In the paper which is considered the second milestone of the DFT [62], Kohn and Sham showed how the problem of interacting electrons can be mapped into an auxiliary noninteracting system.

4.1.3 Kohn-Sham Equations

The Hohenberg-Kohn theorems apply to any electron system, both interacting or not. For a system of non-interacting electrons, the first Hohenberg-Kohn theorem guarantees the existence and uniqueness of an external potential $\widetilde{V}_{ext}$ producing a ground-state density $\widetilde{n}_0(\mathbf{r})$ equal to $n_0(\mathbf{r})$. The universal functional $F[n(\mathbf{r})]$ of the non-interacting

system is simply equal to the kinetic energy term $T_0[n(\mathbf{r})]$, while for the interacting system it can be decomposed as:

$$F[n(\mathbf{r})] = T_0[n(\mathbf{r})] + \frac{e^2}{2}\int \frac{n(\mathbf{r})n(\mathbf{r}')}{|\mathbf{r}-\mathbf{r}'|}\, d\mathbf{r}d\mathbf{r}' + E_{xc}[n(\mathbf{r})]\,, \tag{4.7}$$

where the second term in the right-hand side represents the Hartree energy $E_H[n(\mathbf{r})]$, the classical electrostatic interaction due to the charge density distribution, which was separated out from the $V_{ee}[n(\mathbf{r})]$ term. Analogously, the kinetic energy of the noninteracting system was separated out from the kinetic term $T[n(\mathbf{r})]$ and all the remaining parts are included into the exchange-correlation energy $E_{xc}[n(\mathbf{r})]$:

$$E_{xc}[n(\mathbf{r})] = T[n(\mathbf{r})] - T_0[n(\mathbf{r})] + V_{ee}[n(\mathbf{r})] - E_H[n(\mathbf{r})]\,. \tag{4.8}$$

The exchange-correlation functional represents the difference between what can be calculated and what cannot, and for this reason it was named the *stupidity term* by Feynman [65].

The variational principle applied to the total energy functional of the interacting system (4.4) yields:

$$\frac{\delta E[n(\mathbf{r})]}{\delta n(\mathbf{r})} = \frac{\delta T_0[n(\mathbf{r})]}{\delta n(\mathbf{r})} + V_H(\mathbf{r}) + V_{xc}(\mathbf{r}) + V_{ext}(\mathbf{r}) = \mu\,, \tag{4.9}$$

where μ is a Lagrange multiplier associated with the constrained total number of particles, while the Hartree $V_H(\mathbf{r})$ and the exchange-correlation potential $V_{xc}(\mathbf{r})$ are the functional derivatives of the Hartree and the exchange-correlation energy functionals with respect to the electron density:

$$V_H = \frac{\delta E_H[n(\mathbf{r})]}{\delta n(\mathbf{r})} = e^2\int \frac{n(\mathbf{r})}{|\mathbf{r}-\mathbf{r}'|}\, d\mathbf{r} \qquad V_{xc} = \frac{\delta E_{xc}[n(\mathbf{r})]}{\delta n(\mathbf{r})}\,. \tag{4.10}$$

The corresponding equation for the system of noninteracting electrons with the same electronic density in an external potential $\widetilde{V}_{ext}(\mathbf{r})$ reads:

$$\frac{\delta E[n(\mathbf{r})]}{\delta n(\mathbf{r})} = \frac{\delta T_0[n(\mathbf{r})]}{\delta n(\mathbf{r})} + \widetilde{V}_{ext}(\mathbf{r}) = \mu\,. \tag{4.11}$$

The two problems represented by Eq.(4.9) and Eq.(4.11) are formally equivalent, provided that

$$\widetilde{V}_{ext}(\mathbf{r}) = V_H(\mathbf{r}) + V_{xc}(\mathbf{r}) + V_{ext}(\mathbf{r})\,. \tag{4.12}$$

The external potential $\widetilde{V}_{ext}(\mathbf{r})$ which satisfies the above equation is known in the DFT community as the Kohn-Sham potential V_{KS}.

The ground-state wavefunction of a N_e noninteracting electrons system is just the

Slater determinant of N_e single-particle orbitals $\{\psi_i\}$, which are the N_e low-lying eigenfunctions of the well-known Kohn-Sham equations:

$$\left[-\frac{\hbar^2}{2m}\frac{\partial^2}{\partial \mathbf{r}^2} + V_{KS}(\mathbf{r})\right]\psi_i(\mathbf{r}) = \epsilon_i\psi_i(\mathbf{r})\,, \tag{4.13}$$

The ground-state density can be written as the sum of independent orbital contributions:

$$n_0(\mathbf{r}) = \sum_{i=1} f_i|\psi_i(\mathbf{r})|^2\,. \tag{4.14}$$

where f_i is the occupation number of the orbital ψ_i. The ground-state energy can be obtained by inserting $n_0(\mathbf{r})$ into the total energy functional, and for the noninteracting system it is equal to the sum of the N_e lowest eigenvalues:

$$\sum_i f_i\epsilon_i = T_0[n_0(\mathbf{r})] + \int n_0(\mathbf{r})\,V_H(\mathbf{r})\,d\mathbf{r} + \int n_0(\mathbf{r})\,V_{xc}(\mathbf{r})\,d\mathbf{r} + \int n_0(\mathbf{r})\,V_{ext}(\mathbf{r})\,d\mathbf{r}\,, \tag{4.15}$$

where the kinetic term is easily calculated as:

$$T_0[n_0(\mathbf{r})] = -\frac{\hbar^2}{2m}\sum_i f_i \int \psi_i^*(\mathbf{r})\frac{\partial^2\psi_i(\mathbf{r})}{\partial \mathbf{r}^2}d\mathbf{r}\,. \tag{4.16}$$

Analogously, the ground-state energy of the interacting system is:

$$E_0 = E[n_0(\mathbf{r})] = T_0[n_0(\mathbf{r})] + E_H[n_0(\mathbf{r})] + E_{xc}[n_0(\mathbf{r})] + \int n_0(\mathbf{r})\,V_{ext}(\mathbf{r})d\mathbf{r}\,, \tag{4.17}$$

Comparing Eq.(4.17) with Eq.(4.16) the total energy of the interacting system can be expressed in terms of the eigenvalues of the noninteracting problem:

$$E_0 = \sum_i f_i\epsilon_i - \frac{1}{2}E_H[n_0(\mathbf{r})] + E_{xc}[n_0(\mathbf{r})] - \int n_0(\mathbf{r})\,V_{xc}(\mathbf{r})d\mathbf{r}\,. \tag{4.18}$$

So far, the DFT is an exact model. The complicated system of interacting electrons is mapped into a system of non-interacting electrons, described by Schröedinger-like equations (4.13) with a local, effective potential V_{KS} which, however, depends on its own solution through the density (4.14). The solution of these non-linear equations can be done self-consistently, starting from an initial guess of the wavefunctions and the potential and evolving the equations up to the self-consistency. However, the exchange-correlation term $E_{xc}[n(\mathbf{r})]$ which enters the Kohn-Sham potential through its functional derivative is unknown and suitable approximations must be provided to use DFT as a practical tool.

4.1.4 Exchange-correlation functionals

The simplest approximation of $E_{xc}^{LDA}[n(\mathbf{r})]$ is given by the local density approximation (LDA) [62], in which each small volume of the system behaves as a homogeneous electron gas with the density equal to the local density of the inhomogeneous system:

$$E_{xc}^{LDA}[n(\mathbf{r})] = \int \epsilon_{xc}^{hom}(n(\mathbf{r}))\, n(\mathbf{r})\, d\mathbf{r}\,, \tag{4.19}$$

where $\epsilon_{xc}^{hom}(n(\mathbf{r}))$ is the exchange-correlation energy per electron of an homogeneous electron gas whose density is $n(\mathbf{r})$. The exchange-correlation potential is obtained as a functional derivative of Eq.(4.19):

$$V_{xc}^{LDA}(\mathbf{r}) = \frac{\delta E_{xc}^{LDA}[n(\mathbf{r})]}{\delta n(\mathbf{r})} = \epsilon_{xc}^{hom}(n(\mathbf{r})) + n(\mathbf{r})\, \frac{\partial \epsilon_{xc}^{hom}(n(\mathbf{r}))}{\partial n(\mathbf{r})}\,. \tag{4.20}$$

LDA is particularly efficient in systems with a reasonably slowly varying spatial density, yet the binding energies are typically overestimated and the bond lengths underestimated.

To overcome these limitations, corrections to the LDA functional can be applied in terms of the density gradient, in the so called generalized gradient approximation (GGA) [66]:

$$E_{xc}^{GGA}[n(\mathbf{r})] = \int \epsilon_{xc}^{GGA}(n(\mathbf{r}), \nabla n(\mathbf{r}))\, n(\mathbf{r})\, d\mathbf{r}\,. \tag{4.21}$$

Compared to LDA, GGA provides soften bonds in terms of binding energy and bond length, correcting or over-correcting the LDA values [67]. Moreover, it improves the description of inhomogeneous systems, like transition metals, where LDA completely fails.

Several forms of GGA functional have been proposed [67–70]. Among them, the most widely used is the formulation of Perdew et al. (PBE), whose reference paper [67] was the most cited article in physics in the period between 1996 and 2010.

4.1.5 Numerical implementation of the Kohn-Sham equations

In order to use DFT for practical purposes, the complicated integro-differential Kohn-Sham equations must be transformed into an algebraic form to be solved numerically. In periodically repeated crystalline solids, in which the Bloch theorem holds, the electronic wavefunction, hence all the operators in the Hamiltonian, can be expanded in a plane wave basis set. According to the Bloch theorem, the single-particle electronic wavefunctions in a periodic potential, $V(\mathbf{r}+\mathbf{R}) = V(\mathbf{r})$, can be written in the momentum space as a plane wave modulated by a periodic function $u_{n\mathbf{k}}(\mathbf{r})$, having the same periodicity

of the lattice, $u_{n\mathbf{k}}(\mathbf{r}+\mathbf{R}) = u_{n\mathbf{k}}(\mathbf{r})$:

$$\psi_{n,\mathbf{k}}(\mathbf{r}) = e^{i\mathbf{k}\cdot\mathbf{r}} u_{n,\mathbf{k}}(\mathbf{r})\,, \tag{4.22}$$

where n is the band index and $\mathbf{k}$ is the crystal momentum of the electron, which is defined within the first Brillouin zone (BZ) of the reciprocal space. The periodic part is expanded in a plane wave basis set,

$$u_{n,\mathbf{k}}(\mathbf{r}) = \frac{1}{\sqrt{\Omega}} \sum_{\mathbf{G}} c_{n,\mathbf{k}+\mathbf{G}} e^{i\mathbf{G}\cdot\mathbf{r}}\,, \tag{4.23}$$

where Ω is the volume of the cell, $\mathbf{G}$ is a reciprocal lattice vector and $c_{n,\mathbf{k}+\mathbf{G}}$ are the coefficients of the plane waves. Consequently, the Kohn-Sham orbitals (4.22) can be expressed in terms of the plane wave basis set as:

$$\psi_{n,\mathbf{k}}(\mathbf{r}) = \frac{1}{\sqrt{\Omega}} \sum_{\mathbf{G}} c_{n,\mathbf{k}+\mathbf{G}} e^{i(\mathbf{k}+\mathbf{G})\cdot\mathbf{r}}\,. \tag{4.24}$$

This expansion is exact in the limit of an infinite plane wave basis set. In practical calculations, the summation is truncated to include only the $\mathbf{G}$-vectors that have a kinetic energy lower than a cutoff energy E_{cut}:

$$\frac{\hbar^2}{2m}|\mathbf{k}+\mathbf{G}|^2 \leq E_{cut}\,. \tag{4.25}$$

The accuracy of this approximation must be verified by convergence tests of the quantities of interest as a function of E_{cut}. The ground-state density (4.14) can be also expanded in plane waves:

$$n_0(\mathbf{r}) = \sum_{\mathbf{G}} n_0(\mathbf{G}) e^{i\mathbf{G}\cdot\mathbf{r}}\,, \tag{4.26}$$

where $n_0(\mathbf{G})$ is the charge density in the reciprocal space:

$$n_0(\mathbf{G}) = \frac{1}{\Omega} \sum_{n} \int_{BZ} f_{n,\mathbf{k}} \sum_{\mathbf{G}'} c^{\star}_{n,\mathbf{k}+(\mathbf{G}'-\mathbf{G})} c_{n,\mathbf{k}+\mathbf{G}'} d\mathbf{k}. \tag{4.27}$$

The modulus of the largest $\mathbf{G}$-vector appearing in Eq.(4.26) is twice as large as the maximum $\mathbf{G}$-vector determined by the cutoff energy in Eq.(4.25), because it depends on the vector difference between $\mathbf{k}+\mathbf{G}$ and $\mathbf{k}+\mathbf{G}'$. As a consequence, the kinetic energy cutoff of the charge density is 4 times larger than the kinetic energy cutoff of the wavefunction. Moreover, the integral over the BZ appearing in Eq.(4.27), is replaced, in numerical calculations, with a summation over a discrete grid of $\mathbf{k}$-points. One of the most used techniques to sample the BZ is the Monkhorst-Pack grid [71], an homogeneous grid with rows and columns of $\mathbf{k}$-points running parallel to the reciprocal lattice vectors.

Using the plane wave expression of the Kohn-Sham orbitals, (4.24), the Kohn-Sham equations in the reciprocal space become equations for the coefficients $c_{n,\mathbf{k}+\mathbf{G}}$:

$$\sum_{\mathbf{G}'} \left[-\frac{\hbar^2}{2m} |\mathbf{k}+\mathbf{G}|^2 + V_{KS}(\mathbf{G},\mathbf{G}') \right] c_{n,\mathbf{k}+\mathbf{G}'} = \epsilon_{n,\mathbf{k}+\mathbf{G}}\, c_{n,\mathbf{k}+\mathbf{G}}\,. \tag{4.28}$$

The equations are solved iteratively, and the coefficients are used to compute the charge density, from which a new Kohn-Sham potential is constructed and the equations are solved again until the self-consistency is reached.

However, a problematic component of the Kohn-Sham potential in the plane wave representation is the nuclear potential $V_{ext}(\mathbf{G}+\mathbf{G}')$. Indeed, the Coulomb electron-ion interaction decays too slowly to be represented by a small number of plane waves. A large kinetic energy cutoff is also required to describe the rapid oscillations of the wavefunction of the core electrons. However, the localized core electrons do not contribute to the chemical reactivity of the system, which is led by the valence electrons. This assumption is the basis of the pseudopotential technique [72].

The basic idea of the pseudopotential approximation is to freeze the core electrons and replace the potential of the resulting ionic core (nuclei plus core electrons) with a fictitious potential, smoother in the core region, such that the behaviour of the valence electrons is not affected outside a certain cutoff radius r_c from the nucleus. The resulting pseudo-wavefunctions $\psi_l^{\mathrm{ps}}(\mathbf{r})$, for each angular momentum l should be equal to the all-electron wavefunctions $\psi_l^{\mathrm{ae}}(\mathbf{r})$ outside the core region and nodeless inside the core regions, in such a way that a smaller number of plane waves is required:

$$\psi_l^{\mathrm{ps}}(\mathbf{r}) = \psi_l^{\mathrm{ae}}(\mathbf{r}) \quad (r \geq r_c) \qquad\qquad \psi_l^{\mathrm{ps}}(\mathbf{r}) \quad \text{nodeless}\,. \tag{4.29}$$

The pseudopotentials are built for single, isolated atoms on a given reference atomic configuration, and further constraints must be satisfied, first of all the orthonormality of the pseudo-wavefunctions:

$$\langle \psi_i^{\mathrm{ps}}(\mathbf{r}) | \psi_j^{\mathrm{ps}}(\mathbf{r}) \rangle = \delta_{i,j} \tag{4.30}$$

The eigenvalues associated to the all-electron wavefunction and to the corresponding pseudo-wavefunction must be equal:

$$\epsilon_l^{ps} = \epsilon_l^{ae}\,. \tag{4.31}$$

The first and the second derivative of each $\psi_l^{\mathrm{os}}(\mathbf{r})$ must be equal to those of $\psi_l^{\mathrm{ae}}(\mathbf{r})$ at the cutoff radius:

$$\left.\frac{\partial \psi_l^{\mathrm{ps}}(\mathbf{r})}{\partial r}\right|_{r=r_c} = \left.\frac{\partial \psi_l^{\mathrm{ae}}(\mathbf{r})}{\partial r}\right|_{r=r_c}, \qquad \left.\frac{\partial^2 \psi_l^{\mathrm{ps}}(\mathbf{r})}{\partial r^2}\right|_{r=r_c} = \left.\frac{\partial^2 \psi_l^{\mathrm{ae}}(\mathbf{r})}{\partial r^2}\right|_{r=r_c}. \tag{4.32}$$

In norm-conserving pseudopotentials (NCPP) the total electronic charge of the pseudo-wavefunctions inside the cut-off radius is equal to the corresponding all-electron orbitals:

$$\int_{r<rc} |\psi_l^{\mathrm{ps}}(\mathbf{r})|^2 r^2 dr = \int_{r<rc} |\psi_l^{\mathrm{ae}}(\mathbf{r})|^2 r^2 dr \,. \tag{4.33}$$

Traditionally, NCPP, are composed of a local and non-local component, the former describing the long-range interaction outside the core, while the latter is a short-range potential, specific for each angular momentum [73]:

$$V^{ps}(\mathbf{r}) = V_{loc}(r) + \sum_l V_l \left|l\right\rangle \left\langle l\right| \,. \tag{4.34}$$

An important properties for a good pseudopotential is the transferability, which is the ability of the pseudopotential to reproduce the all-electron calculations for a certain range of energies about ϵ_l. The logarithmic derivative of the pseudo-wavefunction is a good parameter to evaluate the transferability of a pseudopotential. The transferability is good if the logarithmic derivative of the pseudo-wavefunction is comparable to that of the all electron calculation through a large range of energy. In this case, it is safe to use the pseudopotential in a chemical environment different from the one used to construct the pseudopotential.

A breakthrough in the pseudopotential theory came when Vanderbilt proposed to relax the norm conservation condition (4.33) in order to generate softer pseudopotentials [74]. In the ultrasoft pseudopotentials (USPP) scheme, the pseudo-wavefunction are as smooth as possible in the core region, requiring an even smaller kinetic energy cutoff. However, in this formalism the orthonormality of the electronic wavefunctions occurs via an overlap matrix:

$$\langle \psi_i^{\mathrm{ps}}(\mathbf{r}) | S | \psi_j^{\mathrm{ps}}(\mathbf{r}) \rangle = \delta_{i,j} \,, \tag{4.35}$$

and the charge density contains an additional term, the so-called augmentation charge, which requires a kinetic energy cutoff higher than four times the E_{cut}.

A more elaborate representation of the pseudopotential is the projector augmented wave (PAW) method, which consists in reconstructing the all-electron wave function from the pseudo-wavefunction [75]. The calculation consists in a plane wave part and several one-center terms, whose interaction is removed by introducing a compensation charge. The USPP and the PAW formalisms guarantee high-accuracy results with a lower computational effort.

In recent years, a method to construct optimized norm-conserving pseudopotentials following the USPP construction algorithm without renouncing the norm conservation has been proposed [76]. The resulting optimized norm-conserving Vanderbilt (ONCV)

pseudopotentials have an accuracy comparable to the USPP at a moderately higher kinetic energy cutoff [77].

4.1.6 Failures of DFT

In practical applications, DFT has shown much success but also several drawbacks, which are not failures of the theory itself but limitations of the approximated exchange-correlation functionals [78].

A well-known limitation of DFT is the underestimation of the band gap of semiconductor and insulator materials. The Kohn-Sham eigenvalues ϵ_i are purely mathematical objects, eigenvalues of the auxiliary Hamiltonian, but without a precise physical meaning, with the exception of the HOMO, which corresponds to the first ionization energy if the (unknown) exact exchange-correlation functional is employed [79]. However, even for exact DFT, there is not an analogous theorem that identifies the LUMO with the electron affinity. Therefore, the interpretation of ϵ_{LUMO}-ϵ_{HOMO} as the fundamental band gap of the interacting system is in principle wrong, even though it can serve (and is vastly used) as an approximation for the fundamental gap and is used as a starting point for perturbative approaches, as in many body perturbation theory, that can provide accurate approximations for electron addition/removal energies. A large part of the error is due to a missing term coming from the discontinuity of the derivatives of the exchange-correlation functional [80].

The local nature of the LDA/GGA functionals does not allow a correct descriptions of interactions with a nonlocal character, such as the van der Waals interactions. The long-range attractive part, decaying as $1/R^6$ cannot be reproduced by these local fuctionals.

An important failure occurring not only in complicated systems, but also in the simplest molecules, such as stretched H_2 or H_2^+, is the so-called self-interaction error. The binding energy of the H_2^+ at large distances is severely underestimated ($50-60$ kcal/mol) by any exchange-correlation functional. The failure in this simple one-electron system, which can be easily solved in a wavefunction-based approach, resides in the fact that DFT treats individual electrons through their total density and the single electron interacts unphysically with the field it generates. This is known as self-interaction error which is not canceled in the DFT scheme as it is, for instance, in the Hartree-Fock theory.

The self-interaction error affects also more complicated systems, favoring delocalized charge distributions. The total energy of a system with a fractional number of electrons $(N + \delta)$ is a linear interpolation between the total energies of the two nearest systems

with an integer number of electrons $E(N+\delta) = (1-\delta)E(N)+\delta E(N+1)$ [79]. However, LDA/GGA functionals show a convex behavior for fractional charges, deviating from the exact piece-wise linearity. As a consequence of this convex behaviour, fractional charges or delocalized charge distributions have a lower energy than integer or localized states. This is particularly true for strongly correlated materials, with localized electronic states originating from d or f atomic orbitals. For instance, in TM oxides LDA/GGA may fail not only underestimating the band gap, but predicting a metallic character and a wrong magnetic state [81]. As we are going to explain in the next sections, better results for TM oxides can be achieved if the energy functional is corrected adding a a Coulomb repulsion U which resembles the Hubbard model, or a fraction of exact, Hartree-Fock exchange.

4.1.7 DFT + U

The basic idea behind the DFT+U approach [82, 83] is to correct the DFT energy functional with a static mean-field Hubbard-like correction that acts specifically on the correlated d electrons:

$$E_{\mathrm{DFT}+U}[n(\mathbf{r})] = E_{\mathrm{DFT}}[n(\mathbf{r})] + E_{\mathrm{Hub}}[\{n_m^{I\sigma}\}] - E_{\mathrm{dc}}[\{n^{I\sigma}\}] \,. \tag{4.36}$$

The second term in the right-hand side of Eq.(4.36) corresponds to the Hubbard correction that acts on a selected set of atomic orbitals, whose occupation numbers are represented by $\{n_m^{I\sigma}\}$, while E_{dc} is a double counting term that removes correlation effects already treated by the DFT functional in an average way. The occupation numbers $\{n_m^{I\sigma}\}$ are the eigenvalues of the 5×5 occupation matrix $n_{mm'}^{I\sigma}$, defined as the projection of the Kohn-Sham state $|\psi_{\mathbf{k}v}^{\sigma}\rangle$, with occupation $f_{\mathbf{k}v}^{\sigma}$, onto the five d atomic orbitals ϕ_m^I of the atom at site I:

$$n_{mm'}^{I\sigma} = \sum_{\mathbf{k},v} f_{\mathbf{k}v}^{\sigma} \, \langle \psi_{\mathbf{k}v}^{\sigma} | \phi_{m'}^{I} \rangle \, \langle \phi_{m}^{I} | \psi_{\mathbf{k}v}^{\sigma} \rangle \ . \tag{4.37}$$

In the simplified rotational-invariant formulation of the DFT+U [81] the correction applied to the energy functional reads:

$$\begin{aligned} \Delta E_U[\{n_{mm'}^{I\sigma}\}] &= E_{Hub}[\{n_{mm'}^{I\sigma}\}] - E_{dc}[\{n^{I\sigma}\}] \\ &= \frac{U}{2} \sum_{I} \sum_{m,\sigma} \left[n_{mm}^{I\sigma} - \sum_{m'} n_{mm'}^{I\sigma} n_{m'm}^{I\sigma} \right] \\ &= \frac{U}{2} \sum_{I,\sigma} \mathrm{Tr}[\mathbf{n}^{I\sigma}(1-\mathbf{n}^{I\sigma})] \,. \end{aligned} \tag{4.38}$$

If the representation that diagonalizes the occupation matrix, $\mathbf{n}^{I\sigma}\mathbf{v}_m^{I\sigma} = n_m^{I\sigma}\mathbf{v}_m^{I\sigma}$ is chosen, then the Eq.(4.38) becomes:

$$\Delta E_U[\{n_{mm'}^{I\sigma}\}] = \frac{U}{2}\sum_{I,\sigma}\sum_{m} n_m^{I\sigma}(1 - n_m^{I\sigma})\,. \tag{4.39}$$

The correction acts like a penalty function, destabilizing any fractional occupancy of the orbitals and therefore favoring fully occupied ($n_m^{I\sigma} \simeq 1$) or unoccupied ($n_m^{I\sigma} \simeq 0$) d states. An orbital-dependent correction term is added in the Kohn-Sham effective potential:

$$V_U = \frac{\delta\,\Delta E_U[\{n_{mm'}^{I\sigma}\}]}{\delta n(\mathbf{r})} = U\sum_{I,m}\left(\frac{1}{2} - n_m^{I,\sigma}\right)|\phi_m^I\rangle\,\langle\phi_m^I|\,, \tag{4.40}$$

acting on the Kohn-Sham eigenvalues $\epsilon_{\mathbf{k}v}$ in the following way:

$$\begin{aligned}\epsilon_{\mathbf{k}v}^{\sigma\,\mathrm{DFT}+U} &= \epsilon_{\mathbf{k}v}^{\sigma\,\mathrm{DFT}} + \langle\psi_{\mathbf{k}v}^{\sigma}|\,V_U\,|\psi_{\mathbf{k}v}^{\sigma}\rangle \\ &= \epsilon_{\mathbf{k}v}^{\sigma\,\mathrm{DFT}} + U\sum_{I,m}\left(\frac{1}{2} - n_m^{I,\sigma}\right)|\,\langle\phi_m^I|\psi_{\mathbf{k}v}^{\sigma}\rangle\,|^2\,.\end{aligned} \tag{4.41}$$

The value of the U parameter is linked, via Janak's theorem [84], to the linear response properties of the system [81] and it can be computed from the derivatives of the Hubbard-site occupations with respect to a small perturbing potential, α,

$$U_0 = \left(\chi_0^{-1} - \chi^{-1}\right)_{II} = \frac{\partial\alpha_I^{\mathrm{KS}}}{\partial n_I} - \frac{\partial\alpha_I}{\partial n_I}\,, \tag{4.42}$$

where χ_0 and χ are the matrices constructed from the initial, bare response and full self-consistent response to the applied α. This linear-response formalism was introduced on top of the DFT ground state. However, the Hubbard correction should be derived from the linear response properties of the DFT+U ground state itself [85], especially in systems in which qualitative differences exist between the properties of a DFT and DFT+U solution. If U_{in} is the Hubbard parameter introduced in a calculation and U_{out} the resultant linear response correction, then it holds that [85]

$$U_{\mathrm{out}} = U_{\mathrm{scf}} - \frac{U_{\mathrm{in}}}{m}\,, \tag{4.43}$$

in the range where $U_{\mathrm{in}} \approx U_{\mathrm{scf}}$ [85]. Here, $m = \frac{1}{\sum_i (a_i^I)^2}$ can be thought as the effective degeneracy of the orbitals involved in the perturbation, where a_I are the linear order coefficients in the change of the occupations numbers produced by U. Therefore, from a series of linear response calculations for different values of U_{in} it is possible to extract a value for U_{scf} [85].

The advantage of the self-consistent correction (U_{scf}) is that it specifically removes the unphysical curvatures in the total energy versus occupation plots and the spurious

minima for non-integer orbital occupations, restoring the piece-wise linearity between N and $N \pm 1$ electron states. In this sense, U_{scf} can be effectively interpreted as the curvature of the DFT energy for fractional occupations, which is associated to the self-interaction error.

4.1.8 Hybrid functionals

Hybrid functionals [86], which contain a fraction of exact, non-local Hartree-Fock exchange, serve as an alternative to the Hubbard-U approach in the modelling of transition metal oxides, and can overcome some of the limitations associated with local and semilocal functionals [87]. The mixing of the HF and DFT exchange functionals can be achieved in variety of ways [88–91], with the possibility to treat the long- and short-range components of the exact interaction separately [92, 93].

PBE0 and HSE functionals are two hybrid functionals which make use of the PBE correlation energy and they differ most notably in the treatment of the exact-exchange term. PBE0 is not range-separated, and therefore adopts the form

$$E_{xc}^{\mathrm{PBE0}} = \alpha E_x^{\mathrm{HF}} + (1-\alpha) E_x^{\mathrm{PBE}} + E_c^{\mathrm{PBE}}\,, \tag{4.44}$$

with $\alpha = \frac{1}{4}$ in the original formulation [90, 91]. On the other hand, HSE is range-separated; this means that only the short range HF exchange interaction is mixed into the functional and the long range component is treated at the PBE-level

$$E_{xc}^{\omega,\mathrm{HSE}} = \alpha E_x^{\mathrm{HF,SR}}(\omega) + (1-\alpha) E_x^{\mathrm{PBE,SR}}(\omega) + E_x^{\mathrm{PBE,LR}}(\omega) + E_c^{\mathrm{PBE}}\,. \tag{4.45}$$

An additional parameter ω is introduced, which determines the partitioning of the Coulomb potential into the short-range and the long-range components [93]. The HSE functional, which reportedly gives excellent results for a wide range of materials [94], has values of $\alpha = \frac{1}{4}$ and $\omega = 0.11\ \ (\mathrm{a.u.})^{-1}$ [95].

Like the Hubbard U correction, the fraction of HF exchange can be tuned by hand to reproduce experimental quantities [96–98]. However, an optimal and physically motivated value for α has also been proposed by Alkauskas et al. [98] as the reciprocal of the macroscopic dielectric constant of the material $\alpha = 1/\epsilon_\infty$ [98]. If the non-local hybrid exchange-correlation potential is compared with the statically screened GW self-energy (COHSEX [99]), the relation $\alpha = 1/\epsilon_\infty$ emerges naturally. Considering for instance the long-range part of the PBE0 exchange-correlation potential: it depends on α as $-\alpha/(|\mathbf{r}-\mathbf{r}'|)$, while in the COHSEX approximation the long-range part is dominated by the screened exchange $-1/(\epsilon_\infty(|\mathbf{r}-\mathbf{r}'|))$ [98]. Therefore, the value of α could be determined self-consistently, iterating hybrid calculations with $\alpha^{\mathrm{new}} = 1/\epsilon_\infty^{\mathrm{old}}$ until ϵ_∞

is converged [100]. If the self-consistent value of α is employed, the predicted bandgap and the dielectric constant of a large set of compounds is in excellent agreement with their experimental counterparts. Thus, if the starting guess of ϵ_∞ is good enough, a one-shot calculation with $\alpha = 1/\epsilon_\infty$ leads to accurate results, even without performing the self-consistent procedure.

4.2 Ab-initio thermodynamics

From DFT calculations it is possible to make predictions about the electronic structure and many other properties of materials at the atomistic level at zero temperature and pressure. The *ab-initio* thermodynamics is a multi-scale approach in which the information obtained at the microscale are used to calculate several macroscopic properties of realistic materials at finite temperature and pressure [101–103]. The key ingredient is to calculate in an accurate way thermodynamic potential functions from which the macroscopic properties of the system can be computed using the standard tools of the thermodynamics. The Gibbs free energy G is the appropriate thermodynamic potential for system under conditions of fixed temperature and pressure.

The potential energy surface (PES) obtained from DFT calculations serves as an input parameter to calculate the Gibbs free energy. In particular, the position and the energy of the minima in the PES are the important quantities. Indeed, we treat various possible phases of the system one by one assuming that each one of them is in equilibrium with the environment, and then we try to predict the relative stability of the various phases comparing their free energy. The formalism can be applied in different fields, from bulk phases to surfaces and interfaces.

In the former case, *ab-initio* thermodynamics allows to compute the formation free energy of bulk compounds from the elementary constituents:

$$\Delta G^f = G_p - \sum_r G_r \,, \tag{4.46}$$

where G_p and G_r are the free energy of the product and the reactants, respectively. The Gibbs free energy can be decomposed as:

$$G = E_{\text{total}} + F_{vib} + F_{el} + F_{rot} + F_{trans} + pV \,, \tag{4.47}$$

where E_{total} is the total internal energy, F_{el} is the electronic free energy, F_{vib}, F_{rot} and F_{trans} are the vibrational, rotational and translational free energies, respectively. These physical quantities can be computed from DFT calculations:

- E_{total} is replaced with the DFT total energy of the optimized geometry, corresponding to the minimum of the PES:

$$E_{total} = E_0^{DFT} \,. \tag{4.48}$$

  The DFT total energies are not physically meaningful quantity, because they depend on the choice of the pseudopotential, yet in *ab-initio* thermodynamics what really matters are the energy differences.

- The vibrational free energy is computed from the phonon dispersion as:

$$F_{vib} \approx k_B T \int \ln\left(\frac{h\nu}{2k_B T}\right) d\nu \,, \tag{4.49}$$

  where $g(\nu)$ is the phonon density of states.

- The electronic free energy F_{el} at a temperature T corresponds to $[E_{el}(T) - E_{el}(0)] - TS_{el}$, where S_{el} is the electronic entropy. In the approximation of slowly varying electronic density of states at the Fermi level $g(E_F)$

$$F_{el} \approx -\frac{\pi^2}{6} k_B^2 T^2 g(E_F) \,. \tag{4.50}$$

  The contribution of F_{el} is usually small and neglected in the practical calculations.

- F_{rot} and F_{trans} are commonly neglected for fixed solids, while they could play a role if one, or more, among the reactants or the products is in the gaseous phase. In this case, their contribution in the total entropy is already contained in the values reported in thermochemical tables [104].

- The volumetric contribution pV is usually small and neglected in the practical calculations.

The energy difference ΔE is the dominant contribution in the free energy difference (4.46). Although not negligible, the vibrational contribution is far lower than the energetic one and is sometimes not taken into account because it is comparable to the numerical accuracy of the calculation [101].

The free energies G appearing in Eq.(4.46) depend on the size of the cell employed in DFT calculations. In general, it is convenient for bulk systems to adopt a free energy per formula unit, which is equivalent to the chemical potential μ for an infinite, homogeneous system. Eq.(4.46) then becomes:

$$\Delta G^f = G_p - \sum_r \mu_r \,. \tag{4.51}$$

The reactants are taken from their reservoirs paying an energetic cost μ and then combined to form the product, gaining a free energy G_p. The difference among these energies provides the formation free energy which can be compared with the experimental values and can be used to construct phase diagrams to evaluate the stability of the different phases at a certain temperature and pressure.

Moreover, for bulk materials the *ab-initio* thermodynamic approach allows to predict the type and number of defects that can form as a function of thermodynamic variables [105, 106]. Several methods have been devised also to deal with charged defects [107].

The same concept of computing free energy differences can be employed to investigate the relative thermodynamic stability of the different surfaces of a particular material. The simplest model consists in a surface in equilibrium with the underlying bulk material, which acts as a thermodynamic reservoir, and a surrounding gas atmosphere at a certain temperature and pressure. An additional term γA, which represents the energy cost of introducing a surface with area A in the system, is added in the expression of the Gibbs free energy. The thermodynamic stability is then assessed by comparing the surface free energies γ of different surface structures for different environmental conditions:

$$\gamma = \frac{1}{A}\left(G - \sum_i n_i \mu_i(T,p)\right) \quad , \tag{4.52}$$

where G is the Gibbs free energy of the employed supercell, n_i the number of atoms of the i-th species and the temperature and pressure dependence is contained in the chemical potentials. For instance, if one of the reactants is gaseous oxygen, then the corresponding chemical potential is:

$$\mu_O(T,p) = \frac{1}{2}E^{mol}_{O_2} + \Delta\mu_O(T,p_0) + \frac{1}{2}k_B T \ln\left(\frac{p}{p_0}\right), \tag{4.53}$$

where the temperature dependence of the chemical potential at 1 bar $\Delta\mu_O(T,p_0)$ can be computed from the thermochemical data reported in the NIST-JANAF database [104]:

$$\Delta\mu_O(T,p_0) = \frac{1}{2}\left(\Delta H_{O_2}(T,p_0) - T\Delta S_{O_2}(T,p_0)\right) . \tag{4.54}$$

The most stable surface as a function of temperature and pressure can be found combining Eq.(4.52) and Eq.(4.53).

4.3 Computational hydrogen electrode

The free energy change of electrochemical reactions, involving proton-electron transfer cannot simply be described by Eq.(4.46), but requires additional terms. Nørskov et al. developed a method, which is referred to as the computational hydrogen electrode (CHE), to compute the free energy of the intermediates of electrochemical reactions, under applied bias, from first-principles [108]. In this approach, voltages are referred to SHE, as the equilibrium between $H^+ + e^-$ and $1/2\ H_2$ at pH=0 and standard temperature and pressure conditions, $T = 298.15$ K and $p = 1$ bar. As a consequence, at these conditions the following relation holds:

$$\frac{1}{2}G(\mathrm{H}_{2,gas}) = \mu(e^-) + \mu(H^+)\,. \tag{4.55}$$

When the pH is different from 0, the variation of chemical potential of protons is $-RT\ln 10\,\mathrm{pH}$ while when a bias is applied, the electrons acquire a chemical potential equal to eV_{SHE}.

The first step of the HER (Volmer step, cf. Eq.(2.13)) consists in the adsorption of a hydrogen atom on an active site on the surface. The hydrogen coverage at specific electrochemical conditions depends on the thermodynamics of the Volmer step, which can be evaluated comparing the free energy of adsorption:

$$\begin{aligned}
\Delta G(NH, V_{\mathrm{RHE}}) &= G_{\mathrm{slab}+NH} - [G_{\mathrm{slab}} + N_H(\mu_{e^-} + \mu_{H^+})] \\
&= G_{\mathrm{slab}+NH} - \left(G_{\mathrm{slab}} + \frac{N_H}{2}G_{\mathrm{H}_{2,\mathrm{mol}}}\right) - N_H(-RT\ln 10\,\mathrm{pH} + eV_{\mathrm{SHE}}) \\
&= \Delta G^{ads}_{NH} - eN_H\,V_{\mathrm{RHE}} \quad ,
\end{aligned} \tag{4.56}$$

where the subscripts *slab* and *slab*$+N_H$ refer to the pristine slab and the slab with N_H adsorbed hydrogen atoms, respectively. Given the definition of RHE, as in Eq.(7.11), the dependence on the chemical potentials of protons and electrons is incorporated into the compact form eV_{RHE}. The free energy of adsorption ΔG^{ads}_{NH} is computed as:

$$\Delta G^{ads}_{NH} = \Delta E^{ads}_{NH} + \Delta E_{\mathrm{ZPE}} - T\Delta S \quad , \tag{4.57}$$

where $T\Delta S$ and ΔE_{ZPE} are the energy changes due to entropic and zero-point effects and $\Delta E^{ads}_{\mathrm{H}^*}$ is the DFT adsorption energy. In general, the calculation of the adsorption energy $\Delta E^{ads}_{\mathrm{H}^*}$ is performed in vacuum, neglecting the effect of the solvent and the double layer. Although the effect of the solvent is usually small, there are cases in which it could have an impact in the calculation of the binding energy of the intermediates [109].

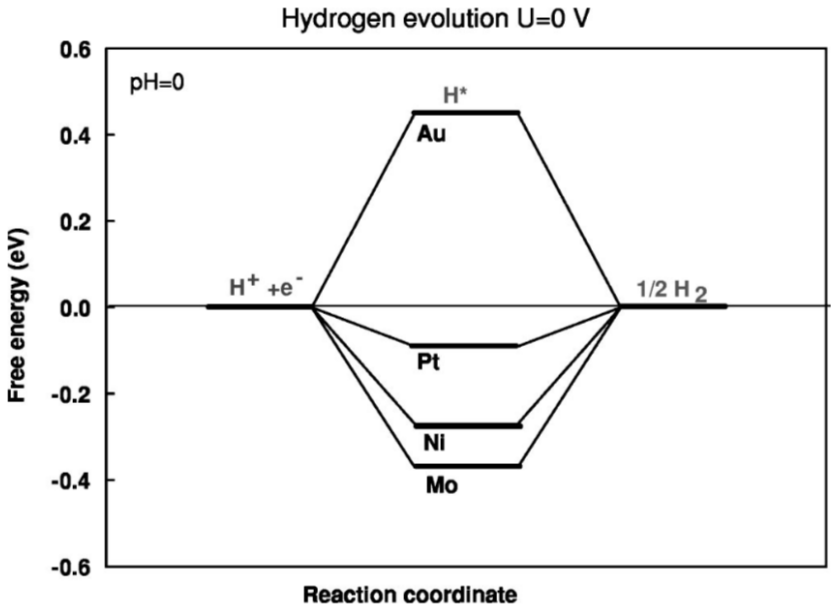

Figure 4.1

Free energy diagram for hydrogen evolution on different metals, taken from Ref.[110].

The CHE was used to compute the hydrogen adsorption energy on different transition and noble metals [110]. The free energy diagram for the electrochemical HER on different metals is reported in Figure 4.1, taken from Ref.[29]. The first step represents the proton discharge on the metal surface, followed by the hydrogen desorption. At zero potential, the initial and the final state have the same free energy, according to Eq.(4.55), while the free energy of the intermediate is determined by the hydrogen adsorption free energy. The well-known catalytic activity of Pt is due to an adsorption free energy close to zero, in such a way that no significant thermodynamic barriers are present neither in the adsorption nor in the desorption processes. Au shows a barrier of the 0.5 eV for the adsorption process, which inhibits the first step of the HER. Conversely, Ni and Mo have a large barrier for the desorption, indicating that the hydrogen are too largely bound for an efficient HER.

The CHE technique was used later to construct surface Pourbaix diagrams, describing the coverage of the adsorbates as a function of the pH and the applied potential [111–116].

4.4 Band edge alignment

A favorable alignment of the CBM edge with the redox potentials of water is a key ingredient to allow the light-driven HER. Different methods proposed to predict the band alignment from *ab-initio* calculations have been proposed with different levels of accuracy [117–124]. In the simplest schemes, the band edge at the semiconductor-water interface were taken equal to the ionization potential and the electron affinity computed at the *GW* level [122]. However, neglecting the atomistic structure at the interface could lead to significant errors, since the orientation of the dipoles at the interface plays an important role. In other studies, the atomistic interface was explicitly considered, but the structure was not equilibrated, and the results may suffer from the incorrect orientation of surface dipoles [117]. The band edge alignment could be computed with an implicit solvent model with high accuracy, provided that the first layer of water molecules is explicitly taken into account [124].

In this work, we follow the approach of Guo et al. [123], which consists in three independent steps, as it was also reported in earlier studies [118, 120, 121]. The scheme of this procedure is reported in Figure 4.2, taken from Ref.[123].

First of all, an accurate description of the band edges ϵ_v and ϵ_c of the bulk material is required, in order to refer them to the average electrostatic potential in the unit cell V_{sc}(bulk), which is commonly set to zero in periodic boundary conditions codes.

Second, the standard hydrogen electrode (SHE) redox level μ_{SHE} must be aligned with the average electrostatic potential of water V_w(bulk). A computational version of the SHE has been reported as the reduction potential of an hydronium ion into gaseous hydrogen [118, 125] and the alignment between this level and the average electrostatic potential of water has been computed with the same computational setup adopted in this work [125]. Therefore, we adopted the values reported by Ambrosio et al. [125], which found the vacuum level to be 3.69 eV higher in energy than the average electrostatic potential of water, and the SHE 4.56 eV below the vacuum level [125], in good agreement with the value proposed by Trasatti, 4.44 eV [34]. According to this scheme, μ_{SHE} lies -0.87 eV below V_w(bulk). These aligning terms were obtained combining ab-initio molecular dynamics (AIMD) simulations with the thermodynamic integration method.

The band alignment at the semiconductor-water interface is due to electrostatic effect depending on the electrons and ions redistribution near the interface. Therefore, in the final step, the profile of the electrostatic potential across the CFO/water interface is computed through the analysis of several snapshots of AIMD simulations. This step

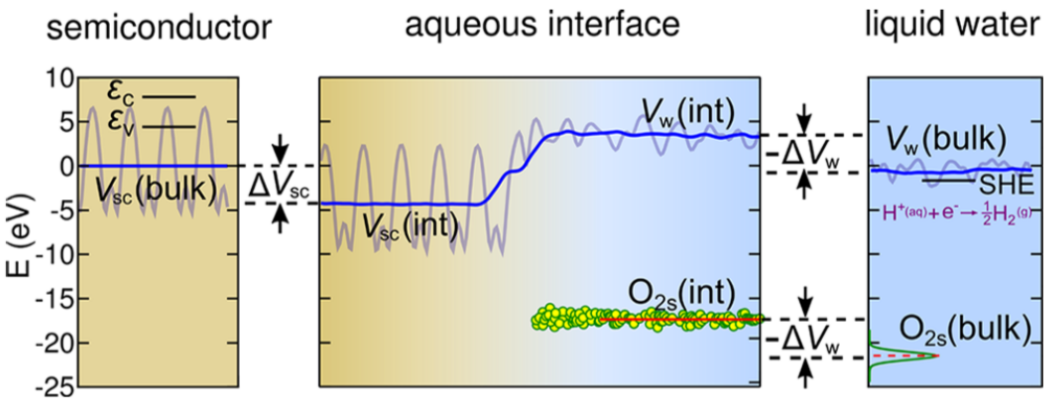

Figure 4.2

Schematic representation of the band alignment at the semiconductor-water interface. In the left panel, the conduction and valence band edges (ϵ_c and ϵ_v) of the semiconductor are shown with respect to the electrostatic potential (gray) and its average V_{sc}(bulk). Similarly, on the right, the SHE level is given with respect to the electrostatic potential (gray) and its average V_w(bulk) in liquid water. The line-up between the electrostatic potentials V_{sc}(int) and V_w(int) is illustrated in the middle panel. The figure also illustrates the alternative but equivalent alignment in liquid water through the average O 2s level. Figure taken from Ref.[123].

allows us to determine the difference of the electrostatic potential between bulk water V_w(int) and bulk CFO V_{sc}(int) across the solid/liquid interface, which depends on the specific surface termination considered. The electrostatic potentials computed in this last step are aligned with those of the semiconductor and water in their bulk phases:

$$\Delta V_{sc} = V_{sc}(\text{bulk}) - V_{sc}(\text{int}) \tag{4.58}$$

$$\Delta V_w = V_w(\text{bulk}) - V_w(\text{int})\,. \tag{4.59}$$

Finally, all the ingredients are put together and the band edges relative to SHE are computed as:

$$E_{VBM} = \epsilon_v - \mu_{SHE} - \Delta V_{sc} + \Delta V_w \quad , \tag{4.60}$$

$$E_{CBM} = \epsilon_c - \mu_{SHE} - \Delta V_{sc} + \Delta V_w \quad . \tag{4.61}$$

The AIMD simulations can be compared with experiments performed at the pH corresponding to the point of zero charge (PZC). If this is not the case and the reference experiment is performed at a different pH, the computed bands can be shifted to the

pH of interest, assuming a Nernstian dependence on the pH [5, 126]:

$$E_{\mathrm{VBM}}(\mathrm{pH}) = E_{\mathrm{VBM}}(\mathrm{pH_{PZC}}) + (0.059\ \mathrm{V}) \times (\mathrm{pH_{PZC}} - \mathrm{pH}) \quad , \tag{4.62}$$

$$E_{\mathrm{CBM}}(\mathrm{pH}) = E_{\mathrm{CBM}}(\mathrm{pH_{PZC}}) + (0.059\ \mathrm{V}) \times (\mathrm{pH_{PZC}} - \mathrm{pH}) \quad . \tag{4.63}$$

4.5 Maximally localized Wannier functions

Orbitals that are degenerate in an isolated atom, like the Fe $3d$ states, can interact differently with the ligands present in the crystal, e.g. the O atoms, resulting in a loss of degeneracy. Both the electrostatic field generated by the ligands and the hybridization between metal and ligand orbitals contribute to the crystal field splitting. The different contributions to the crystal field splitting can be evaluated using the concept of the Wannier functions.

Wannier functions [127] are spatially localized functions that represent an alternative to Bloch states for the description of the electronic states in periodic crystalline solids. A set of N Wannier functions $|w_{n,\mathbf{R}}\rangle$, characterized by a unit cell vector $\mathbf{R}$ and a band index n, can be constructed from a set of N Bloch states $|\psi_{n,\mathbf{k}}\rangle$ via a unitary transformation:

$$|w_{n,\mathbf{R}}\rangle = \frac{V}{(2\pi)^3} \int_{BZ} d\mathbf{k}\, e^{-i\mathbf{k}\cdot\mathbf{R}} \sum_{m=1}^{N} U_{mn}^{(\mathbf{k})} |\psi_{n,\mathbf{k}}\rangle \ , \tag{4.64}$$

where V is the volume of the unit cell and $U_{mn}^{(\mathbf{k})}$ are matrix elements of a unitary matrix $\mathbf{U}$ that mixes the Bloch states at a specific $\mathbf{k}$-point. Given a set of N Bloch states, the N Wannier functions are not uniquely defined, because of the arbitrariness in the choice of $\mathbf{U}$. A method for obtaining the optimally localized set of Wannier functions has been developed by Marzari and Vanderbilt [128], choosing the transformation $\mathbf{U}$ that minimized the total quadratic spread of the Wannier orbitals, and resulting in the so-called maximally localized Wannier functions (MLWF):

$$\Omega = \sum_{n} \left[\langle w_{n\mathbf{0}}(\mathbf{r}) | \, r^2 \, | w_{n\mathbf{0}}(\mathbf{r}) \rangle - | \langle w_{n\mathbf{0}}(\mathbf{r}) | \, \mathbf{r} \, | w_{n\mathbf{0}}(\mathbf{r}) \rangle |^2 \right] . \tag{4.65}$$

This method was first proposed for a group of well isolated Bloch states, but it was later extended to the case of entangled bands, which cross other states throughout the Brillouin zone [129].

Once the matrix $\mathbf{U}$ is determined, the Hamiltonian in the Wannier basis reads as:

$$\hat{H} = \sum_{n,m,\mathbf{R},\mathbf{R}'} h_{n,\mathbf{R},m,\mathbf{R}'}\, \hat{c}^{\dagger}_{n\mathbf{R}} \hat{c}_{m\mathbf{R}'} \ , \tag{4.66}$$

where $\hat{c}^{\dagger}_{n\mathbf{R}}$ and represent $\hat{c}_{n\mathbf{R}}$ the creator and the annihilation operators for an electron in the Wannier orbital $|w_{n\mathbf{R}}\rangle$, while $h_{n,\mathbf{R},m,\mathbf{R}'}$ are the matrix elements defined as:

$$h_{n,\mathbf{R},m,\mathbf{R}'} = \frac{V}{(2\pi)^3} \int_{BZ} d\mathbf{k}\, e^{i\mathbf{k}\cdot(\mathbf{R}-\mathbf{R}')} \sum_i (U^{(\mathbf{k})}_{in})^* \epsilon_{i\mathbf{k}} \, (U^{(\mathbf{k})}_{im}) \,. \tag{4.67}$$

The diagonal terms $h_{n,\mathbf{R},n,\mathbf{R}}$ can be interpreted as the on-site energies in a tight-binding model, while the off-diagonal terms assume the role of the hopping amplitudes between two different Wannier orbitals [130].

The MLWFs in Eq.(5.1) can be constructed starting from different sets of Bloch states, each one of them corresponding to a different tight-binding model. If only Bloch states with a specific character are included in the summation, the resulting Wannier functions have the main orbital character. However, the tails spread to neighboring sites that hybridize with the central orbital and the final MLWF also retains the character of the surrounding sites. On the other hand, if more bands are included in the summation, hybridization effects are gradually removed and each MLWF has a reduced mixing with the other orbitals on neighboring sites.

This method was applied to investigate the crystal field parameters in perovskites [130] and in two-dimensional transition metal dichalcogenides [131]. Therefore, the difference between the on-site energies converges to a value that can be interpreted as a working definition of the pure electrostatic contribution to the crystal field, when the hybridization is gradually removed adding more bands in Eq.(5.1).

5

Electronic Structure of bulk $CuFeO_2$

CONTENTS

A detailed understanding of the electronic structure of the bulk phase of CFO is the first step towards its characterization as a photocathode. The energy level alignment is one of the important factors that determines the PEC performance of a material. In this sense, it is important to have an accurate description of the electronic structure of the bulk phase for the level alignment procedure. DFT is a powerful tool for accurately describing the electronic properties of materials, yet overcoming its well-known limitations is important for predicting reasonable properties.

We have benchmarked the most popular formulations for the treatment of the electron exchange and correlation interactions, highlighting their strengths and weaknesses in predicting electronic structures compatible with the available spectroscopic measurements [2]. In this chapter, we report in detail the outcomes of our theoretical investigation, analyzing how different exchange-correlation functionals describe quantities like the bandgap, the position of Fe, Cu and O-derived electronic states, the crystal field splitting of the Fe 3d states, comparing them with the available spectroscopic measurements. Moreover, we focus on aspects that have not been treated specifically in previous theoretical studies, in particular the origin of the t_{2g}-e_g splitting and how these states are affected by the Hubbard U correction.

5.1 Experimental characterization of the electronic structure of $CuFeO_2$

The electronic structure of CFO has been well characterized experimentally. The first x-ray photoemission experiment, carried out by Galakhov et al. [132], aimed at investigating the valence manifold. A comparison of the Cu $L\alpha$, Fe $L\alpha$ and O $K\alpha$ spectra revealed that the highest occupied states have mainly a Cu d character, while Fe d and O p states lie deeper in energy. In the same work, the oxidation state of each of the ions has been determined and the Cu ions were found to be in the Cu^{1+} oxidation state and the Fe^{3+} ions in the high-spin S= 5/2 configuration. Subsequently, x-ray absorption experiments have been carried out to characterize the lowest unoccupied states [133]. Inspecting the low-energy absorption edge, the main contribution to the bottom of the conduction band has been attributed to Fe $3d$ and O $2p$ states. Moreover, the O K-edge x-ray absorption spectrum (XAS) reveals partial $3d$ holes on the Cu ions, indicating a not completely filled $3d$ shell ($3d^{10-x}$). The visible absorption edges, investigated with resonant inelastic X-ray scattering (RIXS) spectroscopic measurements, correspond to Cu $\rightarrow$ Fe charge transfer [10].

Recent spectroscopic ellipsometry experiments [10] measured an optical bandgap of 1.43 eV, in agreement with a previous indirect estimate, 1.5 eV, based on the analysis of the Mott-Schottky diagram [7]. To the best of our knowledge, a combined photoemission-inverse photoemission experiment to determine the quasi-particle bandgap has not yet been reported.

The first theoretical investigation of CFO in the framework of the Density Functional Theory (DFT) appeared in 1997 [132]. In that work, the authors applied the LSDA($+U$) approach to study the density of states, comparing it with x-ray photoelectron spectra. Subsequent theoretical studies focused on the electronic structure of general Cu-based delafossite compounds [134, 135] or specifically on the multiferroicity of CFO [136, 137]. PBE+U and HSE calculations, aimed at supporting optical spectroscopic and PEC measurements, appeared recently in the literature [10, 138]. The general idea that emerges from these works is that the bare PBE fails in describing the electronic structure of CFO and corrections must be introduced in the exchange-correlation functional in the form of on-site Hubbard U or exact Hartree-Fock exchange.

5.2 Computational setup

We carried out the electronic structure calculations using the plane waves pseudopotential approach implemented in the Quantum Espresso (QE) software package [139, 140], employing optimized norm-conserving Vanderbilt (ONCV) pseudopotentials [76, 77] to model the electron-ion interaction. The $3s$ and $3p$ semicore states are explicitly included in the valence set for both Fe and Cu pseudopotential. We employed the Perdew-Burke-Ernzerhof (PBE) [67] exchange-correlation functional with the Hubbard U corrections (PBE+U) [82, 83] and the hybrid PBE0 [91] and Heyd-Scuseria-Ernzerhof (HSE) [141]. We applied an energy cutoff for the plane waves of 80 Ry (1088 eV) and a $6 \times 6 \times 6$ Γ-centered **k**-point sampling of the BZ to converge the total energy per atom within 0.5 mRy (7 meV). We performed the hybrid functionals calculations using a variable fraction α of exact exchange, which has been computed on a $2\times2\times2$ **q**-subgrid. For HSE calculations we adopted the recommended screening parameter $\omega = 0.11\ (\text{a. u.})^{-1}$ [95]. We computed the maximally localized Wannier functions (MLWF) adopted to investigate the origin of the crystal field splitting using the `wannier90` code [142], interfaced with the QE software package.

The delafossite structure of CFO, consisting in alternating dumbbell coordinated Cu and octahedral FeO_6 layers (Figure 5.1(a)), was modeled using the rhombohedral primitive cell depicted in Figure 5.1(b), which belongs to the space group $R\bar{3}m$. This is the structure adopted by CFO at room temperature, while below 16 K this material exhibits structural and magnetic phase transitions, which include a monoclinic unit cell with the $C2/m$ symmetry [143–145].

We considered different antiferromagnetic (AFM) arrangements of the spins around each Fe atom, duplicating the cell in each direction to obtain an even number of Fe atoms per cell. We account for three kinds of magnetization: a simple ferromagnet (FM), a layered antiferromagnet (AFML), in which each layer of Fe ions is uniformly magnetized but consecutive layers have opposite magnetization, as in Fe_2O_3, and an antiferromagnet in which the antiferromagnetism lies inside each layer, which is formed by lines of atoms with opposite magnetization (AFMI). The three different crystal structures are represented in Figure 5.2.

The comparison of the total energies per atom at the PBE and the PBE+U level is reported in Table 5.1, in which the energy of the FM structure has been set to zero. The antferromagnetic structures have a lower energy per atom than the ferromagnetic both in PBE and in PBE+U. At the PBE+U level, the energy differences are of the

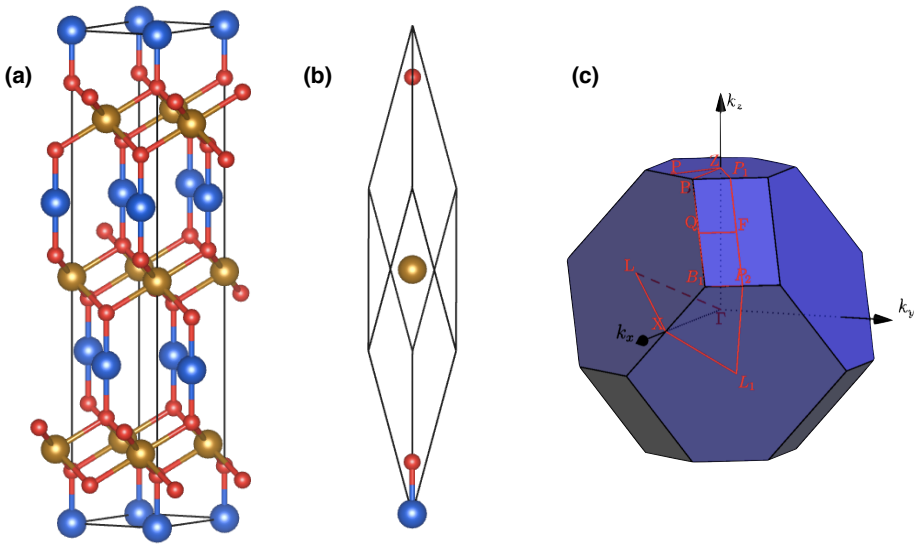

Figure 5.1

Delafossite crystal structure of $CuFeO_2$ (a) and rhombohedral unit cell (b). Cu, Fe and O atoms are represented by blue, yellow and red spheres, respectively. Brillouin Zone of the rhombohedral unit cell (c).

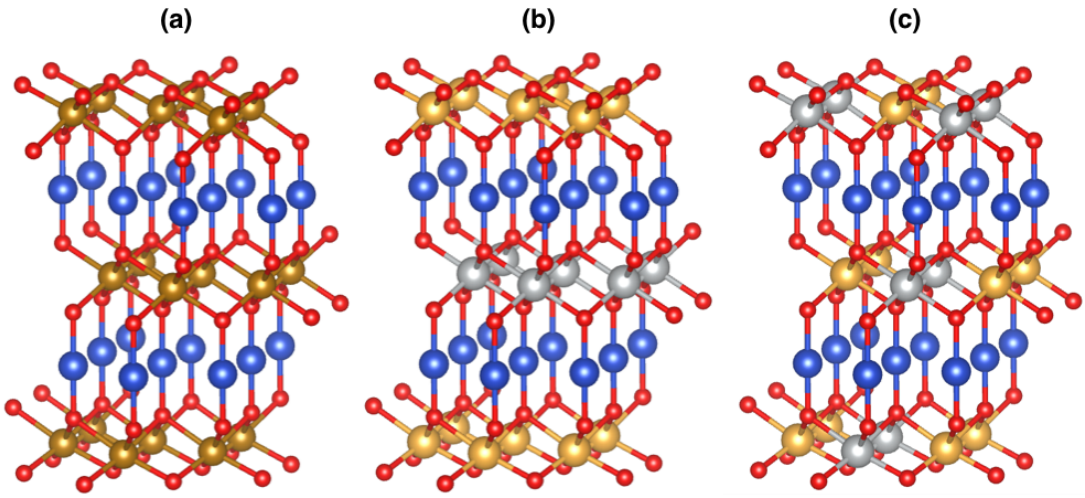

Figure 5.2

Magnetic structures of CFO: ferromagnet (a), layered antiferromagnet (c), antiferromagnet inside each layer (c). Gold and silver spheres represent Fe atoms with up and down spin polarization, respectively. Cu atoms are represented in blue and oxygen atoms in red.

Structure	Energy per atom PBE (eV/atom)	Energy per atom PBE+U (eV/atom)
AFML	-0.003	-0.002
AFMI	-0.025	-0.008

Table 5.1

Comparison between the total energies per atom of the antiferromagnetic configurations at the PBE and the PBE+U level. The values are referred to the energy per atom of the FM configuration, which has been set to zero.

same order of magnitude of the accuracy of our calculation (0.007 eV) and there are no appreciable effects in the electronic properties. For this reason, we adopted a collinear, ferromagnetic arrangement of the spins around the Fe ion using the ferromagnetic cell containg a single formula unit.

5.3 Electronic Structure with the PBE functional

The relaxed geometry of CFO computed with the PBE functional is in good agreement with the available experimental data, based on neutron diffraction measurements [146]. The experimental lattice constants a and c in the hexagonal unit cell, 3.03 Å and 17.09 Å, are slightly overestimated by the PBE functional, which has an equilibrium geometry with $a = 3.03$ Å (+0.6%) and $c = 17.36$ Å (+1.6%).

However, as it is commonly the case for transition metal oxides [81], the PBE functional fails in describing the semiconducting character of CFO. Within this scheme, CFO is wrongly predicted to be a metal, as shown in the bands structure and in the spin-polarized projected density of states (PDOS) in Figure 5.3, where the Fermi level cuts the tails of the majority and minority-spin manifolds. The metallic behaviour is due to a minority spin band with a Fe character crossing the Fermi level around the L point of the BZ.

In spite of this failure, the PBE functional does correctly predict the character of the lowest unoccupied states. The first two groups of unoccupied states have a strong Fe d character, while the third group, 3.5 eV above the Fermi level, is dominated by Cu contributions from the $3d_{z^2}$ and $4s$ states, revealing that the $3d$ shell of Cu is not completely filled ($3d^{10-x}$). This observation is consistent with the measured Cu $L_{2,3}$-

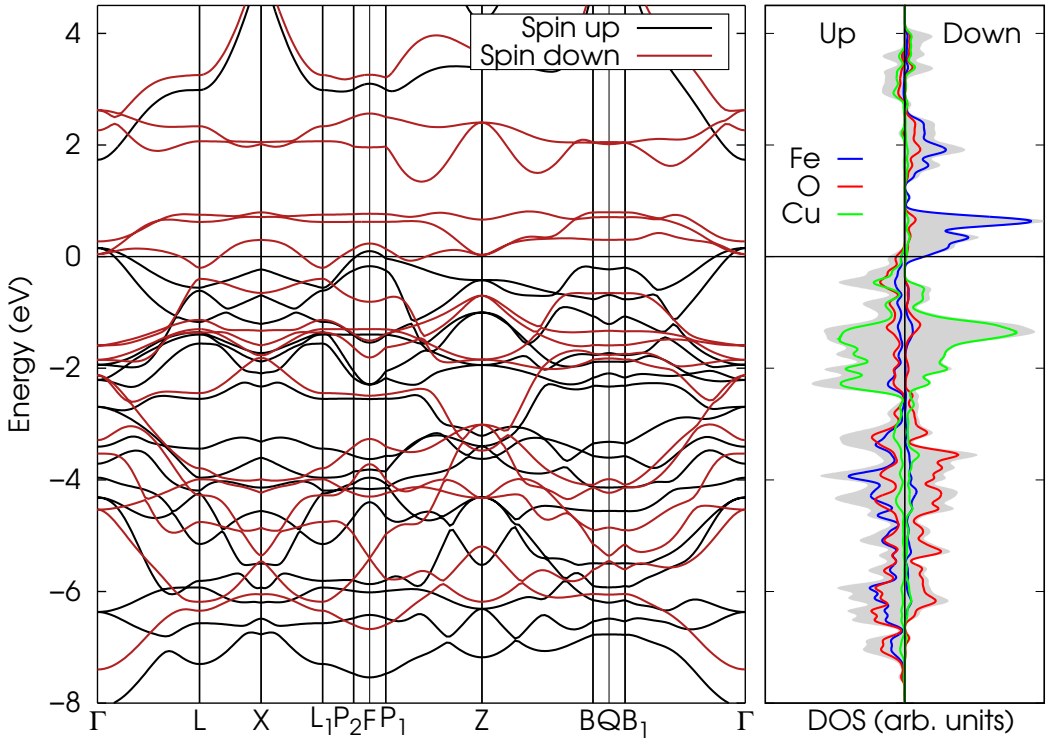

Figure 5.3

Bands structure (left panel) and spin-polarized projected density of states (right panel) of $CuFeO_2$, computed with the PBE exchange-correlation functional. The zero of the energy is set to the Fermi energy.

edge XAS spectrum [133], which established the presence of a partial hole on Cu $3d$ states.

At the PBE level, the Fe ion is correctly predicted to be in the Fe^{3+} high spin ($S = \frac{5}{2}$) state. Note that the oxidation state is calculated following the method of Sit et al. [147], where the number of electrons attributed to a certain ion corresponds to the number eigenvalues of the occupation matrix equal or close to 1. The 5 eigenvalues of the Fe $3d$ occupation matrix in CFO are close to 1 for one spin channel, while in the other they are significantly smaller (< 0.4). Given this configuration, 5 electrons are formally assigned to the Fe ion and all of them lie in the majority spin channel. In Fe^{3+} compounds a large exchange energy, ~ 4.1 eV [148], separates the majority from the minority Fe d orbitals, with the latter lying above the Fermi energy.

In addition, the electrostatic field arising from the octahedral set of surrounding oxygen atoms, seen only as six point charges, breaks the symmetry of the five-fold degenerate d orbitals of the central Fe ion, splitting the lowest conduction states into the three-fold degenerate t_{2g} and the two-fold degenerate e_g manifolds [149]. Going beyond the pure electrostatic picture, the e_g orbitals, namely d_{z^2} and $d_{x^2-y^2}$, oriented directly towards the ligands interact with the O p orbitals forming bonding e_g and antibonding e_g^* combinations. The bonding combination has a stronger O character, while the antibonding contains a prevalent Fe component. Conversely, the t_{2g} (d_{xy}, d_{yz} and d_{zx}), which lie in-between two Fe-O bonds, are non-bonding.

According to PBE level PDOS analysis, the t_{2g} and the e_g manifolds are separated by 1.5 eV, in good agreement with the experimental energy difference (1.35 eV) measured in the XAS spectrum and attributed to the Fe 3d - O 2p overlap [133]. As we will show in Sect.5.4, the introduction of a Hubbard term U on Fe 3d electrons has a very significant effect on this splitting. Since CFO operates as a photocathode, a deeper understanding of the character of the conduction band is of critical importance. In the following, we will therefore analyze in details the physical origin of the energetic splitting of the t_{2g}-e_g states.

5.3.1 Crystal-field splitting

The t_{2g}-e_g splitting contains contributions both from the Coulomb repulsion and from the hybridization between the transition metal d states with the ligand p states, as previously stated. Following the procedure outlined in reference [130] and summarized in Sect.4.5, it is possible to distinguish between the two contributions according to the on-site energies of MLWF. [128] derived from varying Bloch states.

We focus only on the minority-spin channel, since it gives rise to the conduction band states whose crystal field splitting can be directly compared with experimental values. The band structure of the minority-spin channel, plotted along the path in the BZ shown in Figure 5.1(c), is reported in Figure 5.4. The different colors of the bands not only denote the main character of the states, but they also indicate the stage at which the states are included in the summation for the construction of the MLWFs:

$$|w_{n,\mathbf{R}}\rangle = \frac{V}{(2\pi)^3}\int_{BZ} d\mathbf{k}\, e^{-i\mathbf{k}\cdot\mathbf{R}} \sum_{m=1}^{N} U_{mn}^{(\mathbf{k})}\, |\psi_{n,\mathbf{k}}\rangle \ . \tag{5.1}$$

We recall here that $|w_{n,\mathbf{R}}\rangle$ denotes the Wannier function characterized by a unit cell vector $\mathbf{R}$ and a band index n, constructed from a set of N Bloch states $|\psi_{n,\mathbf{k}}\rangle$ via a unitary transformation $\mathbf{U}$ that mixes the Bloch states at a specific $\mathbf{k}$-point.

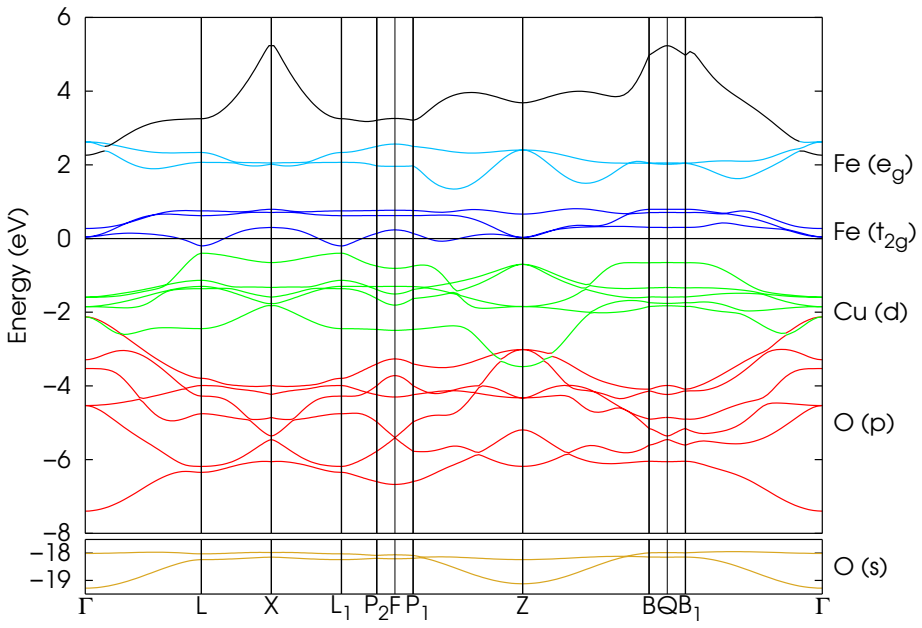

Figure 5.4

Minority spin band structure plotted along the path of the BZ reported in Figure 5.1(c). The different colors represent the main character of the band, according to the PDOS: O s (gold), O p (red), Cu d (green), Fe t_{2g} (dark blue), Fe e_g (light blue), Cu s (black).

In the first instance, we construct the MLWFs including in Eq.(5.1) first the t_{2g} bands (dark blue in Figure 5.4) and then, separately, the e_g bands (light blue). It should be noted that, while the group of t_{2g} states is well separated from the other bands, this is not the case for the e_g set, which cross with Cu states at the Γ-point. In the latter case we adopted the disentanglement procedure introduced by Souza et al. [129] to decouple the bands. The plot of one representative MLWF among the three t_{2g} states and one among the e_g is reported in Figure 5.5(a).

The resulting MLWFs are centered on the Fe atoms and, while those corresponding to the t_{2g} states assume the shape of atomic-like orbitals, the tails of the e_g ones are extended on the surrounding oxygen atoms. The on-site energies for each MLWF are indicated as $\varepsilon^{(d)}$ in the scheme in Figure 5.6. The splitting at this stage between the two-fold degenerate e_g states and the three-fold degenerate t_{2g} amounts to 1.55 eV, in agreement with the difference between the peaks in the PDOS.

In the second step, we construct the set of MLWFs including both Fe d (dark and

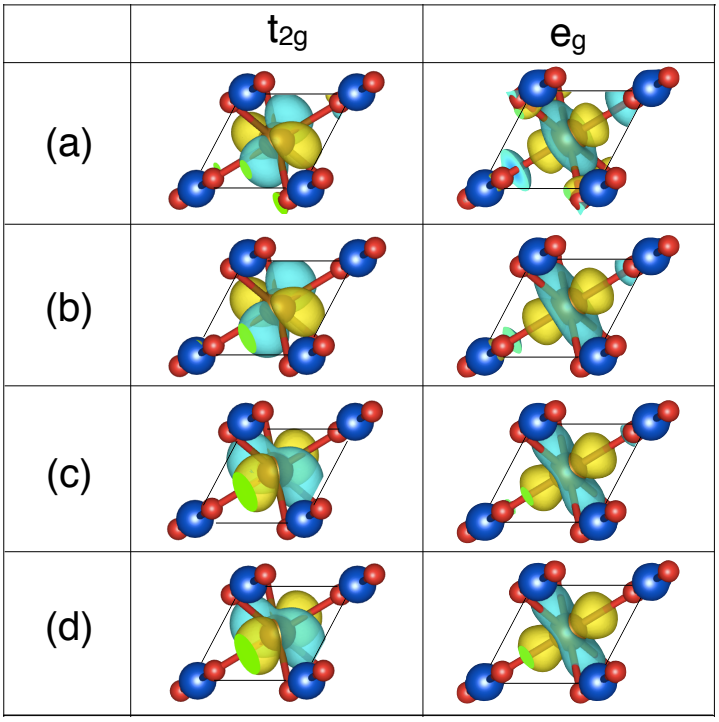

Figure 5.5

Representative MLWFs for the t_{2g} and the e_g set inside the unit cell. In the row (a) the bands with t_{2g} (e_g) character are included separately in the summation. We then add in the summation the Kohn-Sham states with a prevalent O p (b), Cu d (c) and O s (d) character.

light blue in Figure 5.4) and O p (red) states in the summation. We applied again the disentanglement procedure to treat the crossing between the red and the green bands around the Γ and the Z point. The MLWFs centered on the Fe ions are decoupled from those centered on the oxygen atoms and the contribution due to d-p hybridization is removed from the on-site energies. The effect is most notably evident on the e_g MLWFs, whose tail on the surrounding oxygen atoms is significantly reduced, as shown in Figure 5.5(b). The corresponding on-site energy, indicated as $\varepsilon^{(dp)}$, is reduced by 1.00 eV, while for the t_{2g} the difference is only 0.24 eV, indicating the different degrees of hybridization between the Fe d states with the ligands. Moreover, the explicit inclusion of the Kohn-Sham states with O p character in the summation breaks the symmetry of the three-fold degenerate t_{2g} manifold, with one state lying 16 meV higher than the other two.

This effect is due to the rhombohedral arrangement of the oxygen atoms around the central iron, which slightly differs from the octahedral configuration. In a rhombohedral

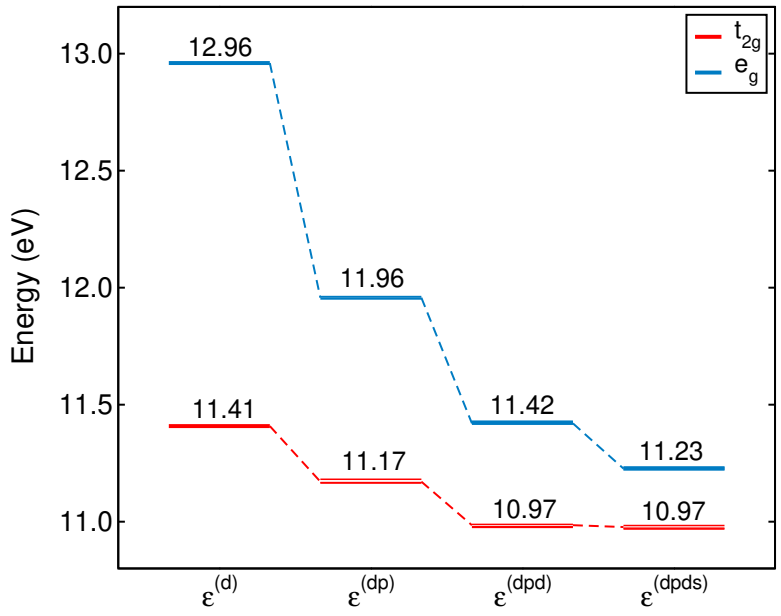

Figure 5.6

On-site energies of the MLWFs corresponding to the t_{2g}-e_g states, obtained including different sets of Kohn-Sham states in the summation in Eq.(5.1).

environment the t_{2g} states are split into two subgroups, one with the a_{1g} representation, which corresponds to the linear combination $|a_{1g}\rangle = \frac{1}{\sqrt{3}}(|xy\rangle + |yz\rangle + |zx\rangle)$ and the other with the two dimensional e_g representation, containing the linear combinations $|e_g^1\rangle = \frac{1}{\sqrt{6}}(2|xy\rangle - |yz\rangle - |zx\rangle)$ and $|e_g^2\rangle = \frac{1}{\sqrt{2}}(|yz\rangle - |zx\rangle)$ [150].

In order to remove possible hybridization effects associated with Cu d states, we include them (green bands in Figure 5.4) in the summation and compute the corresponding on-site energies, $\varepsilon^{(dpd)}$. The on-site energy corresponding to the e_g orbitals is further reduced by 0.55 eV, while only 0.20 eV is removed from the t_{2g} on-site energy obtained at the previous stage. Yet, this comparably small change in energy is accompanied by a change in the shape of the t_{2g} orbitals, which resemble the rhombohedral a_{1g} and e_g orbitals, as shown in Figure 5.5(c).

Finally, we include in the summation the O s states, depicted in gold in Figure 5.4, which lie around 18.5 eV below the Fermi level. The t_{2g} are unaffected by the inclusion of these states while a small contribution of 0.19 eV is removed from the e_g on-site energies, indicating that a small Fe e_g - O s mixture was still present in the MLWFs. The difference between the e_g and the t_{2g} on-site energies obtained at this level, $\varepsilon^{(dpds)}$, amounts to 0.26 eV and can be interpreted as the pure electrostatic contribution to the crystal field splitting [130]. The remaining 1.29 eV instead, can be thought as the consequence of

the hybridization between the d states and the O p, O s and Cu p atomic orbitals. This hybridization effect is more pronounced in the e_g, which experience a larger shift when further states are added to the summation in Eq.(5.1).

5.4 Electronic structure with the PBE+U functional

Although our PBE simulations reproduce some experimental results, in order to recover the semiconducting character of CFO we first explored the effect of adding a Hubbard U correction to the exchange correlation functional, which acts specifically on the d states.

5.4.1 Determination of the self-consistent Hubbard U

The treatment of the strongly correlated Fe ions in CFO by the Hubbard U approach is seriously conflicted within the available literature. Even though the appropriate value of U to apply depends on the set of pseudopotentials and the adopted projection methods, and therefore is not necessarily comparable across different computational approaches, there is a large diversity in the Hubbard U corrections applied to the Fe^{3+} ions in CFO reported in the literature [132, 134, 135, 137]. Values of the effective Hubbard parameter range from 2.2 to 7.1 eV, and in one case the Hubbard term is applied also to Cu^{1+} ions [132]. In this work, the correction is only applied to Fe ions, which are the main source of the metallic behaviour. Furthermore, it has previously been shown that the U correction does not improve the description of the electronic structure of Cu^{1+} compounds, where the d shell is completely filled, for instance in the case of Cu_2O [48].

In order to compute the Hubbard U correction for our computational setup we followed the linear-response formulation of Cococcioni and de Gironcoli [81], adapted to include the self-consistency procedure introduced by Kulik et al. [85]. In addition, we performed an extra geometry self-consistency cycle in order to capture any changes to the U correction associated with the rehybridzation of the orbitals due to changes in the nuclear coordinates.

The evaluation of U by linear response should be computed in the limit of an infinite crystal, thus in our simulations we have measured the response in rhombohedral supercells of increasing size, assuming 50 meV as convergence threshold in the value of U_{scf}. We evaluated both the full response matrices and the scalar on-site response, where full response matrices are constructed from the changes to the occupations of all

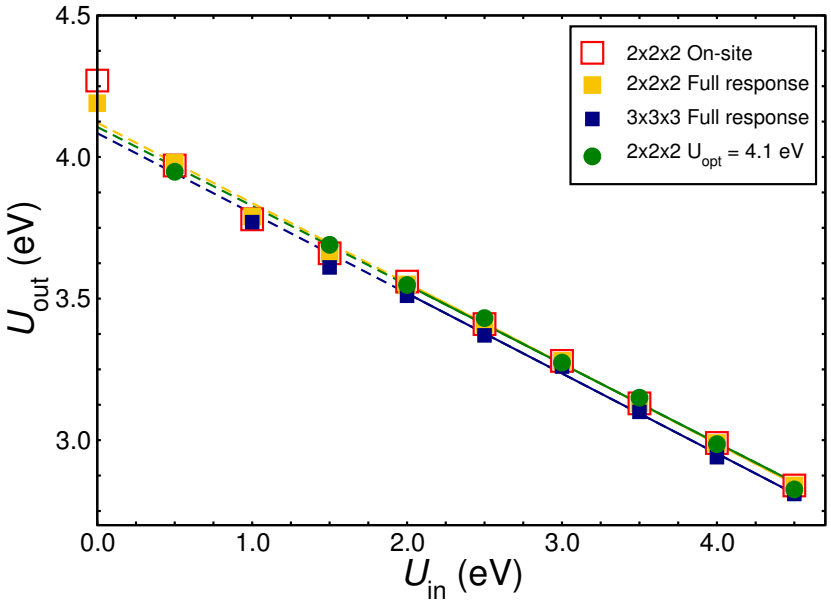

Figure 5.7

A plot summarizing the self-consistent computation of the Hubbard U parameter used throughout this work. Values computed with the full response matrix and onsite only approaches are represented by solid and hollow symbols respectively. Solid and dashed lines represent the fitted and extrapolated regions of the graph. Square symbols denote computations on the PBE-optimized geometry, whereas circles are used for the PBE+U = 4.1 eV-optimized geometry.

of the Fe sites within the supercell, while the on-site response takes into account only the response of the site where the perturbation is applied.

It is not unreasonable to expect that ensuing changes to the bonding, and thus the electron density distribution surrounding the Hubbard atoms, could give rise to a different spurious curvature in the total energy and the initially computed U_{scf} may no longer be applicable. Consequently, in addition, we performed an extra geometry self-consistency cycle in order to capture any changes to the U correction associated with the re-hybridzation of the orbitals due to changes in the nuclear coordinates.

The results of our linear response, geometrically self-consistent procedure are presented in Fig. 5.7, highlighting several subtle features of the approach when applied to CFO.

Firstly, on the convergence of the linear response calculations with respect to increasingly large supercells, we considered up to cells $3 \times 3 \times 3$ in size, finding that a rhombohedral $2 \times 2 \times 2$ supercell (solid yellow squares in Fig. 5.7) is sufficient for the computation of both U_{out} and U_{scf}. This represents a significantly fewer number Hub-

bard sites than for instance required by Cococcioni and de Gironcoli in order to achieve convergence of the U parameter for FeO [81]. Secondly, our results show that calculation of the full response matrix has little bearing on U_{scf} when compared with on-site corrections only. In fact within the linear regime (> 2.0 eV) the on-site and full response calculations are equivalent yielding $\Delta U_{\text{scf}} \approx 10$ meV. Finally, the response computed on the PBE+U optimized geometry, represented by green dots, is equivalent to the one computed on the PBE geometry.

This linear-response procedure reveals U_{scf} to be converged within 50 meV to a value of 4.1 eV. This value is in line with other DFT+U studies of Fe^{3+} based oxides, in which U was not computed via linear response calculations, but it was tuned to 4.2 and 4.0 eV in order to obtain the experimental energy gap [151] and the formation enthalpy [152] of α-Fe_2O_3, respectively. A similar value, $U = 4.3$ eV, has also been evaluated for α-Fe_2O_3 following an *ab-initio* approach based on unrestricted Hartree-Fock theory [153]. The optimized equilibrium lattice constants a and c, in the hexagonal description, are 3.10 Å (+2.3% w.r.t. the experimental value) and 17.32 Å (+1, 3%), respectively, resulting in a very similar geometry compared to the one obtained with the PBE functional.

The PDOS at the PBE+U_{scf} level is reported in Figure 5.8, the computed band gap, which is still lower than experimentally measured value, is 0.80 eV. In addition to underestimating the band gap we find that the CB states are also altered by the Hubbard U: the splitting between the unoccupied Fe t_{2g} and e_g states is not preserved when the U correction is added, and the two manifolds collapse in a single peak in the PDOS. This outcome is in disagreement with the experimental XAS measurements, where the two peaks are easily distinguishable and separated by a gap of 1.35 eV [133]. A similar behaviour in CFO has been reported in the Supporting Information of Ref.[10]. However, this effect is not peculiar to this compound, but it has been shown that it occurs when DFT+U is applied to other Fe^{3+} compounds like hematite [154] and $BiFeO_3$ [155]. Interestingly, Cr^{3+} in CrI_3 displays a similar behaviour [156].

5.4.2 Crystal field splitting

Determining the origin of this result is important in assessing the application of the DFT+U to CFO, since an accurate description of the empty conduction band states is of paramount importance for understanding the ability to act as the photocathode. To explain the origin of this failure, we note that, in a first approximation, neglecting effects due to charge rearrangement, the Kohn-Sham eigenvalues $\epsilon^{\sigma}_{\mathbf{k}v}$ are rigidly shifted by the

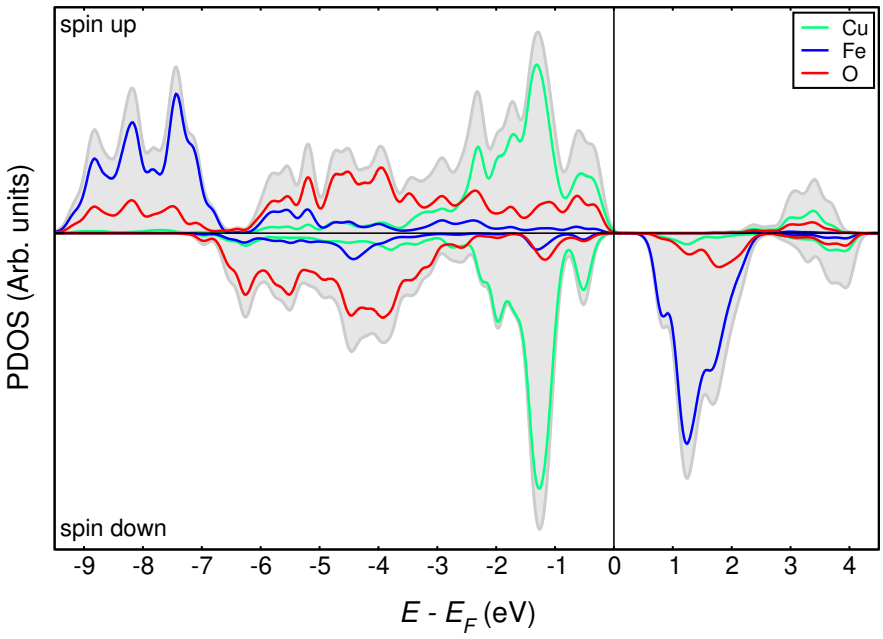

Figure 5.8

Projected density of states at the PBE+U level, using the self-consistent value of U.

Hubbard U according to Eq.(4.41), which we report below for the sake of simplicity:

$$\epsilon_{\mathbf{k}v}^{\sigma\,\mathrm{DFT}+U} = \epsilon_{\mathbf{k}v}^{\sigma\,\mathrm{DFT}} + U \sum_{I,m} \left(\frac{1}{2} - n_m^{I,\sigma} \right) | \langle \phi_m^I | \psi_{\mathbf{k}v}^{\sigma} \rangle |^2 \,. \tag{5.2}$$

The value of the shift depends on the occupation numbers $n_{m,\sigma}^I$ of the corresponding d orbitals and on the projection of the Kohn-Sham states onto the atomic Fe d orbitals. The occupation numbers $n_{m,\sigma}^I$ in the minority-spin channel of the d states of Fe obtained with the PBE functional are reported in the first row of Table 5.2.

On the basis of the Fe^{3+} oxidation state and the high-spin character, it could be naively expected that the occupation numbers $n_{m,\sigma}^I$ would be zero. However, the occupation numbers can assume values greater than 0 due to hybridization and projection effects. It has been shown that when a transition metal and a ligand form a covalent bond, if only the bonding state is occupied, a projection procedure onto the d orbitals could give rise to occupation numbers greater than 0, whose origin resides only in the orbital mixing [147]. As already pointed out, the d_{z^2} and $d_{x^2-y^2}$ orbitals hybridize with the p orbitals of the ligands, forming σ bonding and antibonding combinations and the projection of the occupied bonding Kohn-Sham states with a prevalent O character, but a smaller Fe contribution, onto the atomic d_{z^2} and $d_{x^2-y^2}$ orbitals gives rise to non-zero occupation numbers. The atomic d_{xy}, d_{zx} and d_{zy} orbitals are not formally hybridized

	d_{xy}	d_{zx}	d_{zy}	d_{z^2}	$d_{x^2-y^2}$	$\Delta\epsilon_{n\mathbf{k}}^{U_{scf}}$ (eV)
$n^{\downarrow}_{I,m}$	**0.197**	**0.199**	**0.202**	**0.376**	**0.376**	
$\lvert\langle\phi^I_m\lvert\psi^{\downarrow}_{\Gamma\, t^1_{2g}}\rangle\rvert^2$	0.279	0.522	0.003	0.002	0.181	+**1.08**
$\lvert\langle\phi^I_m\lvert\psi^{\downarrow}_{\Gamma\, t^2_{2g}}\rangle\rvert^2$	0.300	0.103	0.505	0.078	0.000	+**1.16**
$\lvert\langle\phi^I_m\lvert\psi^{\downarrow}_{\Gamma\, t^3_{2g}}\rangle\rvert^2$	0.266	0.213	0.325	0.008	0.004	+**1.00**
$\lvert\langle\phi^I_m\lvert\psi^{\downarrow}_{\Gamma\, e^1_g}\rangle\rvert^2$	0.035	0.047	0.008	0.003	0.501	+**0.37**
$\lvert\langle\phi^I_m\lvert\psi^{\downarrow}_{\Gamma\, e^2_g}\rangle\rvert^2$	0.003	0.001	0.032	0.555	0.005	+**0.33**

Table 5.2

Occupation numbers of the minority-spin Fe d orbitals in CFO at the PBE level and projection of the t_{2g} and e_g states at the Γ point onto the atomic orbitals. The last column represents the shift produced by $U = 4.1$ eV on these states computed using Eq.(5.2).

with the oxygen orbitals in a pure tight-binding picture. However, the tail of the atomic projectors can give rise to spurious interactions that could enhance the value of the occupation number. The results of DFT+U calculations depend considerably on the choice of the local projector. The atomic orbitals used in atomic-like projectors have in general a large effective radius and therefore a larger number of electrons can be accommodated in the d shell [157]. We have shown with the MLWFs analysis that a small hybridization contribution, 0.44 eV, is present in the on-site energies of the t_{2g} states, much smaller than the one in e_g states, 1.73 eV. This different hybridization is reflected in the occupations of the d_{z^2} and $d_{x^2-y^2}$, which are larger than those of the other three d orbitals and, consequently, the corresponding factor $(\frac{1}{2} - n^{I,\sigma}_m)$ in Eq.(5.2) will be smaller.

Moreover, we report in the lower part of Table 5.2 the projection of the t_{2g} and e_g Kohn-Sham states at the Γ point onto the five d orbitals. The sum of the projections of the t_{2g} states is close to the unity, while it is around 0.6 for the e_g, indicating that there is a larger Fe character in the former, as evident also from the PDOS in Figure 5.3. The correction on the eigenvalues at the Γ point, computed using Eq.(5.2) with the self-consistent value of $U = 4.1$ eV, is reported on the last column of Table 5.2. The combination between the different occupation numbers and atomic projections makes the shifts on the t_{2g} states three times bigger than those applied to the e_g with the effect of pushing the former towards the latter and closing the gap between the two manifolds.

The shifts reported in Table 5.2 are computed using Eq.(5.2), in which the PBE

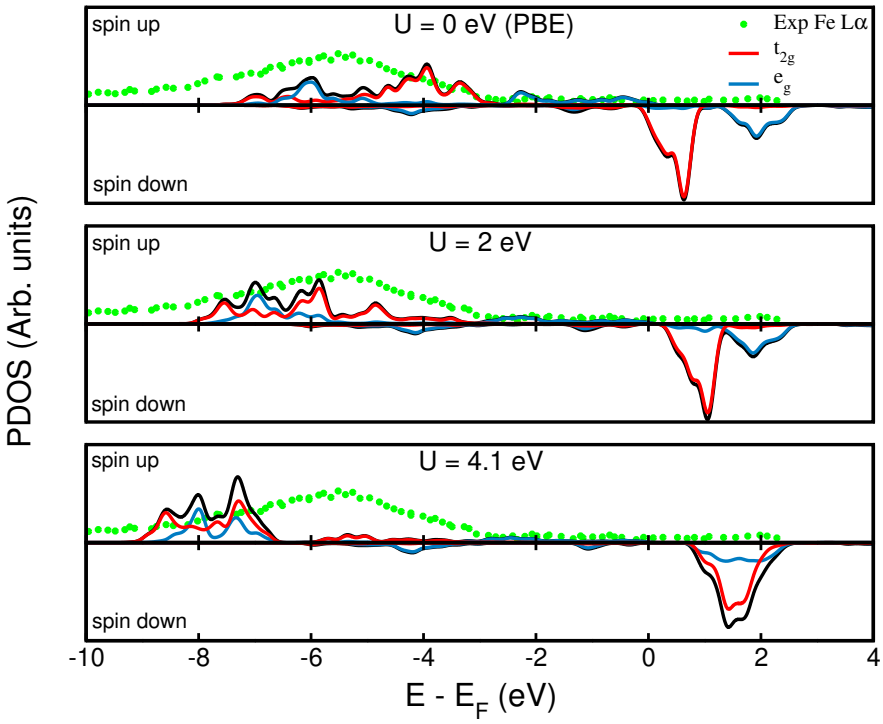

Figure 5.9

Projected density of states onto the Fe t_{2g} (red line) and e_g (green line) d states for different values of the applied Hubbard U. The green dots represent the experimental data of Fe $L\alpha$ edge x-ray emission spectrum, taken from Ref.[132].

wavefunctions are assumed to be fixed and the potential due to the Hubbard U is applied in a perturbative way. These results are consistent with the eigenvalues reported at the first iteration of the self-consistent cycle, when U is switched on. However, the wavefunctions are continuously updated during the self-consistent cycle, causing modifications also in the Kohn-Sham potential, and the difference between the corrections applied to the t_{2g} and the e_g states at the end of the cycle is even bigger than the prediction made with Eq.(5.2), with the consequence of further reducing the gap.

In Figure 5.9, we compare the PDOS on the Fe atomic orbitals for three different values of U with the experimental Fe $L\alpha$ x-ray emission spectrum. The occupied majority-spin states shift rigidly with U towards lower energies as expected by the fact that their occupation number is close to 1. A comparison with the experimental data reveals that the position of the occupied Fe d state is well reproduced for small values of the Hubbard U, while they are pushed towards lower energies when the self-consistent value is employed. The unoccupied minority-spin t_{2g} states are shifted linearly with U

towards the e_g states, which are almost unaltered. The two manifolds start overlapping for $U = 2$ eV and they collapse into a single peak when the self-consistent value of U (4.1 eV) is applied.

As pointed out above, the magnitude of the shift experienced by the t_{2g} and e_g states when U is applied depends on the different degrees of hybridization that those states have with the orbitals of the surrounding atoms. In order to investigate the effect of U on the hybridization of Fe d with the other orbitals, we analyzed MLWFs constructed from different DFT+U wavefunctions and eigenvalues. More explicitly, for each value of U considered, we built MLWFs including in the first instance only the t_{2g} and e_g states, and then including the O p, Cu d and O s states within the summation (see Eq. (5.1)). We noted in Sect.5.3, the difference between the on-site energies of the MLWFs $\epsilon^{(d)} - \epsilon^{(dpds)}$ can be interpreted as a working definition of hybridization effects on a particular orbital.

We plot schematically of the on-site energies of the MLWFs for three different values of U in Figure 5.10. The on-site energy, $\epsilon^{(d)}$, of the MLWFs relative to the t_{2g} states gets closer to the e_g state as U increases, reflecting the collapse of the two manifolds in the PDOS in Figure 5.9.

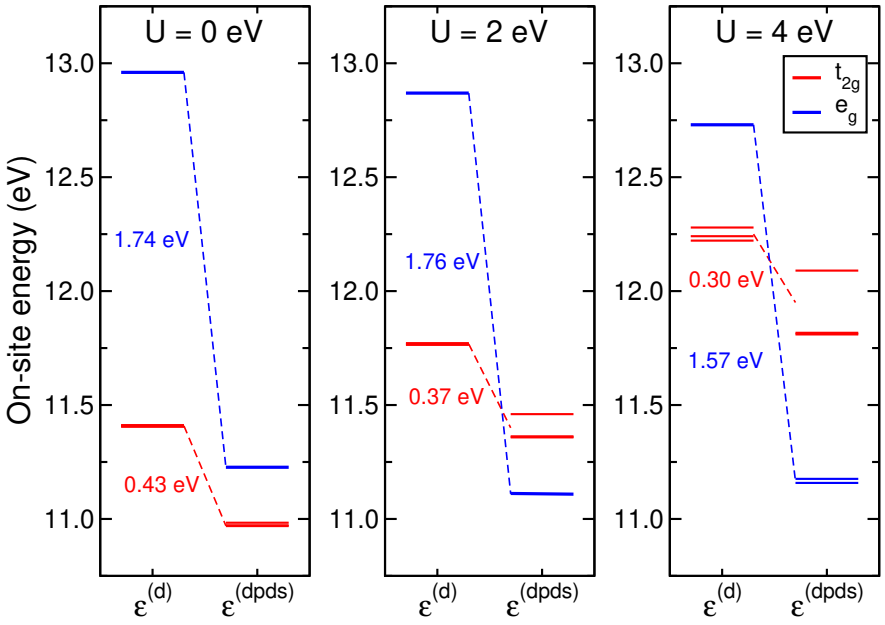

Figure 5.10

On-site energies of the MLWFs corresponding to the t_{2g} and e_g states for three different values of the Hubbard U.

The spurious effect that the introduction of the Hubbard correction has on the two manifolds becomes clear once we decompose the crystal field splitting in electrostatic and hybridization effects. The difference between the onsite energies $\epsilon^{(d)}$ and $\epsilon^{(dpds)}$ of the MLWF corresponding to the e_g states changes from 1.74 eV for $U = 0$ eV to 1.57 eV for $U = 4$ eV, indicating that the impact of U in reducing the hybridization is fairly small, -0.2 eV. Similarly, for the t_{2g} states the change in hybridization due to U modifies the difference between $\epsilon^{(d)}$ and $\epsilon^{(dpds)}$ from 0.43 eV to 0.30 eV.

When we set $U = 2$ eV, the on-site energy $\epsilon^{(dpds)}$ of the e_g states becomes smaller than the one of the t_{2g} and this effect is further amplified for $U = 4$ eV, in which the e_g states lie 0.8 eV lower than the t_{2g}. The reverse ordering of these states would correspond to an unphysical negative electrostatic crystal field splitting, in contrast with the pure electrostatic picture [149]. This inversion suggests that the interpretation of the difference between the on-site energies as a measure of electrostatic effects is only valid as long as the states are not altered by the introduction of the U correction.

The incorrect description of the t_{2g} and e_g states at the DFT+U level affects the on-site energies $\epsilon^{(d)}$ of the MWLFs. These bad starting energies lead to the spurious negative electrostatic crystal field splitting when hybridization effects, that are weakly dependent on U, are gradually removed passing from $\epsilon^{(d)}$ to $\epsilon^{(dpds)}$.

Another spurious effect that arises due to the presence of the Hubbard correction relates to the splitting of the t_{2g} states into the a_{1g} and e_g subgroups due to the rhombohedral arrangement of atoms. This separation is emphasized with increasing values of U, for example it is most strongly amplified in the case of $U = 4$ eV, where it is equal to 0.25 eV.

It is worthwhile to note that potential solutions to these issue have already been proposed, based either on a separate treatment of the t_{2g} and e_g electrons in DFT+U [158], or using a suborbital dependent U [159]. Alternatively, the application of an intra-site correction V [160] could favor the decoupling of the e_g states from the O p orbitals, favoring the shift applied by U.

5.5 Electronic structure with hybrid and meta-GGA functionals.

An alternative approach to address the shortcomings of the PBE functional in reproducing the semiconducting character of CFO is to include a fraction of exact Hartree-Fock exchange within the exchange-correlation functional. To this end, we employ the hybrid

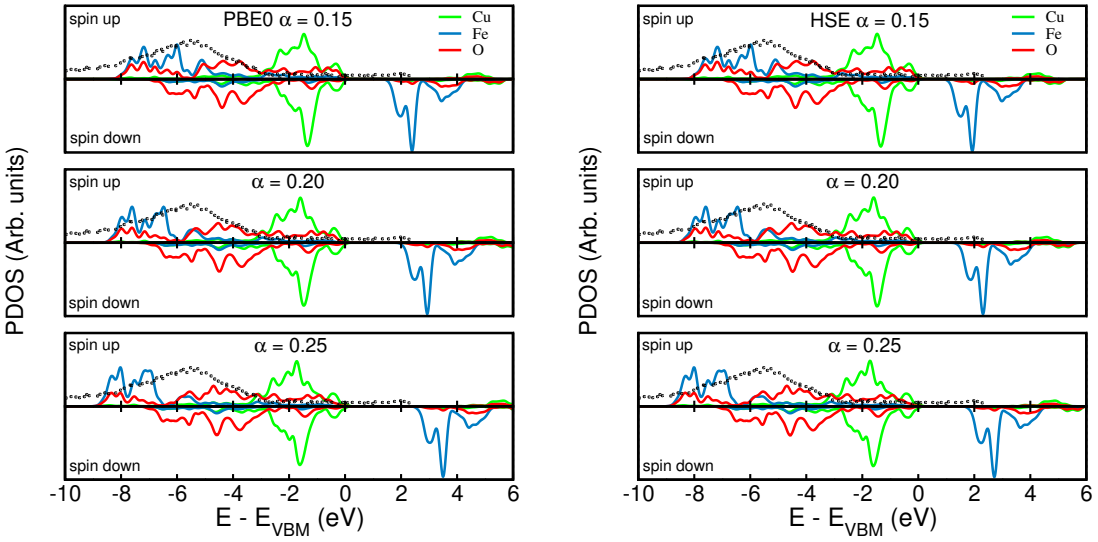

(a) (b)

Figure 5.11

Projected density of states for different values of the fraction of exact exchange, using the PBE0 (a) and the HSE hybrid functionals. The blue dashed line represents the experimental data of Fe $L\alpha$ edge x-ray emission spectrum, taken from Ref.[132].

functionals PBE0 and HSE, on top of the PBE and PBE+U optimized geometry, tuning the fraction α of the exact exchange to reproduce several experimental quantites related to the electronic structure of CFO, in particular the bandgap, the crystal field splitting of the unoccupied Fe 3d states and the position of the Fe 3d states in the occupied states. The choice of the starting geometry does not affect the electronic structure significantly and in the following we report only the electronic structures obtained on top of the PBE+U geometry.

The PDOS for three selected values of the fraction α is reported in Figure 5.11. The two functionals provide an equivalent description of the occupied states when the same fraction of exact exchange is applied. A small fraction of exact exchange, around 0.15, is required to describe correctly the position of the occupied Fe d states, compared with the experimental $L\alpha$ edge emission spectrum, as indicated by the dashed lines in Figure 5.11. The Fe manifold shifts linearly towards lower energies for increasing α, while the Cu and the O manifolds are only slightly affected and their position is almost constant.

The linear shift is applied also to the empty states which move rigidly towards higher energies for increasing α. The t_{2g} and e_g manifolds are well separated for all values of α

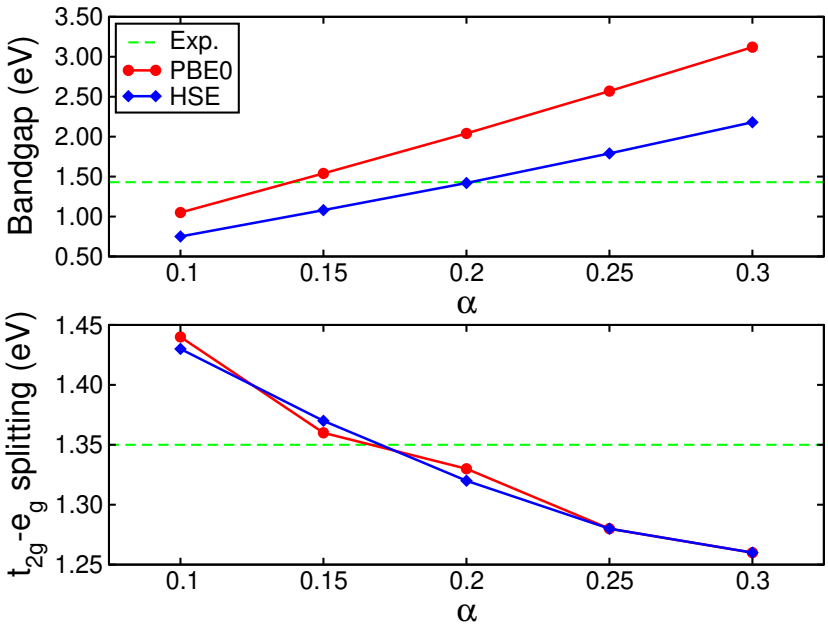

Figure 5.12

Bandgap (upper panel) and crystal field splitting (lower panel) in CFO, computed with hybrid functionals using a variable fraction of exact exchange.

and the crystal field splitting, computed via a weighted average on the PDOS, is plotted in the lower panel of Figure 5.12. In the range of α considered, the crystal field splitting lies within ± 0.1 eV of the experimental value, without any indication of the collapse towards a single peak observed at the PBE+U_{scf} level of theory.

In the upper panel of Figure 5.12 we report the value of the bandgap, comparing it with the optical bandgap of 1.43 eV [10]. It should be noted that this comparison is not formally justified, since the optical bandgap is renormalized by excitonic effects. Yet, in the absence of an experimental value for the true quasi-particle gap, the optical gap can serve as a rough benchmark. The PBE0 functional predicts a higher bandgap than the HSE at the same α, an effect that has been previously observed for Cu_2O [48]. When the standard fraction of exact exchange, 0.25, is employed the bandgap is overestimated by both functionals indicating that a lower fraction is required to reproduce the optical value. Specifically, HSE requires a fraction of 0.20 to reproduce the experimental optical gap, while a value of $\alpha = 0.14$ is obtained by interpolating the PBE0 data. In both cases, the crystal field splitting lies within 0.03 eV from the experimental value, while the occupied Fe d states are better reproduced with a low fraction of exact exchange and so, in this sense, the PBE0 functional may be preferable.

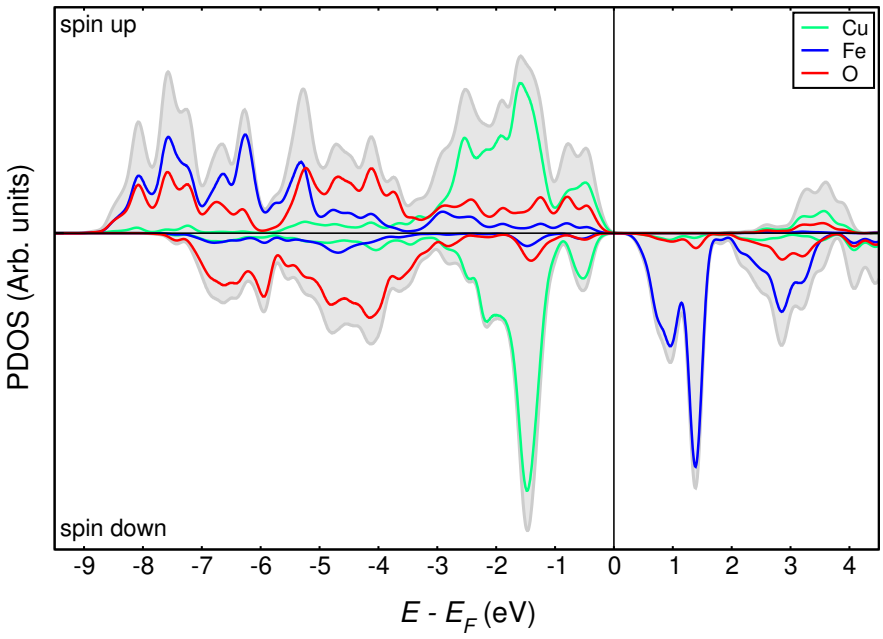

Figure 5.13

Projected density of states computed using the meta-GGA SCAN functional.

There are solid theoretical foundations for which an optimal value for α is given by the reciprocal of the static dielectric constant $\alpha = 1/\epsilon_\infty$ [98, 100]. We computed $\epsilon_\infty = \frac{1}{3}\,\mathrm{Tr}[\epsilon]$, where ϵ is the dielectric tensor, computed at the PBE+U level within Density Functional Perturbation Theory [161], and we obtained $\alpha = 0.11$. Therefore, it is not surprising that the fraction of exact exchange that provides a bandgap in excellent agreement with the experiments is $\alpha = 0.14$, very close to the estimate obtained from $\alpha = 1/\epsilon_\infty$.

Finally, we investigated the structural and electronic properties of CFO using the meta-GGA functional SCAN [162], which was recently shown to provide accurate results for geometries and energies of a vast class of materials [163]. The SCAN lattice constant $a = 3.02$ Å and $c = 17.24$ Å are closer to their experimental counterparts than those computed at the PBE and the PBE+U level, with an error of -1% for a and $+0.88\%$ for c. The PDOS computed at the equilibrium geometry is reported in Figure 5.13. While the crystal field splitting is captured correctly, we obtained a band gap of 0.56 eV. This is a clear improvement over the metallic PBE solution, but is still significantly smaller than the 1.43 eV experimental gap.

5.6 Summary

Our calculation confirms that, without any corrections, PBE wrongly predicts a metallic bulk CFO whereas the peak of the occupied d states and the crystal field splitting between the lowest conduction bands with the Fe d character are correctly described. In particular, we analyzed the origin of the crystal field splitting and we separated the dominant hybridization contribution from the pure electrostatic, computing the on-site energies of different sets of MLWFs.

We derived a self-consistent value of the Hubbard U parameter from series of linear response calculations, in order to give a penalty to delocalized Fe d states, favoring the opening of a gap in the band structure. However, the PBE+U formalism fails in describing the character of the lowest unoccupied states, predicting a collapsing of the Fe $3d$ t_{2g}-e_g manifolds, due to projection effects and hybridization with the ligands.

A hybrid functional with a fraction of exact exchange equal to the inverse of the dielectric constant is necessary for a correct description of the electronic structure. In the following chapters, we will use this last value as the most suitable theoretical approach to describe the electronic structure of CFO, as required in the band edge alignment procedure.

6

Thermodynamic stability and native point defects of bulk $CuFeO_2$

CONTENTS

The synthesis of pure CFO is challenging because the Cu-Fe-O system exhibits different phases depending on the environmental conditions and the Cu:Fe ratio [164]. Moreover, it is necessary to avoid the formation of different compounds, such as α-Fe_2O_3 [58] and Cu^{2+} compounds [60, 165] during the growth.

We investigated the conditions at which CFO is thermodynamically stable combining the DFT+U approach with the *ab-initio* thermodynamics formalism [1], following previous works on Li-based ternary compounds [166–168]. We focused in particular on determining accurate formation free energies in order to construct realistic phase diagrams both in air and in an aqueous environment.

In this chapter we report the outcomes on this thermodynamic investigation, focusing in particular on the range of the chemical potentials which define the stability region of CFO. Once the conditions for which CFO is stable are established, we investigated which are the defects that could appear more easily during the synthesis processes.

6.1 Computational setup

We performed the calculations with the Quantum Espresso (QE) code, using ONCV pseudopotentials and a kinetic energy cutoff of 80 Ry, as described in the previous chapter. We employed the DFT+U approach for CFO and the binary Fe oxides used to construct the phase diagrams, using the self-consistent value of $U = 4.1$ eV previously computed. The total energies of the Cu- and Fe-based compounds were computed for their theoretical relaxed geometry. The formation energies of defects in CFO were studied in a $4 \times 4 \times 1$ hexagonal supercell containing 192 atoms.

6.2 Thermodynamic stability of bulk $CuFeO_2$ in air

To evaluate the limits of the thermodynamic stability of bulk CFO at zero temperature, we computed the formation enthalpies of binary and ternary Cu-Fe-O compounds from the elementary constituents, according to Eq.(4.51). Although the equation holds for the Gibbs free energies, the transition to enthalpies is immediate and consists in ignoring the entropic contribution. We neglected the volumetric and zero-point effects which are commonly small in solid phases [101], approximating the enthalpies of the product and the reactants as their DFT total energies per formula unit:

$$\Delta H^f \simeq E_p - \sum_r n_r E_r \,. \tag{6.1}$$

In the formation of metal oxides, oxygen is present in the reactants and the oxygen molecule is taken as a reference state. However, it is well-known that the overbinding of the O_2 molecule within the LDA and GGA scheme produces wrong formation energies, especially in transition metal oxides in which the self-interaction error introduces further issues, due to the different number of localized d electrons in the reactants and in the product [152].

6.2.1 Mixed GGA/GGA+U approach

What is commonly done to overcome the problem of the overbinded O_2 molecule consists in adding by hand a correction in the DFT total energy of the molecule, in such a way that the experimental binding energy is recovered. However, we follow herein the method of Wang et al. [152], which consists in correcting the total energy of the O_2 molecule

to minimize the mean absolute error in the formation energy of non-transition metal oxides. We wrote several oxidation reactions per O_2 molecule involving metal oxides which do not have the localized $3d$ orbitals typical of the transition metal oxides:

$$\frac{4}{3}\mathrm{Al} + \mathrm{O_2} \rightarrow \frac{2}{3}\mathrm{Al_2O_3}\,, \tag{6.2}$$

$$2\mathrm{Ca} + \mathrm{O_2} \rightarrow 2\mathrm{CaO}\,, \tag{6.3}$$

$$2\mathrm{Mg} + \mathrm{O_2} \rightarrow 2\mathrm{MgO}\,, \tag{6.4}$$

$$4\mathrm{Li} + \mathrm{O_2} \rightarrow 2\mathrm{Li_2O}\,, \tag{6.5}$$

$$4\mathrm{Na} + \mathrm{O_2} \rightarrow 2\mathrm{Na_2O}\,, \tag{6.6}$$

$$\mathrm{Si} + \mathrm{O_2} \rightarrow \mathrm{SiO_2}\,. \tag{6.7}$$

We computed the formation enthalpies of these compounds, taking the PBE O_2 molecule as a reference and we fit the values against the experimental data reported in the NIST-JANAF database [104], as shown in Figure 6.1(a). We fit the data with a straight line with a unitary slope, whose intercept, 1.47 eV, represents the average error in determining the formation enthalpies when the PBE O_2 molecule is employed. This error is entirely attributed to the oxygen molecule, whose total energy is then corrected by 1.47 eV. Our fitted value is slightly larger (0.11 eV) compared to the one computed in Ref.[152], because we considered the formation enthalpies at 298 K and not those at 0 K and the contribution of these thermal effects has been estimated to be 0.1 eV [152].

Once a reliable energy for the O_2 molecule ($E^{fit}_{O_2}$) has been obtained, we computed the formation enthalpies of Fe-based oxides using the mixed GGA/GGA+U method [169]. The basic idea behind this approach is that GGA provides a good description of the compounds with delocalized states, such as metals or alloys, while the oxides, containing localized states, are better represented in a GGA+U scheme. Most of the error in reaction energies occurs when electronic states on transition metals change their localization character. The formation enthalpies of the Fe-based oxides can be computed using the GGA energy of the metallic reactants and the GGA+U energy of the oxide, provided that the latter is properly corrected by applying an energy adjustment proportional to the transition metal content.

Following the method of Jain et al. [169], we have calculated the correction to be applied to the GGA+U energies computing the formation enthalpies of binary Fe oxides (Fe_2O_3, Fe_3O_4 and FeO) as:

$$\Delta H^{f}_{Fe_xO_y} = E^{GGA+U}_{Fe_xO_y} - xE^{GGA}_{Fe} - \frac{y}{2}E^{fit}_{O_2}\,, \tag{6.8}$$

where $E^{GGA+U}_{Fe_xO_y}$ is the uncorrected GGA+U energy of the oxide. The difference between

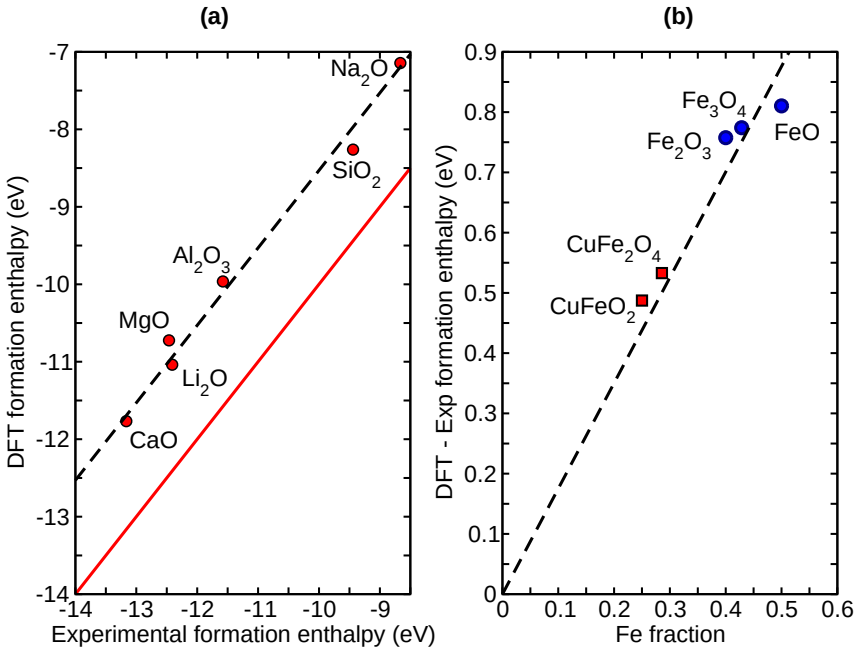

Figure 6.1

Formation energies of non-transition metal oxide per O_2 in the reaction (a). The dashed line represent the line with unitary slope that best interpolates the points, while the red line represents the ideal line of the experimental data. (b) Difference between the DFT and the experimental formation energy for Fe binary and ternary oxides. The fit has been performed only using the binary oxides data, the Cu-Fe oxides are also shown, suggesting that the correction generalizes also for ternary compounds.

the formation enthalpies per atom computed as in Eq.(6.8) and the experimental values, normalized per atom within the unit cell, is plotted as a function of the Fe fraction in the compound, as shown in Figure 6.1. The discrepancy from the experimental values increases linearly with the Fe content in the oxides. This is further confirmed by the fact that the values for Cu-based ternary oxides, which are not included in the fit, lie roughly on the same line.

The slope of the line passing through the origin that gives rise to the best fit of the points represents the magnitude Δ^{corr} of the correction to be applied to the total energies of the oxides for each Fe atom in the unit cell. We found a slope of 1.75 eV/Fe and therefore we corrected each binary and ternary Fe oxide with 1.75 eV for each Fe atom in the unit cell. This value is in good agreement with the correction found by Jain et al. for Fe oxides, 1.723 eV.

Compound	U=3.5 eV	U = 4.1 eV	U = 4.5 eV	EXP
$CuFeO_2$	-1.29	-1.28	-1.27	-1.33 [170]
$CuFe_2O_4$	-1.39	-1.40	-1.39	-1.43 [170]
Fe_2O_3	-1.68	-1.65	-1.64	-1.71 [171]
Fe_3O_4	-1.65	-1.66	-1.63	-1.66 [171]
FeO	-1.44	-1.56	-1.50	-1.41 [171]

Table 6.1

Formation enthalpies (eV per atom) of binary and ternary Fe-based compounds, computed with the mixed GGA/GGA+U method for three different values of U.

The results shown in Figure 6.1 have been obtained using the value of U determined in the previous chapter, computed with the linear response approach [81]. We report in Table 6.1 the formation enthalpies obtained with different values of U, to show how they barely depend on U when the mixed GGA/GGA+U method is adopted, since the correction is fitted on the experimental data.

The total energies of the GGA+U calculations have been adjusted subtracting a correction $\Delta^{corr} = 1.75$ eV for each Fe atom in the unit cell to make the GGA+U energies compatible with the reference GGA values. The formation enthalpy of a compound containing N_i atoms of the i-th species is computed subtracting the total energies of the constituent elements from the adjusted GGA+U total energy of the oxide ($E^{GGA+U}_{N_{Cu}N_{Fe}N_O} - N_{Fe}\Delta^{corr}$):

$$\Delta H^f_{N_{Cu}N_{Fe}N_O} = (E^{GGA+U}_{N_{Cu}N_{Fe}N_O} - N_{Fe}\Delta^{corr}) - N_{Cu}E^{GGA}_{Cu} - N_{Fe}E^{GGA}_{Fe} - N_O\frac{1}{2}E^{fit}_{O_2}\,. \quad (6.9)$$

E^{GGA}_{Cu} and E^{GGA}_{Fe} represent the GGA total energies per atom of the bulk phases of fcc-Cu and bcc-Fe, respectively.

6.2.2 Convex hull of the Cu-Fe-O system

The convex hull of the computed formation enthalpies, normalized by the number of atoms, has been constructed using the phase diagram tool of the Open Quantum Material database [172] and its projection into the compositional space is reported in Figure 6.2. Each vertex represents a pure Cu-Fe-O phase, while the side that connects two phases represents the set of binary compounds of the two elements, whose distance from each vertex is proportional to the ratio of the two elements within the compound. Each point inside the triangle represents a ternary compound whose composition is determined by the distance between the point and each side of the triangle.

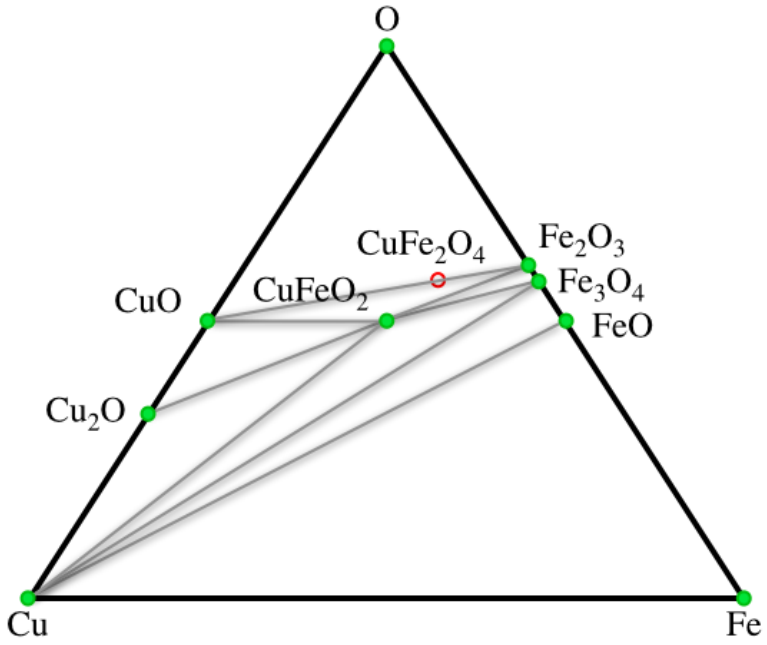

Figure 6.2

Gibbs triangle indicating the stable phases in the Cu-Fe-O system. Green (red) points represent compound that are stable (unstable) in the convex hull, while equilibrium lines are represented in grey.

The green dots represent the compounds that are thermodynamically stable and the grey lines connect two compounds in equilibrium at the limits of their stability regions. Within these small triangles, there are chemical compositions that do not correspond to a stable phase, but to a linear combination of the three stable phases by which they are surrounded, with ratio depending on the distance from each side.

The stability region of CFO is delimited by the equilibrium with Cu, Cu_2O, CuO, Fe_2O_3 and Fe_3O_4. The formation energy of the inverse spinel $CuFe_2O_4$ lies 25 meV/atom above the convex hull and the compound is represented with a red circle since it turns out to be unstable with respect to decomposition into CuO and Fe_2O_3. However, the experimental coexistence of CFO and and $CuFe_2O_4$ has been reported [60, 164], indicating that the two ternary compounds can be in equilibrium. The distance from our computed convex hull is so small that the instability could be due to some inaccuracies in describing properly the electronic structure of $CuFe_2O_4$, for which a U term may be needed also on Cu to model accurately the Cu^{2+} oxidation state, while in our approach we applied a U term only to Fe d states.

6.2.3 Compositional phase diagram

The convex hull in Figure 6.2 has been constructed at zero temperature for a system in which the stoichiometry is fixed at any particular point in the Gibbs triangle. In actual experiments the system is exposed to air at a fixed temperature and pressure and it can therefore exchange atoms with a reservoir of oxygen held at a fixed chemical potential $\mu_O(T,p)$. To model this scenario, we computed a phase diagram in which the Fe:Cu ratio is fixed, while the system is free to exchange O atoms with the gaseous reservoir. We therefore adopted a grand-canonical formalism, in which the relevant quantity is the formation free energy $\Delta G^f(T,p)$. We write the chemical potential of O as its zero temperature value plus a correction term that depends on temperature and pressure:

$$\mu_O = \frac{1}{2}E^{fit}_{O_2} + \Delta\mu_O(T,p)\,, \tag{6.10}$$

where the variation $\Delta\mu_O(T,p)$ depends on temperature and pressure according to the ideal gas law:

$$\Delta\mu_O(T,p) = \Delta\mu^0_O(T,p_0) + \frac{1}{2}k_BT\ln\left(\frac{p}{p_0}\right). \tag{6.11}$$

The temperature variation of the chemical potential at 1 atm $\Delta\mu^0_O(T,p_0)$ can be extracted from the thermochemical data reported in the NIST-JANAF database [104].

The phase diagram calculated for a range of values of $\Delta\mu_O(T,p)$ with respect to the Cu/Fe stoichiometry is shown in Figure 6.3. Assuming bulk Fe and bulk Cu as the reservoirs of Fe and Cu, and taking their total energies normalized per atom as chemical potentials, we computed the most stable Fe/O-based and Cu/O-based structure for each value of $\Delta\mu_O(T,p)$. The stability of CFO for each $\Delta\mu_O(T,p)$ has been assessed by calculating its formation energy starting from the most stable Fe/O and Cu/O structure and evaluating its position in the convex hull. CFO is stable if its formation energy lies below the convex hull, otherwise the formation of the two constituent structures, whose amount depends on the Cu/Fe stoichiometry, is energetically favored. As shown in Figure 6.3, CFO is stable in a fairly small region in which $\Delta\mu_O$ ranges from -1.60 to -1.95 eV.

The dependence of the chemical potential of oxygen on temperature and pressure is reported in Figure 6.4. At $T = 300$ K the stability range of CFO corresponds to unphysical values of pressure lower than 10^{-45} atm, while at 1000 K the allowed range of pressure goes from 10^{-9} to 10^{-5} atm. In general, the range of the allowed values for the chemical potential of the oxygen corresponds to conditions of high temperature and low pressure. The stability region of CFO is in agreement with those reported in experimental phase diagrams of Cu-Fe-O systems [164, 173, 174]. In those papers, liquid

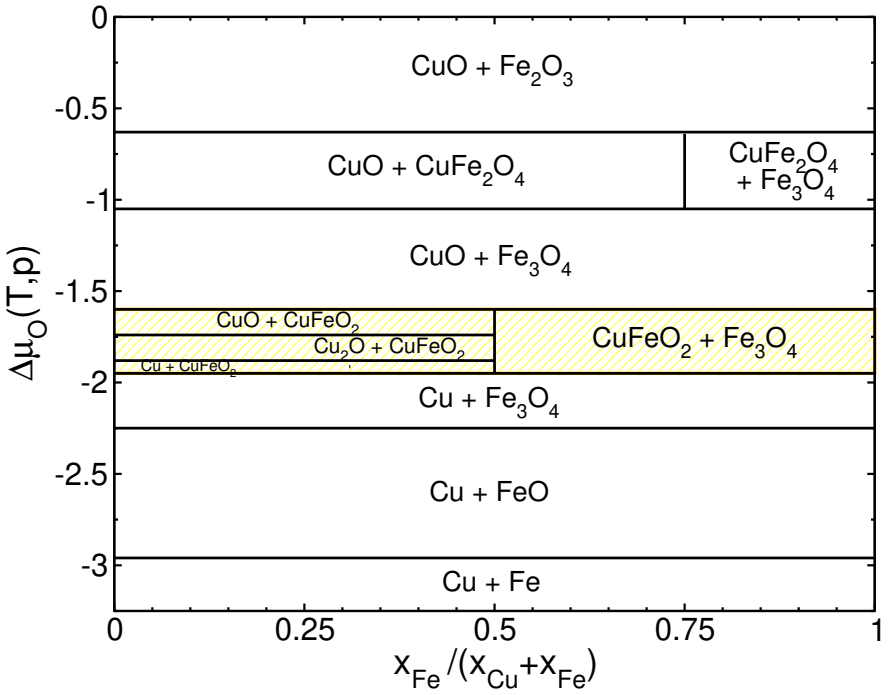

Figure 6.3

Phase diagram of the Cu-Fe-O system in which oxygen can be exchanged with a reservoir at temperature T and pressure p. For a range of values of $\Delta\mu_O(T,p)$ the most energetically stable surface is reported as a function of the Fe:Cu stoichiometry. The yellow area indicates the region of stability of CFO.

phase and spinel solid solutions appear in the phase diagram, while only solid phases have been considered in our analysis. In general, the experiments are performed at a fixed temperature or pressure, tuning the other variable to check the conditions at which a certain phase is stable. Moreover, our findings are also consistent with the fact that the experimental synthesis and growth of thin films has been carried out in one instance at 1000 K [7] and in another at 900 K (and 10^{-7} atm O_2 pressure) [60]. However, in PEC applications, CFO operates at ambient conditions and studies at 11 and 16 K have also been reported [55, 56] indicating that CFO can exist at ambient and lower temperatures. The synthesis of those samples was performed at high-temperature and then the samples were cooled down to ambient conditions. Therefore, combining our theoretical phase diagram with the experimental evidence, we can conclude that CFO exists at ambient conditions in a metastable phase and we assume the existence of a high energy barrier that prevents the segregation into other Cu-Fe-O compounds that are more stable at those conditions of temperature and pressure.

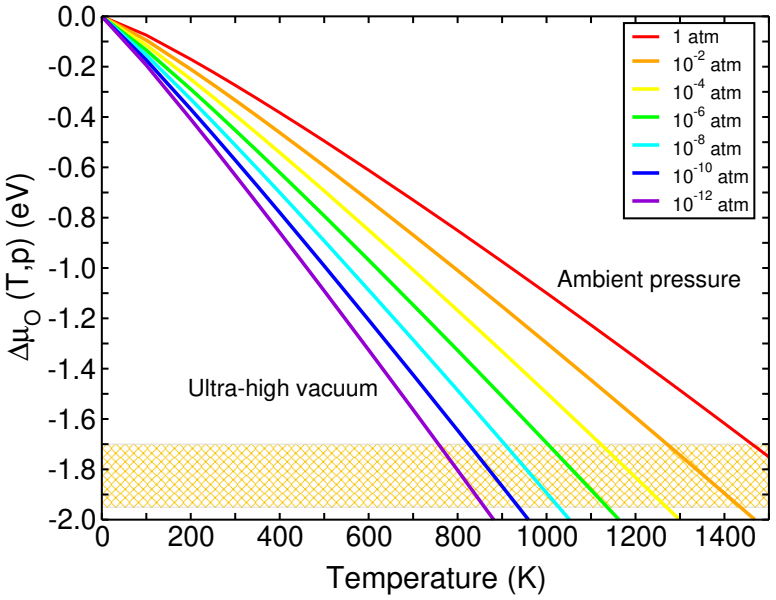

Figure 6.4

Variation of chemical potential of oxygen as a function of the temperature, for pressure ranging from ambient pressure (1 atm) to UHV conditions (10^{-12} atm). The yellow area represents the range of chemical potentials for which CFO is thermodynamically stable.

6.2.4 Stability region of $CuFeO_2$

Once a range of allowed $\Delta\mu_O$ has been determined, we aim to find the range of values for the chemical potentials of copper and iron within CFO in its stability region. While, previously, in the determination of the stability of CFO we assumed the most stable Fe/O and Cu/O structure as reservoir of Fe and Cu, we now consider a different scenario, in which we have bulk CFO in equilibrium with an oxygen atmosphere. At the thermodynamic equilibrium, the chemical potentials of the constituent elements of CFO are related by:

$$E_{CFO}^{bulk} = \mu_{Cu} + \mu_{Fe} + 2\mu_O \,, \tag{6.12}$$

where the free energy of the oxide is approximated with its total energy per formula unit. It is convenient to introduce the quantities $\Delta\mu_i$ that represent the difference between the chemical potentials of the three atomic species inside CFO and those in their respective bulk metal, or gaseous phase for the oxygen:

$$\mu_{Cu} = E_{Cu}^{GGA} + \Delta\mu_{Cu} \quad \mu_{Fe} = E_{Fe}^{GGA} + \Delta\mu_{Fe} \quad \mu_O = \frac{1}{2}E_{O_2}^{fit} + \Delta\mu_O \,. \tag{6.13}$$

We evaluate the formation energy of the compounds in the Cu-Fe-O system as a function of $\Delta\mu_i$, in the range of the allowed values of $\Delta\mu_O$. However, the variation of the

three chemical potentials is not arbitrary, since their sum is constrained by Eq.(6.12) and only two of them are independent. Equilibrium lines between two different compounds represent a set of values of the chemical potentials for which they have the same formation energy. Beyond the equilibrium line, CFO has the thermodynamic tendency to decompose to the phase that has a lower formation energy.

In Figure 6.5 we report the stability region of CFO that is obtained connecting the equilibrium lines between CFO and other compounds; in Figure 6.5(a) the stability region is reported as a function of $\Delta\mu_O$ and $\Delta\mu_{Cu}$, whereas in Figure 6.5(a) as a function of $\Delta\mu_O$ and $\Delta\mu_{Fe}$. The range of allowed values for $\Delta\mu_{Cu}$ goes from -0.13 to 0 eV, while $\Delta\mu_{Fe}$ spans a range from -1.58 to -1.21 eV, depending on the values of $\Delta\mu_O$ and $\Delta\mu_{Cu}$. We notice that the range of allowed values of $\Delta\mu_O$ is slightly reduced (-1.70 to -1.95 eV) compared to the one determined in Figure 6.3, because of the additional constraint imposed by Eq.(6.12). An accurate estimate of the chemical potentials of the constituent elements within CFO is important in the study of the formation energy of native defects, in which atoms of different species are added or removed to CFO. Moreover, we will employ the same formalism in the study of the formation energy of CFO surfaces.

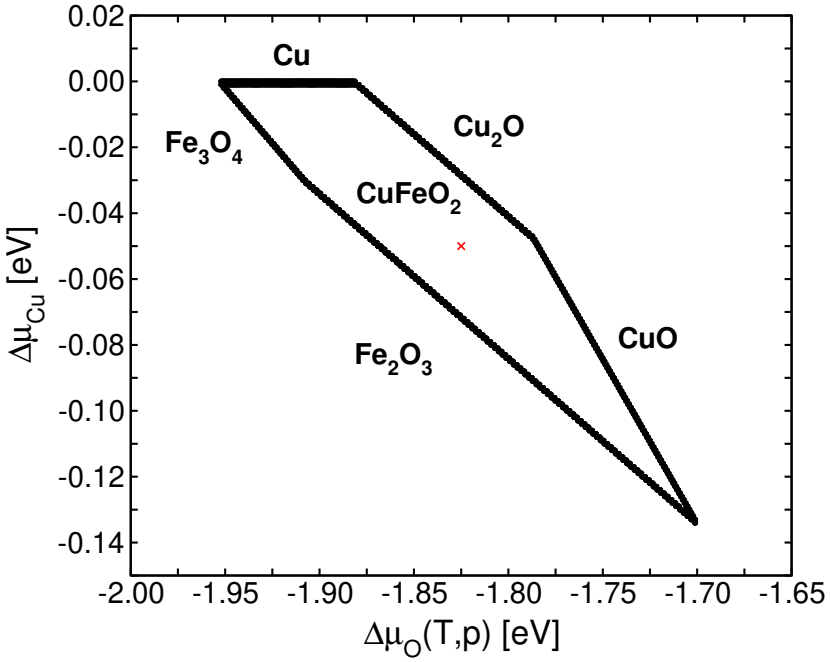

(a)

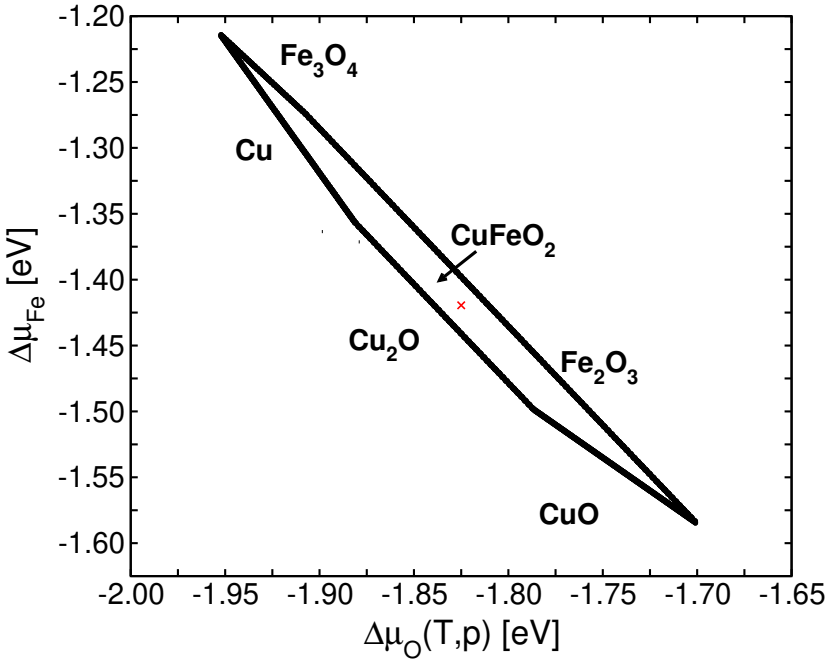

(b)

Figure 6.5

Bulk stability of $CuFeO_2$ and equilibrium lines with other Cu-Fe-O compounds a function of the chemical potential of Cu and O (a) and Fe and O (b). The red cross indicates the point at which the chemical potentials have been chosen to compute the formation energy of the defects.

6.3 Native point defects in bulk $CuFeO_2$

After establishing a range of allowed values of chemical potentials, we turn our attention to the formation of native point defects within the stability region of CFO. A systematic investigation of the formation energy of defects in CFO has not yet been reported. The role of the Cu vacancies and interstitial O in enhancing the PEC performance have been investigated by a combination of spectroscopic measurements and DFT calculations [175]. In particular, Cu vacancies have been shown to improve the PEC efficiency, facilitating the ultrafast charge separation, while the introduction of an interstitial O limits the overall performance. An accurate prediction of the formation energy of a particular defect X is important to estimate the concentration of defects at a certain temperature, which depends on the formation energy via a Boltzmann factor $\exp\left[-E^f[X]/k_BT\right]$.

The formation energy of a neutral defect is computed as:

$$E^f[X^0] = E_{tot}[X^0] - E_{tot}[\text{pristine}] - \sum_i n_i\mu_i\,, \tag{6.14}$$

where $E_{tot}[X^0]$ and $E_{tot}[\text{pristine}]$ represent the DFT total energy of the defective and the pristine supercell, respectively [107] The chemical potentials, μ_i, of the n_i added atoms are taken in the center of the stability region shown in Figure 6.5. In this way we want to determine which defects are more easily created when the material is grown at the ideal temperature and pressure. If we look outside the stability region we would find certain kinds of defects consistent with the most stable phase for those specific conditions. For instance, if the chemical potentials are taken from a region in which a binary Fe-oxide is stable, we would find a tendency to create Cu vacancies, with negative formation energies. If the chemical potentials are taken from the center of the stability region, we can estimate a variability of about 0.2 eV in the value of the formation energies, considering the range of allowed chemical potentials of the three elements.

The presence of a charged defect with charge q leads to the introduction of additional terms into Eq.(6.14):

$$E^f[X^q] = E_{tot}[X^q] - E_{tot}[\text{pristine}] - \sum_i n_i\mu_i + E^q_{\text{corr}} + q(\epsilon_F + \epsilon_{VBM} + \Delta v_{0/b})\,. \tag{6.15}$$

The electrons are exchanged with a reservoir whose energy is equal to the Fermi energy ϵ_F, measured from the valence band maximum (ϵ_{VBM}) of the pristine system. The value of ϵ_{VBM} is referred to the average electrostatic potential, which is commonly set

to zero in periodic boundary conditions (PBC) codes. $\Delta v_{0/b}$ is a potential alignment term between the pristine and the neutral defective cell, needed to work with the same reference potential [107]. We computed the average electrostatic potential in a small cube centered around a specific oxygen far away from the defect and we compare it with the corresponding value in the pristine cell.

When a defect is charged, a neutralizing background jellium is added to maintain the compatibility with PBC. However, the PBC introduce spurious interactions between the replicas of the defect, because of the slowly decaying Coulomb interaction, which scales as $q/\epsilon r$, where ϵ is the dielectric constant of the material. Several correction schemes have been proposed to remove the interaction and simulate an isolated defect [107]. In this work we employed the Makov-Payne approach which, in conjunction with the potential alignment, has been shown to provide converged formation energies even for small supercells of hematite [176]. In this scheme the charge is approximated with a point charge and the correction term, in which only the monopole-monopole interaction is considered, reads:

$$E_{\text{corr}}^{MP} = \frac{q^2\alpha}{2\epsilon L}\,, \tag{6.16}$$

where L is the cubic root of the volume, α is the Madelung constant of the lattice, and $\epsilon = 15.23$ is the dielectric constant. The electrostatic energy of an array of point charges is determined by the Madelung constant α, which depends on the geometry of the lattice. In order to determine the Madelung constant α of the lattice employed to study the defects in CFO ($4 \times 4 \times 1$ hexagonal supercell), we computed the Ewald contribution to the total energy of an array of hydrogen atoms placed at the vertexes of the supercell:

$$E_{\text{Ewald}} = \frac{q^2\alpha}{2L} \quad . \tag{6.17}$$

Inverting the previous formula we obtained a Madelung costant of 2.69 for this lattice. We computed in the same way the Madelung constant of cubic lattices to validate this model, reproducing the results reported in Ref[177].

The dielectric constant has been taken as $\frac{1}{3}\,\text{Tr}[\epsilon]$, where ϵ is the dielectric tensor, computed within Density Functional Perturbation Theory (DFPT) [161]. The electronic dielectric tensor reads:

$$\epsilon_{ij}^{el} = \begin{pmatrix} 9.18 & 0.00 & 0.00 \\ 0.00 & 9.18 & 0.00 \\ 0.00 & 0.00 & 8.42 \end{pmatrix} . \tag{6.18}$$

When also the ionic degrees of freedom are taken into account, the tensor becomes:

$$\epsilon_{ij} = \begin{pmatrix} 17.92 & 0.00 & 0.00 \\ 0.00 & 17.92 & 0.00 \\ 0.00 & 0.00 & 10.10 \end{pmatrix}, \tag{6.19}$$

giving rise to an average dielectric constant of 15.23. Previous studies have reported a dielectric constant of 20 [178].

We investigated different kinds of crystallographic point defect. We considered electron (e_p) and hole (h_p) polarons, by adding or removing an electron from the system and letting the atomic positions relax. The corresponding configuration with the 0 state of charge is represented by the pristine cell, whose formation energy is trivially 0.

We changed the number of atoms in the unit cell by adding interstitial oxygen (O_I) or creating a vacancy of copper (V_{Cu}), iron (V_{Fe}) and oxygen (V_O). In a purely ionic picture, the removal of a neutral Fe atom from a Fe^{3+} compound would leave the system with three excess holes. For this reason we investigated also the charged iron vacancies V_{Fe}^{3-}, V_{Fe}^{2-} and V_{Fe}^{-} and, for similar consideration, V_{Cu}^{-}, V_O^{+} and V_O^{2+}.

Among the defects that change the stoichiometry of the system we also investigated the antisite Cu_{Fe} and Fe_{Cu} in which one Fe atom is replaced by a Cu atom and viceversa. In order to account for the exchange of formally +1 and +3 cations, we considered different charged states, applying negative -1 and -2 charges in the Cu_{Fe} system and positive +1 and +2 to the Fe_{Cu} case.

The formation energy of the defects is shown in Figure 6.6 as a function of the position of the Fermi energy. For each kind of defect, only the most stable state of charge is represented. We will focus mainly on values of the Fermi energy in proximity of the VBM, since CFO is known to be a p-type semiconductor [7].

The defect with the lowest formation energy in this region is the copper antisite Cu_{Fe}, whose formation energy in the neutral state of charge is 0.28 eV. In this configuration, a Cu atom is placed on an octahedral site, originally occupied by a Fe. This arrangement resembles the configuration of the inverse spinel $CuFe_2O_4$ in which formal Cu^{2+} ions occupy octrahedral sites. Experimentally a competing Cu^{+}/Cu^{2+} phase has been reported [60]. The minority Cu^{2+} phase ($< 10\%$) has been attributed first to the formation of $CuFe_2O_4$, and then, when XANES measurements were performed on a pure CFO sample, to the oxidation of surface Cu^{+} into $Cu(OH)_2$ [60]. Here the delafossite structure is preserved, thus we can not strictly speak about the formation of $CuFe_2O_4$, but the relatively small formation energy indicates the ease of creating this kind of defect.

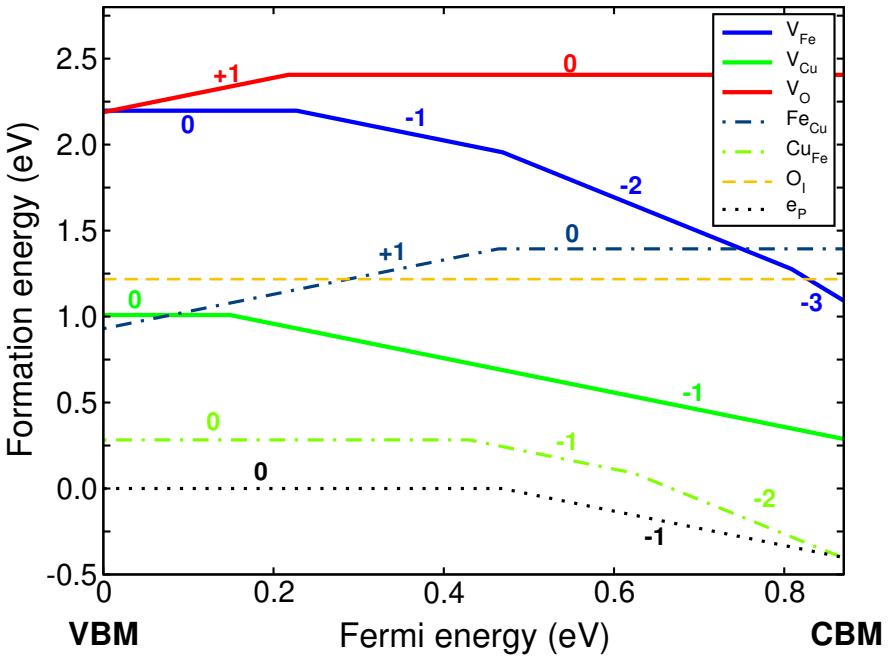

Figure 6.6

Formation energy of the defects as a function of the Fermi energy. For each defect, only the most stable state of charge is represented and indicated with the corresponding number. The defects are investigated within the CFO stability region.

The PDOS of the neutral Cu_{Fe} defect is shown in Figure 6.7. Two empty defect states with a strong Cu/O character appear within the energy gap, 0.2 eV above the VBM. The origin of these states lies in the two extra holes left by the substitution of a Fe with a Cu. The Cu contribution originates almost entirely from the defective copper, while the oxygen contribution is spread over the six oxygen atoms surrounding the defective Cu. The fact that the defect with lowest formation energy introduces holes in the system is consistent with *p*-type character of this material.

The presence of this kind of defect, however, could be detrimental for the performance of CFO as a photocathode, since these gap states, well separated from the top of the valence band, could facilitate the recombination of photogenerated charge carriers. The recombination of charge carriers mediated by states inside the gap has been proven to be a limiting factor in the PEC performances of α-Fe_2O_3 [179]. Recent experiments suggested that in CFO the surface states represent the main channel of recombination of charge carriers, which instead have a long lifetime ($\sim$ 200 ns) within the bulk [11], while earlier measurements indicated inter bandgap states as the dominant recombination path [7].

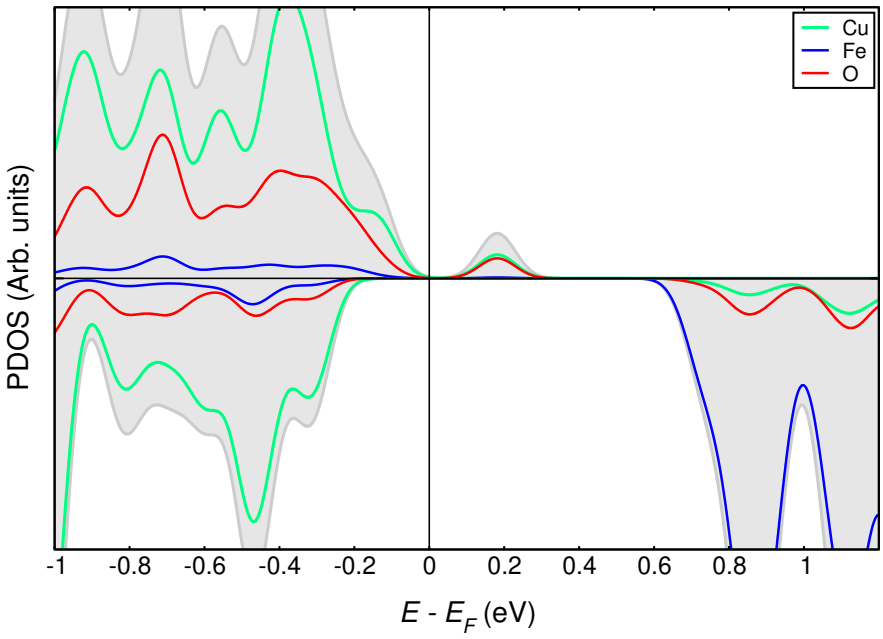

Figure 6.7

Projected density of system of the cell with the Cu antisite defect. Defect states with a strong Cu/O character appear above the Fermi energy.

We can estimate the concentration of Cu_{Fe} defects using the formula: [180]

$$D[X^q] \simeq \frac{N_X}{V} \exp\left(-E^f[X^q]/k_B T\right), \tag{6.20}$$

where N_X and V represent the number of possible defects sites and the cell volume, respectively. If we consider an average growth temperature of 900 K, and we assume that the concentration of defects is kept constant when the sample is quenched to ambient conditions, we obtain a high concentration of Cu_{Fe} defects of the order of 10^{20} cm^{-3}, corresponding to a fraction of about 2% of antisite defects. However, the ratio between different charged states of the defect could change during the quenching [176]. The high concentration of defects suggests that the bulk recombination could play a role in the low PEC performance, as it has been reported for TiO_2 [181] and α-Fe_2O_3 [179].

However, there are cases in which the presence of defects improves the PEC performance, since the defect states could lower the band gap to the visible region and enhance the charge carrier separation. In particular, oxygen vacancies have been shown to improve the PEC efficiency in NiO [182], In_2O_3 [183] and $NiCo_2O4$ [184].

In CFO the charge separation occurs via a fast delocalization of photogenerated holes to Cu d and O p states [138]. The separation is facilitated by the presence of Cu

vacancies, while it is limited by the introduction of interstitial O [175]. Further studies are required to investigate the role of the Cu antisite defect in enhancing the PEC efficiency.

The opposite antisite defect Fe_{Cu}, with overall charge +1, has the lowest formation energy of any *n*-type defect close to the VBM. In this configuration one excess electron is left in the system, in contrast with the former case. The defective Fe is placed in a unusual dumbbell arrangement with two oxygen atoms and is reduced by the extra electron into an Fe^{2+} cation.

Among the vacancies, the Cu vacancy is the defect with the lowest formation energy, 1.0 eV, while the cost of creating a O or Fe vacancy is around 2.2 eV. When a neutral copper atom is removed from the bulk, an excess hole is left in the system. The hole does not localize on a specific site, but it delocalizes on the two oxygen atoms in the dumbbell structure with the missing Cu. Two states with 0.5 occupancy appear at the Fermi level, giving the system a metallic character.

On the other hand, the system keeps a semiconducting character when a Fe vacancy is formed, despite the fact that there are three extra holes. We find three defect states, two of which are found 13 meV above the Fermi energy, and a third that is 94 meV above. The analysis of the spin density reveals an excess of positive charge on the six oxygen surrounding the missing Fe. We observed the delocalization effect also in the hole polaron, in which the extra hole is spread throughout the unit cell. The localization of the holes could be induced by adding a suitable Hubbard U also to the oxygen atoms. A systematic investigation of the localization of charge carriers as a function of the U has been reported for Fe_2O_3 [185].

Conversely, when the defect leaves the system with excess electrons they are well localized on Fe atoms, reducing one or more Fe^{3+} into Fe^{2+} and forming small polarons around them. This effect is observed both in the V_O^- and in electron polaron defect. The electron polaron is the most energetically favored defect when the position of the Fermi energy is close to the CBM, while the formation energy of the hole polaron in the considered range of Fermi energies is always higher than those of the pristine cell and of the electron polaron.

6.4 Thermodynamic stability in an electrochemical environment

To simulate the operating conditions of CFO as photocathode it is useful to investigate not only its stability in air, but also the stability in an aqueous environment. Pourbaix diagrams [186] identify the range of pH and applied potential for which a material is stable in a solution and the conditions at which it corrodes.

The applied potential is measured with respect to a reference electrode. From a computational point of view, a convenient choice is to refer the applied potential to the Standard Hydrogen Electrode (SHE) which is based on the electrochemical half-reaction:

$$\frac{1}{2}\mathrm{H_2} \rightleftharpoons \mathrm{H^+} + e^- \,. \tag{6.21}$$

At the equilibrium, the sum of the chemical potentials of $\mathrm{H^+}$ and e^-, which would be difficult to compute separately, is therefore equal to the chemical potential of gas phase $\mathrm{H_2}$, which is easily accessible in calculations.

Pourbaix diagrams are composed of equilibrium lines that separate two different phases. Each equilibrium line corresponds to the $\Delta G = 0$ condition for a chemical reaction that involves the two different phases. We consider here, for instance, the oxidation of iron into hematite:

$$2\mathrm{Fe} + 3\mathrm{H_2O} \rightleftharpoons \mathrm{Fe_2O_3} + 6\,\mathrm{H^+} + 6\,e^- \,. \tag{6.22}$$

The ΔG of this reaction is computed as:

$$\Delta G = \mu(\mathrm{Fe_2O_3}) + 6\,\mu(\mathrm{H^+}) + 6\,\mu(e^-) - 2\mu(\mathrm{Fe}) - 3\,\mu(\mathrm{H_2O}) \,. \tag{6.23}$$

Eq.(6.23) simplifies into an expression containing the standard free energy of formation:

$$\Delta G = \Delta G^f(\mathrm{Fe_2O_3}) - 6\,RT\ln(10)\mathrm{pH} + 6\,e\mathrm{V}_{SHE} - 3\Delta G^f(\mathrm{H_2O}) \,, \tag{6.24}$$

where R is the gas constant and e the electron charge. $-RT\ln(10)\mathrm{pH}$ and $e\mathrm{V}_{SHE}$ represent the change in chemical potential of protons and electrons for pH and potential different from zero, respectively. The equilibrium line between iron and hematite corresponds to the values of pH and E_{SHE} that give $\Delta G = 0$ in Eq.(6.23).

Following Ref.[187] we wrote a series of chemical reactions involving this species in an aqueous environment and the most stable phases are identified according to the ΔG of the reactions.

In the chemical reactions involving Cu species the Cu^{2+} ion has been taken as reference, in such a way that all the reactions are referred to a common reference.

$$Cu^{2+} \rightarrow Cu^{2+} , \tag{6.25}$$

$$Cu^{2+} + e^- \rightarrow Cu^{+} , \tag{6.26}$$

$$Cu^{2+} + 2e^- \rightarrow Cu_s , \tag{6.27}$$

$$Cu^{2+} + H_2O \rightarrow CuO + 2H^+ , \tag{6.28}$$

$$Cu^{2+} + \frac{1}{2}H_2O + e^- \rightarrow \frac{1}{2}Cu_2O + H^+ . \tag{6.29}$$

Similarly, the Fe^{2+} ion has been taken as reference for the reactions involving Fe:

$$Fe^{2+} \rightarrow Fe^{2+} , \tag{6.30}$$

$$Fe^{2+} + 2e^- \rightarrow Fe , \tag{6.31}$$

$$Fe^{2+} \rightarrow Fe^{3+} + e^- , \tag{6.32}$$

$$Fe^{2+} + H_2O \rightarrow FeOH^{2+} + H^+ + e^- , \tag{6.33}$$

$$Fe^{2+} + 2H_2O \rightarrow Fe(OH)_2{}^+ + 2H^+ + e^- , \tag{6.34}$$

$$Fe^{2+} + 4H_2O \rightarrow FeO_4{}^{2-} + 8H^+ + 4e^- , \tag{6.35}$$

$$Fe^{2+} + H_2O \rightarrow FeOH^+ + H^+ , \tag{6.36}$$

$$Fe^{2+} + 3H_2O \rightarrow Fe(OH)_3 + 3H^+ + e^- , \tag{6.37}$$

$$Fe^{2+} + 2H_2O \rightarrow HFeO_2{}^- + 3H^+ , \tag{6.38}$$

$$Fe^{2+} + \frac{3}{2}H_2O \rightarrow \frac{1}{2}Fe_2O_3 + 3H^+ + e^- , \tag{6.39}$$

$$Fe^{2+} + \frac{4}{3}H_2O \rightarrow \frac{1}{3}Fe_3O_4 + \frac{8}{3}H^+ + \frac{2}{3}e^- . \tag{6.40}$$

We followed the procedure described in Ref.[188] to construct a two-metals diagram. One metal, in this case Fe, has been taken as a primary component. Assuming constant activity for each stable species of the secondary metal, in this case Cu, we write different equations for the formation of CFO, one for each stable phase of Cu. Each equation is valid only in the region in which the given species of Cu is stable.

$$Fe^{2+} + Cu^{2+} + 2H_2O \rightarrow CuFeO_2 + 4H^+ , \tag{6.41}$$

$$Fe^{2+} + Cu^{+} + 2H_2O \rightarrow CuFeO_2 + 4H^+ + e^- , \tag{6.42}$$

$$Fe^{2+} + Cu + 2H_2O \rightarrow CuFeO_2 + 4H^+ + 2e^- , \tag{6.43}$$

$$Fe^{2+} + CuO + H_2O \rightarrow CuFeO_2 + 2H^+ , \tag{6.44}$$

$$Fe^{2+} + \frac{1}{2}Cu_2O + \frac{3}{2}H_2O \rightarrow CuFeO_2 + 3H^+ + e^- . \tag{6.45}$$

We calculated the Pourbaix diagram of CFO using both the experimental and the

Compound	ΔG^f_{exp} (eV)	ΔG^f_{DFT} (eV)
$CuFeO_2$	-4.77	-4.60
Fe_2O_3	-7.68	-7.51
Fe_3O_4	-10.51	-10.45
Cu_2O	-1.52	-1.61
CuO	-1.31	-1.47

Table 6.2

Experimental and computed formation free energies at ambient conditions for the solid compounds considered in the Pourbaix diagram.

computed formation free energies, adopting the procedure illustrated in Ref.[188] to take into account the presence of two different metallic species. The experimental formation energies of solid and dissolved species at 298.15 K have been taken from the atlas of Pourbaix [186], while the experimental formation energy of CFO has been extracted from Ref.[188]. We assumed the concentration of dissolved ions to be 10^{-6} M, considered as the limit of practical corrosion [186].

Several Pourbaix diagrams of bulk phases predicted with *ab-initio* techniques have been reported [113, 187, 189, 190]. We followed the approach outlined in Ref.[189] to combine DFT energies with experimental free energies of aqueous ions. The formation free energies of Cu-Fe-O compounds have been computed from the elementary constituents using the mixed GGA/GGA+U scheme, as it was previously described. We account explicitly for thermal effects only in the O_2 molecule, while the free energies of solids are approximated with their DFT total energies. The formation energy of liquid water has been kept fixed to its experimental value, -2.458 eV [104]. A comparison between the experimental and the computed formation free energies of the compounds considered in our analysis is reported in Table 6.2. The formation energy is underestimated in Fe-oxides and CFO, while Cu-oxides are predicted to be more stable, with errors in all cases within 0.2 eV.

The value of the chemical potential of aqueous ions has been taken from the Atlas of Pourbaix [186] and corrected to reproduce the experimental dissolution energy of representative solids. The tabulated chemical potentials of the dissolved ion have been shifted by the difference between the computed and the experimental formation free energy of the reference solid, divided by the number of metal atoms in the compound, as proposed in Ref.[189]. A complete list of the reference solids and the corresponding corrections is shown in Table 6.3.

Ions	Ref. solid	Experimental ΔG^f_{exp} (eV)	Computed ΔG^f_{DFT} (eV)	Correction $\Delta\mu_s^{0,DFT-exp}$ ($\frac{\text{eV}}{\text{metal ion}}$)
Fe^{3+}, $Fe(OH)_2^+$, $FeOH^{2+}$	Fe_2O_3	-7.68	-7.51	+0.085
Fe^{2+}, $FeOH^+$, $HFeO_2^-$	FeO	-2.60	-2.70	-0.10
Cu^+	Cu_2O	-1.52	-1.61	-0.045
Cu^{2+}	CuO	-1.32	-1.47	-0.15

Table 6.3

Experimental and computed formation free energy of the reference solids used to correct the chemical potential of dissolved ions.

The Pourbaix diagrams obtained with the experimental and the computed formation free energies are shown in Figure 6.8(a) and 6.8(b), respectively. The boundaries between different phases in the two diagrams are in excellent agreement. In alkaline solutions, CFO is stable in a 0.5 V window, and a small region of stability in acidic conditions, pH $\simeq 4-6$, is also observed when the experimental free energies are used. The stability region is reduced when the diagram is constructed from the DFT formation energies, as shown in Figure 6.8(b). The smaller range of stability can be ascribed to the underestimation of the formation free energy of CFO and the simultaneous overestimation of the stability of CuO, see Table 6.2.

The conditions at which the PEC measurements of Read et al. [6] and Prévot et al. [7] were performed are indicated in Figure 6.8 with a cross and a filled circle, respectively. The points are compatible with the Pourbaix diagrams, falling inside the stability region in Figure 6.8(a) and at the boundaries in Figure 6.8(b). In particular, the CFO electrode of Prévot et al. was subjected to a chronoamperometric scan for 40 hours at the potential indicated with the filled circle, without showing signs of degradation [7]. The stability region of the electrode reported by Prévot et al. at pH= 13.6 ranges from +0.3 V to +0.9 V versus RHE, corresponding to a range from −0.5 V to +0.1 V versus SHE, in perfect agreement with our Pourbaix diagram computed with the experimental values. The diagram constructed with the DFT formation energies predicts a smaller stability region, between −0.15 V to −0.4 V versus SHE. A cyclic voltammogram performed for a CFO electrode [7] displays decomposition signs consistent with Cu and Fe reduction for potentials more negative than −0.7 V versus SHE, in a region of the Pourbaix diagram where metallic Cu and Fe are the stable phases.

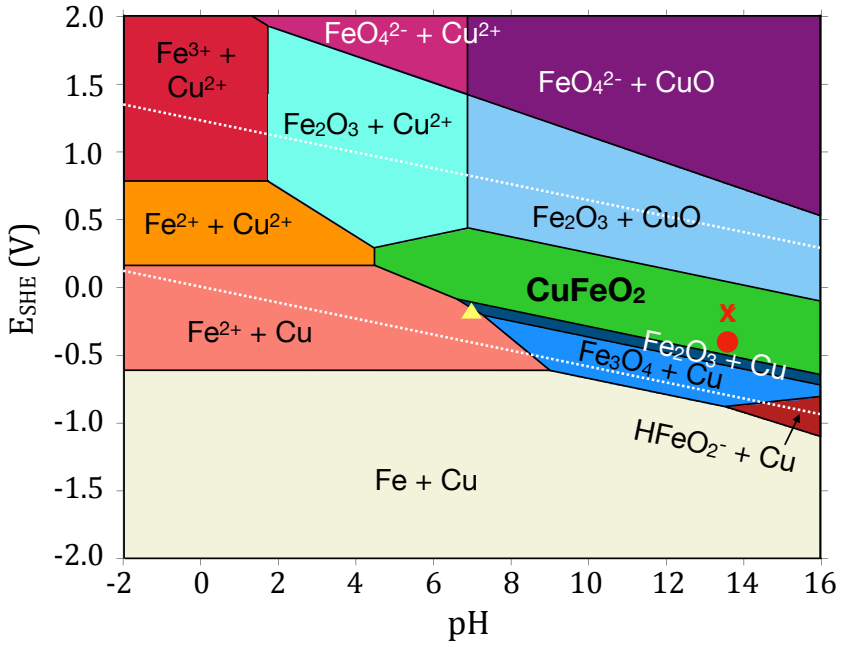

(a)

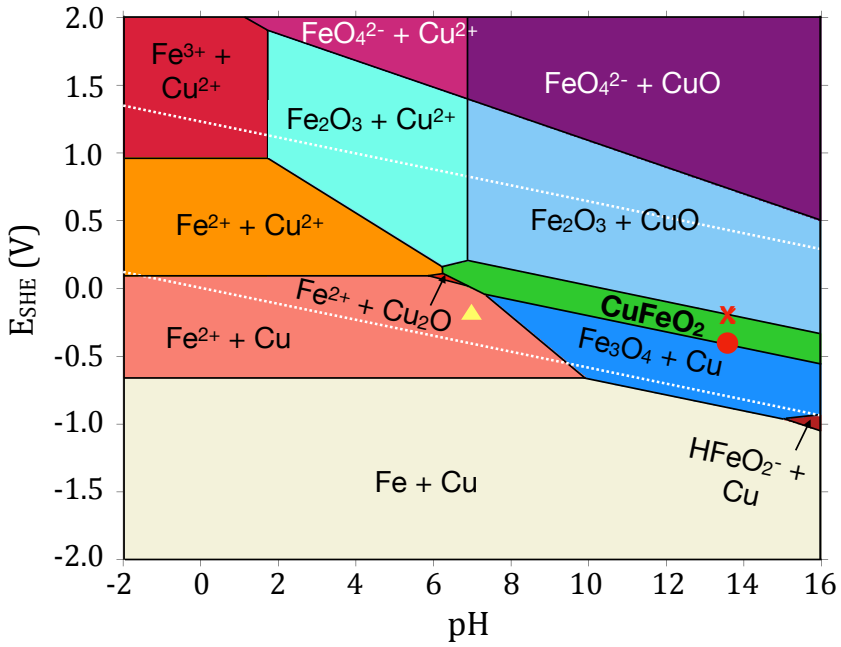

(b)

Figure 6.8

Pourbaix diagrams computed using the experimental (a) and the computed (b) formation free energies of solids phases and dissolved ions. The white dashed lines represent the redox potential of water, while the red cross and circle represent the conditions at which the PEC measurements [6, 7] were performed. The yellow triangle represents the electrochemical conditions employed in Ref. [191], in which the electrode was shown to be unstable .

Our Pourbaix diagrams are further validated by the fact that a mixed Fe-Cu oxide electrode is not stable under conditions of pH 7 and bias −0.2 V against SHE [191], showing a reductive dissolution of Fe^{3+} ions that makes the surface Fe-deficient. These electrochemical conditions, indicated with a yellow triangle in Figure 6.8, fall outside the stability region of CFO, lying where the most stable phase is represented by dissolved Fe^{2+} ions and bulk Cu, in agreement with the experimental evidence.

The stability of CFO in the electrochemical environment used in experiments is in contrast with its meta-stability in the air at the same temperature and pressure conditions. Therefore we can conclude that the aqueous environment acts to stabilize the CFO. This finding explains the origin of the remarkable stability of CFO against corrosion [7]. However, these thermodynamic considerations are not enough to explain the resistance of CFO against the photocorrosion. Indeed, when the electron is photoexcited into the conduction band, its potential is about −0.75 V versus SHE, negative enough to drive at least the reduction of Cu^{2+} into metallic Cu; one would therefore expect to observe the same photodegradation observed in Cu_2O. The enhanced stability may be due to kinetic effects that inhibit the reduction reaction.

6.5 Summary

In summary, we characterized the thermodynamic stability of bulk CFO in air and in presence of an electrolyte. According to our analysis, CFO is stable in air for high temperature and low pressure conditions, in agreement with the experimental growth conditions. However, within the range of allowed chemical potentials we found a low formation energy for a Cu antisite defect that introduces states within the energy gap. We also evaluated the stability of CFO in an aqueous environment as a function of pH and applied potential. The Pourbaix diagram constructed using the DFT formation energies reproduces the one constructed with the experimental formation energies with a small margin of error. We found that the liquid environment strongly stabilizes the CFO compound compared to air, so that the experimental conditions of applied potential and pH fall in the region of thermodynamic stability of CFO, thus explaining the origin of the remarkable stability of this photocathode material.

This analysis also allows us to benchmark our theoretical predictions against experimentally known quantities. Using *state-of-the-art* theoretical tools we are able to reproduce the Pourbaix diagram with a small margin of error. Moving away from what

has been already determined, we can use the same tools to predict with a good level of confidence quantities that are difficult to determine experimentally, such as the relative stability of different facets and surface terminations in contact with the electrolyte as a function of bias and pH, the electrostatic potential alignment or the structure of the double layer formed at the interface. This will be the topic of the next Chapter.

7

Characterization of $CuFeO_2$ surfaces in vacuum and in an electrochemical environment

CONTENTS

To date, comparatively little attention has been given to the investigation of the surfaces of the CFO photocathodes, either in vacuum or aqueous conditions. In particular, recent theoretical works focused very specifically on bulk properties of CFO [10, 138, 175]. However, the role of the CFO surfaces in the band edge alignment and on the availability of charge carriers for the HER cannot be overlooked.

A theoretical approach for predicting structural and electronic properties of PEC interfaces requires the generation and validation of realistic and complex structural models and an accurate description of the electronic properties of interfacial systems [120].

In this chapter we present the first steps along these lines by computing phase diagrams for the CFO surfaces in vacuum and in presence of an electrolyte, and investigating the complex dynamics of the CFO/water interface in the dark and under illumination.

7.1 Computational setup

The DFT calculations have been carried out using the Quantum ESPRESSO code [139, 140], with Optimized Norm-Conserving Vanderbilt pseudopotentials [76, 77] as in the previous chapters. The kinetic energy cutoff was set to 80 Ry, while due to the different sizes of the supercell for slab calculations the first Brillouin zone was sampled with different **k**-point meshes. For slabs terminated with (0001) surfaces we adopted a $4\times2\times1$ mesh and for $(11\bar{2}0)$ surfaces a $3\times1\times1$ **k**-points sampling. For the treatment of electron exchange and correlation we apply the PBE+U, using the self-consistent value of $U_{scf} = 4.1$ eV for the Fe ions.

The surfaces have been modelled using symmetric slabs with two identical terminations in order to avoid the formation of a net dipole moment within the unit cell. The slab is periodically replicated, with 12 Å of vacuum in the direction perpendicular to the surface to avoid spurious interactions between periodic replicas. For the (0001) surface we found that a thickness of ~ 15 Å, corresponding to three FeO_6 layers, yields surface energies converged within 3 meV/$\tilde{\text{Å}}^2$, while for the $(11\bar{2}0)$ surface a 6 Å thick slab composed of 5 layers is sufficient to converge the surface energy to within 1 meV/ Å^2. In the construction of the Pourbaix diagram we replicated the slabs in the xy plane to form supercells. In particular, we adopted a $4\times2\times1$ supercell, with area $\sim 12.4\times10.7$ Å^2, for the (0001) surface and a $2\times2\times1$ for the $(11\bar{2}0)$, with area $\sim 10.7\times17.4$ Å^2.

To study the band edge alignment, the supercells were surmounted by 15 Å of explicit water molecules, corresponding to 77 and 59 water molecules for the $(11\bar{2}0)$ and the (0001) surface, respectively. A vacuum region of ~ 10 Å divides the explicit water and the replica of the bottom surface. We performed ab-initio molecular dynamics (AIMD) simulations with the Quickstep code [192] of the `CP2K` software package, which adopts a mixed Gaussian and plane-waves basis set. We employed the molecularly optimized (MOLOPT) DZVP-SR Gaussian basis set for the wavefunctions, and a plane-wave cutoff of 500 Ry for the charge density, while the Goedecker-Teter-Hutter (GTH) pseudopotentials [193] were used to model the electron-ion interactions. We adopted the rVV10 functional, setting the value of the parameter b to 9.3 to get a correct description of the structural properties of the explicit water. [194–196] The Hubbard U correction on the d states of Fe was set equal to 3.3 eV, in analogy with what has been reported for Fe_2O_3. [197]

We run the AIMD simulations in the NVT ensemble for a total simulation time between 12 and 15 ps, setting the temperature to 360 K through a velocity rescaling

(CSVR) thermostat. [198] The mass of the hydrogen atoms was set equal to the mass of deuterium, 2 amu, and the time step adopted was 1 fs. The profile of the electrostatic potential across the CFO-water interface has been determined by planar averages on planes parallel to the surface and by averaging the potential over snapshots extracted every 50 fs along the AIMD simulation, discarding the first $2-3$ ps of the simulation for equilibration.

7.2 Model photocathode surfaces

We considered two different cuts along orthogonal crystal planes in the CFO delafossite structure. For the construction of the surfaces and their different terminations, it is convenient to adopt a hexagonal representation of the $CuFeO_2$ as opposed to the primitive rhombohedral one. First, we investigated the basal (0001) plane, whose top view is depicted in Figure 7.1(a) and corresponds to crystal growth along the [111] direction in rhombohedral coordinates.

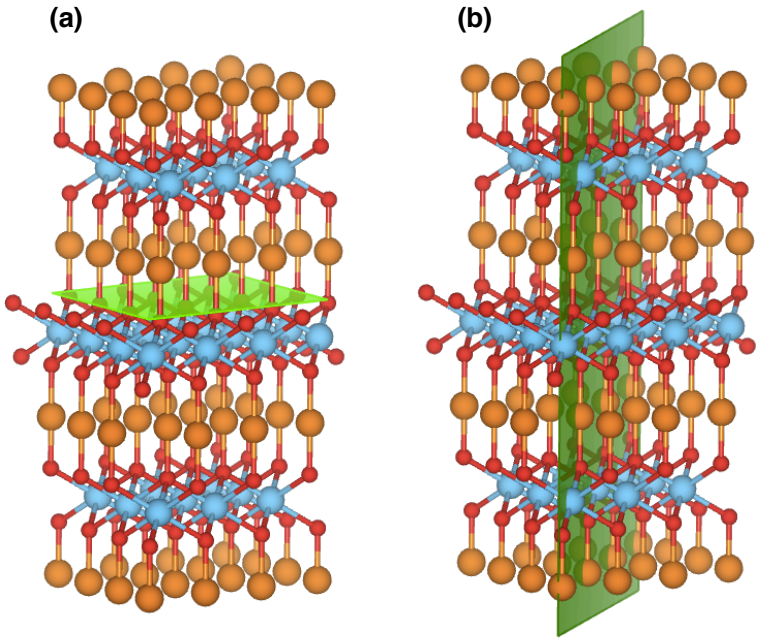

Figure 7.1

Lattice planes that we used to cut the delafossite structure of CFO along the (0001) (a) and $(11\bar{2}0)$ (b) direction. Orange, blu and red spheres represent Cu, Fe and O atoms, respectively.

The basal plane emerges as a natural starting point for the investigation of CFO surfaces for several reasons. First of all, from an experimental point of view, (0001) terminations are reportedly accessible via templated epitaxial growth. [60, 199, 200]. In other delafossite materials, [201–203] the (0001) surfaces have given rise to technologically relevant electronic features such as localized surface states and in-plane conductivities. [201] Finally, archetypal surfaces of the delafossite crystal can be derived from the (0001) plane since chemically-distinguishable terminations arise very naturally from the stacking of A_x and B_xO_{2x} layers.

The second cut we considered is in the $(11\bar{2}0)$ direction, shown in Figure 7.1(b), which is perpendicular to the basal (0001) plane. This facet has been investigated to study nanocubes and nanoplates of CFO as Fenton catalysts for the H_2O_2 activation [204]. This simple configuration presents a linear stacking of $CuFeO_2$ units containing Cu, Fe and O atoms in a stoichiometric ratio. In addition, termination models based on the $(11\bar{2}0)$ plane belong to the Tasker(I) group [205] and are overall dipole free, as it has been reported for $LiCoO_2$ [166] and $CuAlO_2$ [206], making them ideal for consideration in this work.

The Figures 7.2(f-h) depict three possible terminations that arise from (0001) planes. It's worth noticing that the (0001) is a polar Tasker (III) surface and the consequence of adopting a symmetric slab with two identical terminations is the loss of the Cu/Fe/O stoichiometric ratio within the unit cell. Among these three systems, two have non-stoichiometric cells and are referred to as (0001) Fe/O (Figure 7.2h) and (0001) Cu (Figure 7.2f). The two non-stoichiometric surfaces can be considered as the Fe_xO_{2x} layer at zero and full Cu^+ coverage. The (0001) Fe/O surface is O rich, with no undercoordinated transition metal ions present. We considered also a termination with half Cu coverage, which has an overall stoichiometric supercell, denoted as (0001) Cu_s (Fig 7.2g).

Specifically, here we investigate three different termination models based on the $(11\bar{2}0)$ crystal plane. Each of the considered systems are presented in Figure 7.2(c-e). In general, the termination of the $(11\bar{2}0)$ surfaces is unambiguously defined, given the equivalence of the layers. However, we considered also two defective surface models, which have overall non-stoichiometric supercells. We denote as $(11\bar{2}0)$ Cu/O surface, Figure 7.2(c), the system in which the outermost layers are completely Fe-depleted. In this case all the cations are coordinated as in the bulk structure, while the oxygen ions in the two outermost layers are undercoordinated. In contrast, the surface Cu-depleted in the uppermost layer, the $(11\bar{2}0)$ Fe/O system presented in Figure 7.2(d), has dangling O-bonds exposed to the vacuum. In the pristine stoichiometric $(11\bar{2}0)$, which has

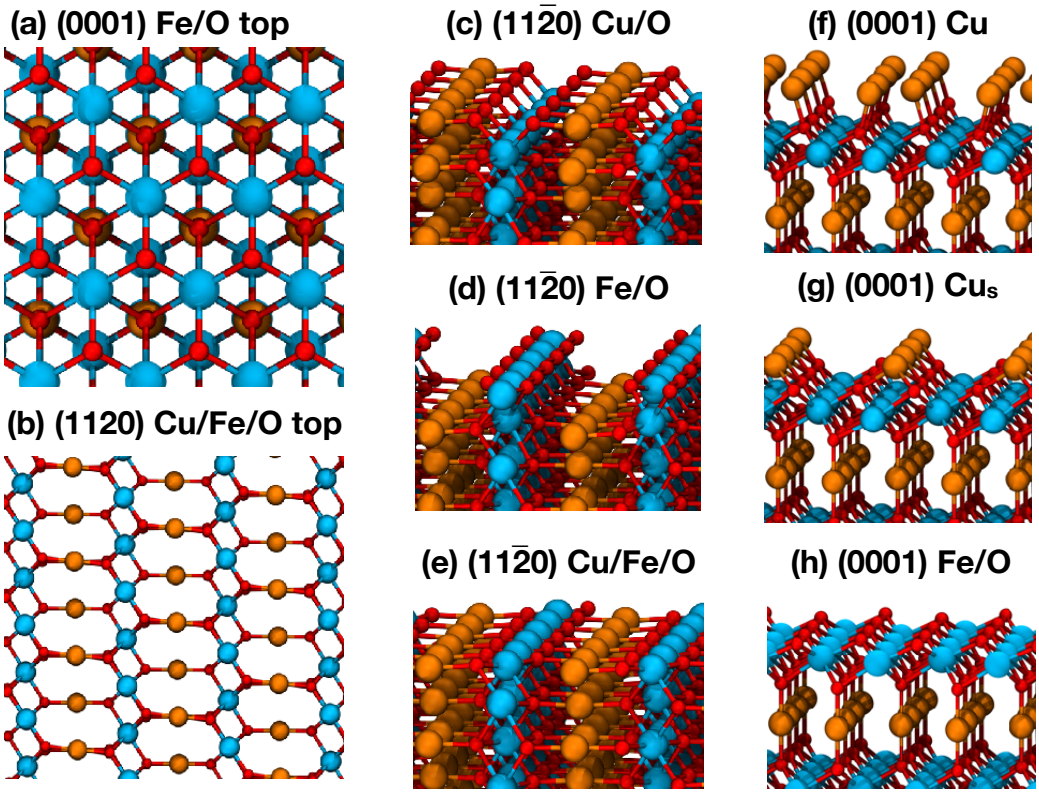

Figure 7.2

Top and side view of the various terminations which are screened in our simulations. (a-b) Top views of the two different orientations, (c-h) side views detailing the optimized geometries of the (11$\bar{2}$0) (c-e) and (0001) surfaces (f-h). Orange, blu and red spheres represent Cu, Fe and O atoms, respectively.

no intrinsic vacancies, the O and the Fe ions in the outermost layers have one and two dangling bonds, respectively.

We have considered an antiferromagnetic arrangement of the Fe ions in the bulk crystal that we cut to construct the slabs to account for the paramagnetic behaviour of CFO at room temperature [10]. Among the different antiferromagnetic structures, we considered the AFMI configuration, reported in Figure 5.2(c). This antiferromagnetic structure consists in layers of Fe atoms with a zero net magnetization, in which each layer is formed by rows of atoms with opposite magnetization. In the resulting (11$\bar{2}$0) slabs, each layer is uniformly magnetized but consecutive layers have opposite magnetization, while in the (0001) slabs the overall magnetization is zero, since each layer contains an equal number of oppositely spin-polarized Fe ions, resembling the bulk structure.

On top of the described surfaces, we also considered the thermodynamic drive for the

formation of surface point defects in the form of Fe, Cu and O vacancies. As it has been reported for $LiCoO_2$ [166], which has the same $R\bar{3}m$ symmetry as CFO, O vacancies on top of the (0001) termination could help stabilizing the surface in terms of charge redistribution.

7.3 Structural and electronic properties of the surfaces

The (0001) Fe/O slab is composed of alternating Cu and ochtahedral FeO_6 layers, as shown in Figure 7.2(h). The slab is constructed with two identical Fe/O terminations to avoid the formation of a dipole moment in the unit cell, due to the polarity of the (0001) surface. The average thickness of the FeO_6 layers in the center of the slab is 2.09 Å, while at the surface the oxygen atoms get closer to the central Fe ion and the thickness is 1.97 Å. Moreover, the dumbbell O-Cu-O structure becomes asymmetric when one of the two oxygen atoms belongs to the external O-Fe-O layers. In this case, the half side pointing towards the external layer is slightly shorter, 1.80 Å, than the half pointing towards the center, which keeps the bulk-like bond length, 1.84 Å.

The (0001) Cu termination, having one undercoordinated Cu ion per surface oxygen, reconstructs to form dimers, while the stoichiometric (0001) Cu_s termination has undercoordinated Cu ions exposed to the vacuum resulting in strong perturbations to the geometry of the surface layers during the optimization process. The external Cu ions deviate from their bulk positions in order to occupy 3-fold hollow sites created by the hexagonal arrangement of O atoms below. This kind of reconstruction has been reported theoretically for other cuprous delafossite materials [202].

The PDOS of a 13 Å thick (0001) Fe/O slab is reported in the top panel of Figure 7.3. We report the PDOS for a single spin polarization, since each layer is composed of an equal number of Fe ions with opposite magnetization and the density of states is symmetric in the two spin channels. The (0001) Fe/O slab has a metallic behaviour, showing a peak at the Fermi level with a prevalent O character. In particular, the brown dashed line in Figure 7.3(a) indicates that this peak is delocalized among the oxygen atoms in the outermost O-Fe-O layers. The Fe ions in the surface layer are still in their Fe^{3+} oxidation state, but the repulsion of the delocalized charge on the surrounding oxygen atoms pushes the energy of the states with Fe d character ~ 1 eV higher than the bulk-like counterpart, as shown by the light-blue dashed line in Figure 7.3.

The origin of the metallic character resides in the loss of the Cu/Fe/O stoichiometric

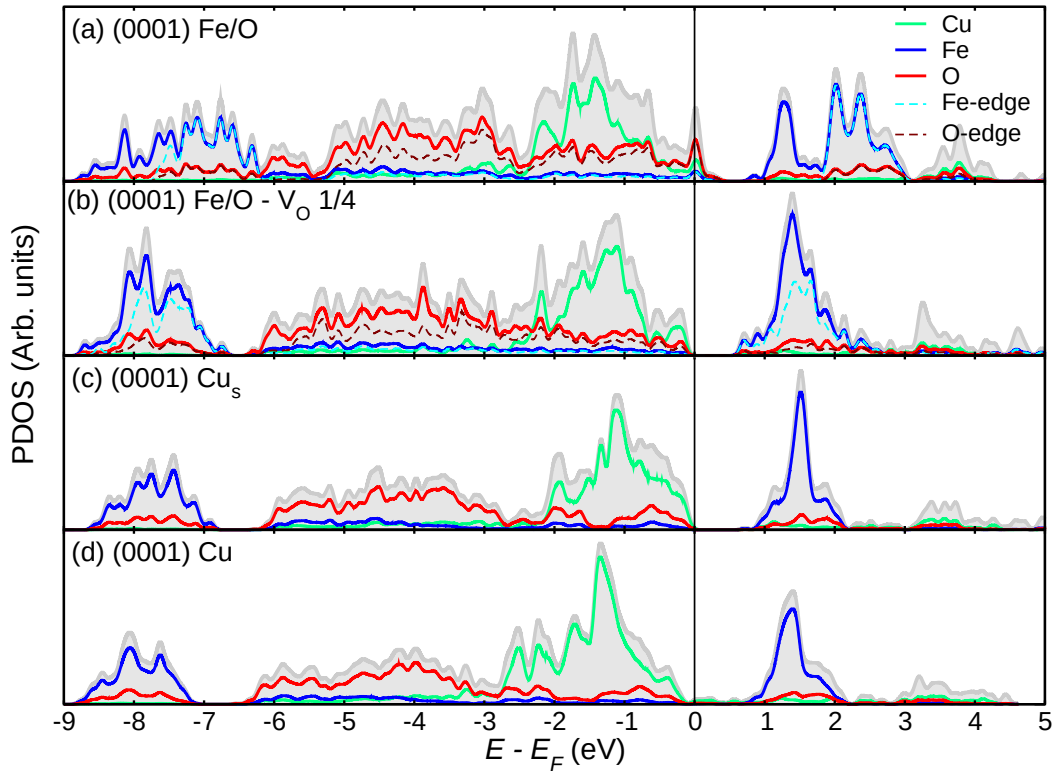

Figure 7.3

Projected density of states of a (0001) slab with the different terminations. Pristine Fe/O termination (a), and Fe/O termination with one 1/4 oxygen vacancies in the outermost layer (b). Stoichiometric Cu termination with 1/2 ML of Cu (c), non-stoichiometric termination with 1 ML Cu (d). The grey areas represent the total density of states.

ratio due to the symmetric construction of the slab. Two identical Fe/O cleavage planes lead to a globally Cu-deficient unit cell and, in a pure ionic picture, each missing Cu leaves the system with an excess hole. The redistribution of charge forming a metallic surface layer is a possible mechanism for stabilizing polar surfaces [207] and it has been reported also for $LiCoO_2$ [166], which has the same $R\bar{3}m$ symmetry of CFO. Alternative ways that involve modifications in the electronic structure of the surface layer for stabilizing polar surfaces have been reported [207]. Among them, a mixed valence of the cations at the surface, half of which are in the M^{3+} oxidation state and the other half in the M^{4+}, guarantees the redistribution of the charge, ensuring a global charge balance [166]. However, the occupied states with Fe character lie 8 eV below the Fermi, thus it is highly unlikely that a hole localizes on a Fe atom, even setting an *ad-hoc* large value of the Hubbard U parameter.

Conversely, an oxygen vacancy in the outermost layer could provide the charge that

stabilizes the surface [166], in particular when the excess charge due to the vacancy, formally 2 electrons per missing oxygen, compensates for the excess holes, provided that the Fe cations keep the Fe^{3+} oxidation state. This condition is achieved when 1/4 of the exposed oxygen atoms are removed. The corresponding slab loses the metallic character, restoring the semiconducting behaviour as reported in the Figure 7.3(b). The compensation of the excess charges makes the electronic structure of the surface compatible with the bulk-like behaviour. The peak at the Fermi level disappears and the manifold of surface states with Fe character overlaps with that of the bulk-like states. According to the phase diagram, this termination is energetically favored over the pristine metallic (0001) Fe/O termination.

Alternatively, the surface can be terminated with half a monolayer (ML) of Cu on both sides [166], as in the Cu_s termination, to ensure a global neutrality of the slab and an equal charge distribution on the two facets. The PDOS of this configuration is reported in Figure 7.3(c). Polar surfaces could also be stabilized by the adsorption of stabilizing species [207]. The charge that compensates for the holes left by the lack of copper in the (0001) Fe/O surface can be provided not only by an oxygen vacancy but also by the addition of as many hydrogen atoms on the surface as the number of holes. Specifically, the undercoordinated oxygen atoms at the surface act as active sites for the adsorption of hydrogen atoms and the charge compensation is achieved when half of them are passivated. Finally, the PDOS of the non-stoichiometric Cu-terminated (0001) surface is reported in Figure 7.3, showing small peaks at the Fermi level.

The pristine slab with the $(11\bar{2}0)$ termination consists in equal stoichiometric layers, as shown in Figure 7.2(e). The inter-layer distance in the bulk-like region is 1.55 Å, while the two outermost layers of each side get closer to each other, 1.46 Å, during the relaxation process. Each Fe atom is coordinated with six oxygen atoms, two of them lying in the same layer and four in the two adjacent layers, with a bond length of 2.08 Å in the unrelaxed structure. The Fe at the external layers have therefore two dangling bonds and the bond length with the oxygen lying in the same layer is reduced to 1.90 Å. The consequence of this rearrangement is a slightly distorted O-Cu-O dumbbell at the surface, in which the O-Cu-O angle is 174° instead of 180°.

The projected density of states (PDOS) of a relaxed 12 Å thick slab (9 layers) with the $(11\bar{2}0)$ termination is reported in Figure 7.4. The projection onto the atoms in the outermost layers, in which the Fe atoms have the majority-spin magnetization, is indicated with dashed lines. The surface states differ from the bulk-like behaviour especially in the lowest conduction states, which have Fe *d* character. The surface states associated with the exposed Fe atoms form a peak which lies ~ 0.4 lower in energy than the peak

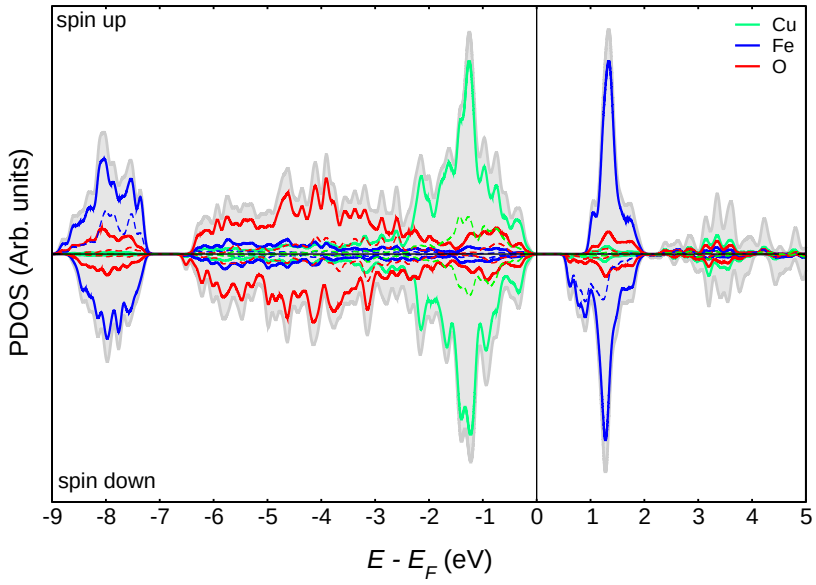

Figure 7.4

Projected density of states of a 12 Å thick slab (9 layers) with the pristine $(11\bar{2}0)$ termination. The dashed lines indicate the projections onto the atoms in the outermost layers.

corresponding to the Fe in the central bulk-like layers, due to the different coordination number of the external Fe. Conversely, the projection onto the wavefunctions of the exposed Cu and O atomic gives results that resemble the bulk-like behaviour.

The PDOS of the $(11\bar{2}0)$ surfaces Fe-depleted (Cu/O termination) and Cu-depleted (Fe/O termination) are reported in Figure 7.5. In both cases, the missing cations leave extra holes in the system which are delocalized among different surface atoms, with the appearance of states at the Fermi level and just above.

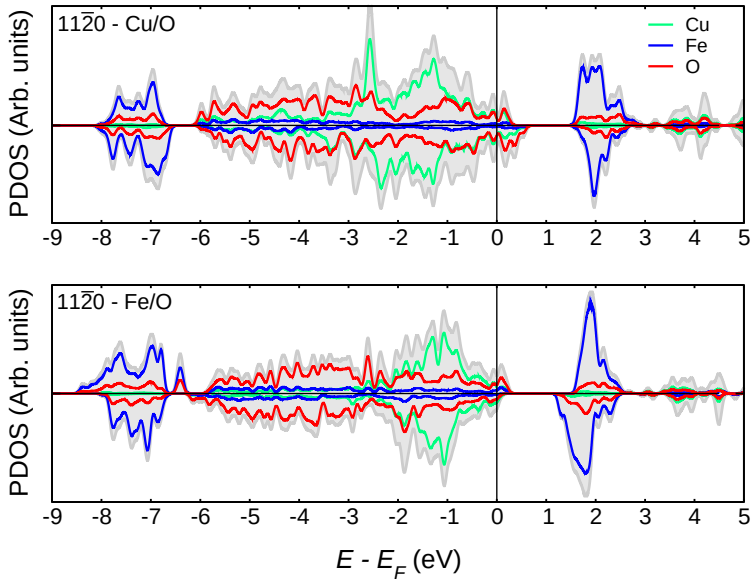

Figure 7.5

Projected density of states of 12 Å thick slabs (9 layers) with the (11$\bar{2}$0) Cu/O termination (top panel) and (11$\bar{2}$0) Fe/O termination (bottom panel).

7.4 Thermodynamic stability in air

In order to evaluate the thermodynamic stability of each surface, we have applied the *ab initio* thermodynamics formalism [101, 102]. In this approach, the surface is in equilibrium with an oxygen atmosphere at a certain temperature and pressure and the underlying bulk material acts as a thermodynamic reservoir. The relative thermodynamic stability of the different surfaces is assessed by comparing their surface free energies, which represent the work required to create each surface. If the surface is modelled as a slab with two identical terminations whose area is A, the surface free energy is computed as:

$$\gamma = \frac{1}{2A}\left(G_{\text{slab}} - \sum_i N_i \mu_i\right) \quad , \tag{7.1}$$

where G is the Gibbs free energy of the slab while μ_i and N_i represent the chemical potential and the number of atoms of the ith species and the factor 2 takes into account that the surface has two identical terminations. In the following, volumetric and entropic contributions to the Gibbs free energy of solids will be neglected and G_{slab} is approximated with the total energy E_{slab} of the DFT calculation.

The assumption of thermodynamic equilibrium in the bulk material introduces a constraint on the chemical potentials of the constituent species:

$$\mu_{Cu} + \mu_{Fe} + 2\mu_O = E^{bulk}_{CuFeO_2} \quad , \tag{7.2}$$

As we have done in the construction of the bulk phase diagram, it is convenient to introduce the quantities $\Delta\mu_i$ that represent the difference between the chemical potentials of the three atomic species inside CFO and those in their respective bulk metal, or gaseous phase for the oxygen:

$$\Delta\mu_{Cu} = \mu_{Cu} - E^{bulk}_{Cu} \quad , \quad \Delta\mu_{Fe} = \mu_{Fe} - E^{bulk}_{Fe} \quad , \quad \Delta\mu_O = \mu_O - \frac{1}{2}E^{mol}_{O_2} \quad . \tag{7.3}$$

The total energy per atom of fcc-Cu and bcc-Fe are taken as reference values for the chemical potentials of Cu and Fe in their metallic phase, while we considered as the chemical potential of gaseous oxygen the total energy of an isolated O_2 molecule, corrected in order to reproduce the total energy of non-transition metal oxides, following the method of Wang et al. [152] The constraint in Eq.(7.2) can be rewritten in an expression that involves only the deviations $\Delta\mu_i$:

$$\Delta\mu_{Cu} + \Delta\mu_{Fe} + 2\Delta\mu_O = \Delta G^f_{CuFeO_2} \quad , \tag{7.4}$$

where $\Delta G^f_{CuFeO_2} = E^{bulk}_{CuFeO_2} - E^{bulk}_{Cu} - E^{bulk}_{Fe} - 2(\frac{1}{2}E^{mol}_{O_2})$ is the formation free energy of CFO from the elementary constituents at zero temperature and zero pressure (formation enthalpy), whose computed value is -5.12 eV. The definitions of $\Delta\mu_i$ as in Eq.(7.3) set an upper bound for their values, which cannot exceed 0 in order to avoid the decomposition into bulk Cu, bulk Fe and a condensed phase of gaseous oxygen. Moreover, since the sum of the $\Delta\mu_i$ is constrained to $\Delta G^f_{CuFeO_2}$ by Eq.(7.4), only two of them can be varied independently and the lower bound for each $\Delta\mu_i$ is determined by setting the other two to zero. In this sense, the lower bound for $\Delta\mu_{Cu}$ and $\Delta\mu_{Fe}$ corresponds to $\Delta G^f_{CuFeO_2}$, while it is $\Delta G^f_{CuFeO_2}/2$ for $\Delta\mu_O$:

$$-5.12 \text{ eV} \leq \Delta\mu_{Cu} \leq 0 \quad , \quad -5.12 \text{ eV} \leq \Delta\mu_{Fe} \leq 0 \quad , \quad -2.56 \text{ eV} \leq \Delta\mu_O \leq 0 \quad . \tag{7.5}$$

In the original formulation of *ab-initio* thermodynamics, based on binary transition metal oxides, the surface energies are commonly reported as a function of $\Delta\mu_O$, while the chemical potential of the metal is implicitly determined via the total energy of the oxide [101, 102]. Several calculations of the free energy of the surfaces of ternary oxides have been reported. [166–168, 208–211] Since only two chemical potentials are independent, the surface energies are usually reported either as a function of the chemical potential

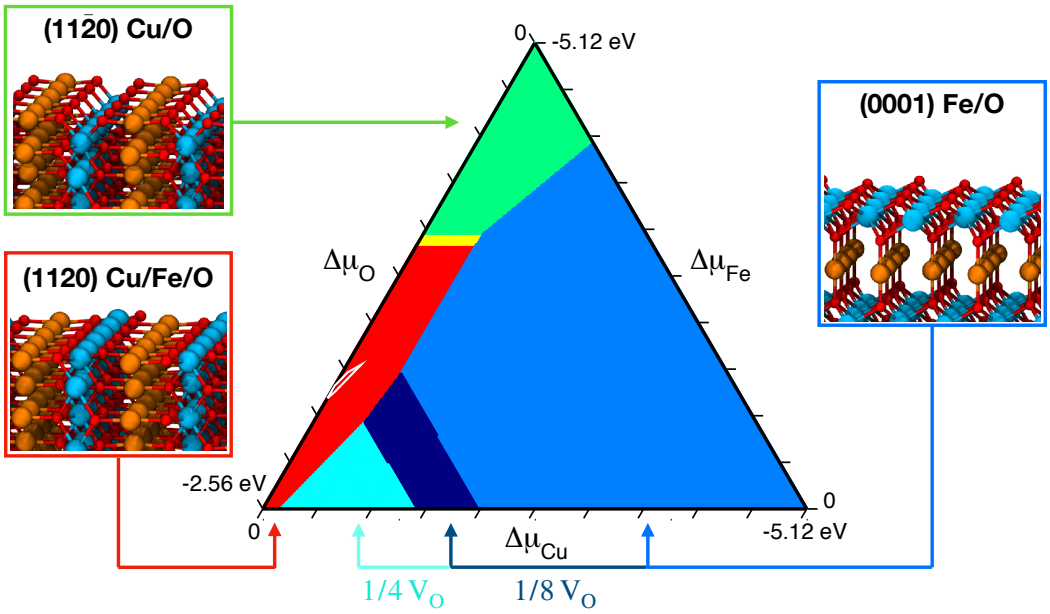

Figure 7.6

Ternary plot representing the surface phase diagram. The surface with the lowest surface energy is reported for each point within the ternary plot, which represent a triplet of chemical potentials values.

of the oxygen, for selected values of the chemical potential of one metallic species, or in a 2D plot, in which the most stable termination is plotted as a function of two chemical potentials. Herein, we follow the approach of Jiang et al. [211], plotting the surface with the lowest surface energy in a ternary plot to show explicitly the dependence on each chemical potential.

The phase diagram of CFO surfaces is reported in Figure 7.6 as a function of $\Delta\mu_i$. The three vertexes of the triangle in Figure 7.6 correspond to the conditions in which two among the three $\Delta\mu_i$ assume their highest allowed value. In particular, at the upper vertex $\Delta\mu_O = \Delta\mu_{Cu} = 0$ and $\Delta\mu_{Fe} = -5.12$ eV. This limiting situation corresponds to Cu- and O- rich conditions, while Fe is deficient since its chemical potential assumes the lowest possible value. Analogously, the bottom-left and the bottom-right corners correspond to O- and Cu-deficient conditions, respectively. The side of the triangle opposite to the vertex in which a certain species is deficient identifies the richness condition of the same species. The coordinates of each point within the triangle are determined by drawing parallel lines to each side of the triangle passing through the point and determining the distance from the parallel side. For each triplet of $\{\Delta\mu_i\}$ the surface with the lowest surface energy is reported in the ternary plot.

Three different terminations are favored in the three limiting cases. When $\Delta\mu_{Fe}$ and $\Delta\mu_O$ are close to zero, the (0001) cut with the Fe/O termination represents the most stable surface and the stoichiometry of the employed slab ($Cu_4Fe_6O_{12}$) is consistent with the Cu-deficient conditions. A large portion of the diagram is dominated by this termination, which has a lower surface energy than the Cu-terminated (0001) surfaces, regardless of the chemical potentials. This difference may be due to the fact that, despite surface reconstructions, the (0001) Cu-terminated expose uncoordinated Cu atoms and it has been shown that the presence of undercoordinated transition metal ions exposed to the vacuum could lead to higher values of the surface energy. [212] In O-poor conditions, the O vacancies on the (0001) surface are termodynamically stable and appear in the phase diagram in Figure 7.6. The lower the chemical potential of the oxygen, the larger is the number of O vacancies on the surface, whose density varies from 1/8 of the total exposed oxygen atoms to 1/4. This last configuration is of particular interest, because the excess charge given by the removal of one oxygen atom every 4 compensates exactly for the holes due the Cu-deficiency in the stoichiometry, and all the ions in the crystal are in their bulk oxidation state.

The $(11\bar{2}0)$ surface is the most stable termination when $\Delta\mu_{Cu}$ is approaching zero. In this Cu-rich conditions, the pristine $(11\bar{2}0)$ surface is the most favorable one for values of $\Delta\mu_{Fe}$ ranging from 0 to -3 eV. When $\Delta\mu_{Fe}$ becomes lower than -3 eV, iron vacancies on the surface begin to appear and the completely Fe-depleted $(11\bar{2}0)$ termination is the most stable one when $\Delta\mu_{Fe}$ is close to its lowest allowed value. In these Fe-deficient (Cu-rich) conditions the Cu-based binary oxides are thermodynamically stable in the bulk phase diagram,[1] and this is reflected in the Fe-depleted termination of the slab ($Cu_{21}Fe_{15}O_{42}$).

The triangle in Figure 7.6 identifies the most stable termination in the range of all the allowed values for each $\Delta\mu_i$. A relevant subset of chemical potentials is the one that guarantees the stability of the underlying bulk delafossite CFO phase. As shown in the previous Chapter, the stability region of CFO is delimited by the intersection of the equilibrium lines with Cu, Cu_2O, CuO, Fe_2O_3 and Fe_3O_4, each one of them corresponding to one of the following constraints:

$$\Delta\mu_{Cu} \leq 0\,, \tag{7.6}$$

$$2\Delta\mu_{Cu} + \Delta\mu_O \leq \Delta G^f_{Cu_2O}\,, \tag{7.7}$$

$$\Delta\mu_{Cu} + \Delta\mu_O \leq \Delta G^f_{CuO}\,, \tag{7.8}$$

$$2\Delta\mu_{Fe} + 3\Delta\mu_O \leq \Delta G^f_{Fe_2O_3}\,, \tag{7.9}$$

$$3\Delta\mu_{Fe} + 4\Delta\mu_O \leq \Delta G^f_{Fe_3O_4}\,, \tag{7.10}$$

where ΔG^f are the formation free energies of the binary Cu- or Fe-based compounds from the elementary constituents at zero temperature and zero pressure. The projection of the computed stability region of CFO into the ternary plot introduces further constraints, giving rise to the tiny region delimited by white lines in Figure 7.6.

We report in Table 7.1 the values of the surface energies of the considered terminations, computed using Eq.(7.1) and taking the chemical potentials in the center of the stability region ($\Delta\mu_{Cu} = -0.05$ eV, $\Delta\mu_{Fe} = -1.43$ eV, $\Delta\mu_O = -1.82$ eV). Given the narrowness of the stability region, the surface energies computed within are barely dependent on $\Delta\mu_i$.

Surface	Ref.	γ (meV/Å^2)
$11\bar{2}0$ - pristine	Figure 7.2(e)	50.5
$11\bar{2}0$ - V_O	Figure 7.2(b)	56.5
$11\bar{2}0$ - V_{Cu}	Figure 7.2(b)	53.9
$11\bar{2}0$ - V_{Fe}	Figure 7.2(b)	55.8
$11\bar{2}0$ - Fe/O term.	Figure 7.2(d)	89.2
$11\bar{2}0$ - Cu/O term.	Figure 7.2(c)	101.4
0001 - Fe/O term.	Figure 7.2(h)	89.0
0001 - Fe/O term. - 1/8 V_O	Figure 7.2(h)	76.7
0001 - Fe/O term. - 1/4 V_O	Figure 7.2(h)	77.1
0001 - Cu_s term.	Figure 7.2(g)	103.2
0001 - Cu term.	Figure 7.2(f)	345.5

Table 7.1

Surface energies of CFO surfaces with different termination. The chemical potentials are taken within the the stability region of the bulk CFO phase.

As it is also clear from the ternary plot in Figure 7.6, the pristine ($11\bar{2}0$) surface has the lowest surface energy when the chemical potentials satisfy the stability conditions of the bulk delafossite phase of CFO. The cost of creating a ($11\bar{2}0$) surface with single vacancies is only 4-6 meV/Å^2 higher than the cost of the pristine termination.

Our calculations suggest that the ($11\bar{2}0$) surface is energetically favored over the basal (0001). However, we are not aware of a direct experimental characterization of this surface for PEC applications, possibly due to the incompatibility with the most commonly used substrates.

7.5 Thermodynamic stability in an electrochemical environment

The phase diagram in Figure 7.6 illustrates the thermodynamics of CFO surfaces exposed to vacuum. When in contact with an aqueous electrolyte, the surfaces are modified by the interaction with water molecules, which can adsorb molecularly or dissociatively, by the interaction with dissolved charged species, which create the electric double layer, and by the possibility of electrochemical reactions taking place at the surface and leading to the formation of adsorbates or the desorption of atoms from the oxide. In particular, we are interested in the discharge of a proton with a photo-generated electron, leading the adsorption of an H atom, as an intermediate state in the HER.

Indeed, when the CBM edge is favorably aligned with respect to the redox potential of HER, the light-driven hydrogen evolution reaction can proceed through two mechanisms, namely the Volmer-Tafel or the Volmer-Heyrovsky steps, cf. Eq.(2.13), (2.14) and (2.16). Regardless of which mechanism is kinetically favored, the first step consists in the discharge of a proton at the surface of the catalyst (Volmer step), leading to the adsorption of a hydrogen atom on an active site. The adsorption of an hydrogen atom is influenced by the interaction with the adsorbates already present on the surface, giving rise to coverage-dependent adsorption free energies [213]. Therefore, the hydrogen coverage at specific electrochemical conditions depends on the thermodynamics of the Volmer step, which we evaluate via the computational hydrogen electrode (CHE) approach of Nørskov et al.[108]

We construct the surface Pourbaix diagram [111–116] of the CFO surfaces, showing the stability of different hydrogen coverage conditions as a function of the potential measured with respect to the reversible hydrogen electrode (RHE) potential $\mathrm{V_{RHE}}$. In this way, we incorporate in a compact form the dependence on the chemical potential of the protons in solution and electrons:

$$V_{\mathrm{RHE}} = V_{\mathrm{SHE}} - \frac{RT \ln 10}{e} \times \mathrm{pH} = V_{\mathrm{SHE}} + (0.059\ \mathrm{V}) \times \mathrm{pH} \quad . \tag{7.11}$$

This term represents the electrochemical potential of an electron reservoir and it will be initially treated as an independent variable, later we will consider how the band structure of CFO constrains the electrochemical potential of photogenerated electrons.

We consider both the adsorption of H atoms and the formation of oxygen vacancies. The latter are the result of two H atoms adsorbing at the same oxygen site, leading to the desorption of a water molecule. We evaluate the formation energy of various structures as a function of the number of adsorbed H atoms, N_{H^*}, the number of oxygen vacancies,

N_v, and V_{RHE}, according to:

$$\begin{aligned}\Delta G(N_{H^*}, N_v, V_{\mathrm{RHE}}) &= G_{\mathrm{slab},N_{H^*},N_v} - [G_{\mathrm{slab}} + N_{H^*}(\mu_{e^-} + \mu_{H^+}) - N_v(\mu_{H_2O} - 2(\mu_{e^-} + \mu_{H^+}))] \\ &= G_{\mathrm{slab},N_{H^*},N_v} - \left[G_{\mathrm{slab}} + (N_{H^*} + 2N_v)\frac{\mu_{H_2}}{2} - N_v\mu_{H_2O}\right] - (N_{H^*} + 2N_v)\, eV_{\mathrm{RHE}} \\ &= \Delta G^{form}_{N_{H^*},N_v} - (N_{H^*} + 2N_v)\, eV_{\mathrm{RHE}} \quad , \end{aligned} \tag{7.12}$$

where we used the fact that $\mu_{e^-} + \mu_{H^+} = 1/2\,\mu_{H_2} + eV_{\mathrm{SHE}} - RT\ln 10 \times \mathrm{pH}$, where the free energy of the H_2 molecule is evaluated at standard conditions, $T = 298.15$ K and $p = 1$ bar; moreover, $V_{\mathrm{RHE}} = V_{\mathrm{SHE}} - RT\ln 10/e \times \mathrm{pH}$. The subscripts slab and slab,N_{H^*}, N_v refer to the pristine slab and the slab with N_{H^*} adsorbed hydrogen atoms and N_v oxygen vacancies, respectively. The free energy of formation $\Delta G^{form}_{N_{H^*},N_v}$ is computed as:

$$\Delta G^{form}_{N_{H^*},N_v} = \Delta E^{form}_{N_{H^*},N_v} + \Delta E_{\mathrm{ZPE}} - T\Delta S \quad , \tag{7.13}$$

where $T\Delta S$ and ΔE_{ZPE} are the energy changes due to entropic and zero-point effects and $\Delta E^{form}_{N_{H^*},N_v}$ is the DFT formation energy.

In the construction of the diagram for the (0001) surface with the Fe/O termination we employed the supercell whose top view is reported in Figure 7.7(a). The 16 outermost oxygen atoms are the only active sites for hydrogen adsorption and we passivated both the terminations of the slab with the same number of hydrogen atoms to avoid the formation of dipoles within the cell. The list of the adsorption reactions considered in the construction of the surface Pourbaix diagram and the corresponding free energies are reported in Table 7.2.

The initial state corresponds to the pristine surface, indicated as $\star$, plus a certain number of hydrogen atoms, taken from a gaseous reservoir of H_2 molecules at 298.15 K and 1 bar. The number of hydrogen atoms added on top of the surface is indicated in Table 7.2 as a coverage related to the total number of surface oxygen sites of the pristine surface. For instance, $\star + 0.5$ ML H indicates that the number of hydrogen atoms added on top of the pristine surface is half the number of oxygen sites.

The hydrogen atoms are then adsorbed on the surface giving rise to the final state. The coverage values are also referred to the total number of oxygen sites on the pristine surface and, wherever not explicitly indicated, H^* refers to the absorption of a hydrogen atom on an oxygen site. For instance, 0.5 ML of H^* refers to the configuration in which half of the active sites have one H adsorbed. We first considered the case of 0, 1/4, 1/2, 3/4 and 1 ML of H^* coverage and then we employed the possibility of further adding hydrogen atoms, creating oxygen vacancies on the surface and adsorption on the hollow sites.

The free energy difference of each reaction is computed using Eq.(7.13), calculating

separately the three contributions. ΔE represents the difference of the DFT total energies between the initial and the final state. The free energy of each hydrogen atom is half the free energy of a H_2 molecules at 298.15 K and 1 bar. The entropic and zero point contributions of gaseous H_2 and H_2O were taken from the thermochemical tables [104], assuming equilibrium between liquid water at 298.15 K and gaseous water at 0.035 bar [108].

We calculated the zero-point energy of adsorbed species computing the vibrational frequencies with the finite differences method. In particular, the zero-point energy associated with the H-O bond corresponds 0.30 eV, while it is 0.23 eV for the adsorption on a hollow site.

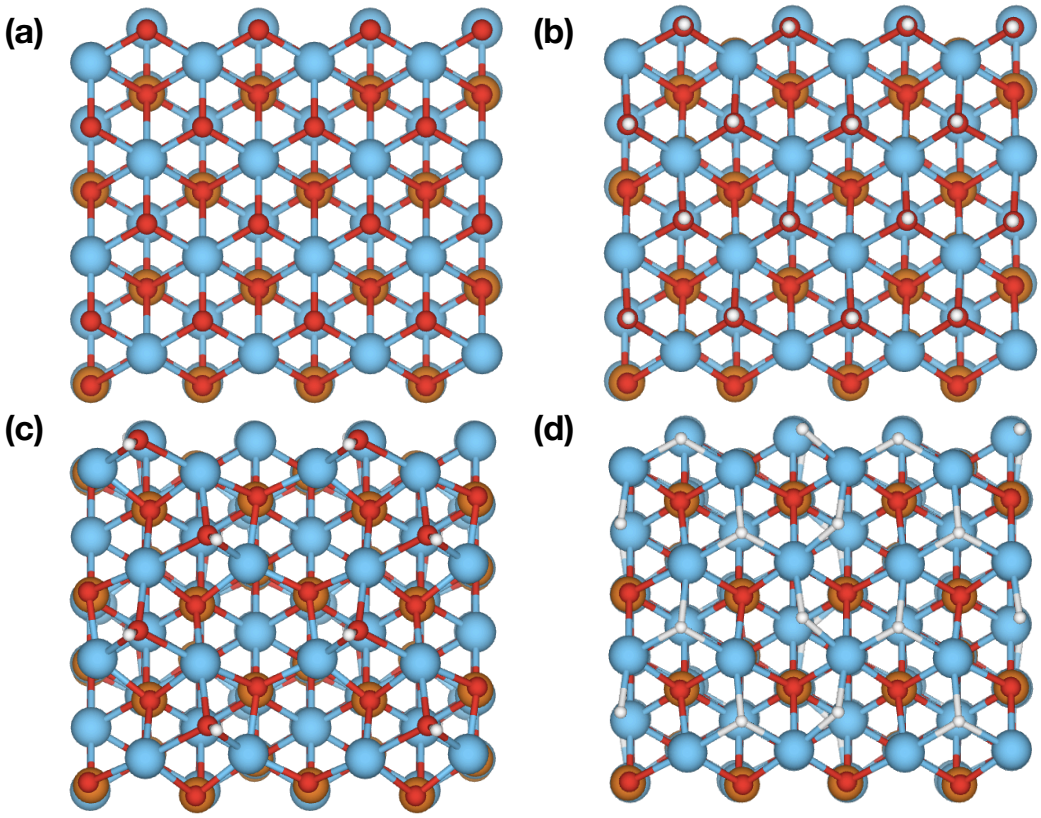

Figure 7.7

Top view of four different adsorption states employed in the construction of the surface Pourbaix diagram for the (0001) surface. Pristine surface (a), 1 ML H^* (b), 0.5 ML H^* + 0.5 ML V_O (c), 0 ML H^* + 1 ML V_O + 1 ML $H\star_{\text{hollow}}$ (d). Red, blue, orange and white represent oxygen, iron, copper and hydrogen atoms, respectively.

.

	Initial state	Final state	ΔE(eV) per cell	ΔZPE(eV) per cell	TΔS(eV) per cell	$\Delta G^{form}_{N_{H^*},N_v}$(eV) per cell	per H
r0	$\star$	$\star$	0	0	0	0	0
r1	$\star$ + 0.25 ML H	0.25 ML H*	-15.96	1.32	-1.62	-13.02	-1.63
r2	$\star$ + 0.50 ML H	0.50 ML H*	-28.36	2.64	-3.23	-22.49	-1.41
r3	$\star$ + 0.75 ML H	0.75 ML H*	-35.61	3.96	-4.85	-26.80	-1.12
r4	$\star$ + 1 ML H	1 ML H*	-42.01	5.28	-6.46	-30.27	-0.95
r5	$\star$ + 17/16 ML H	15/16 ML H* + 1/16 ML V_O + 1/16 ML H_2O	-41.36	5.53	-5.52	-30.30	-0.89
r6	$\star$ + 1.5 ML H	0.5 ML H* + 0.5 ML V_O + 0.5 ML H_2O	-40.12	7.28	1.03	-33.88	-0.71
r7	$\star$ + 2 ML H	0 ML H* + 1 ML V_O + 1 ML H_2O	-19.23	9.28	8.53	-18.48	-0.29
r8	$\star$ + 2 ML H	0.5 ML H* + 0.5 ML V_O + 0.5 ML H_2O + 0.5 ML H$\star_{\text{hollow}}$	-32.90	8.64	-2.20	-22.10	-0.35
r9	$\star$ + 2.5 ML H	0 ML H* + 1 ML V_O + 1 ML H_2O + 0.5 ML H$\star_{\text{hollow}}$	-28.26	10.64	5.30	-22.91	-0.29
r10	$\star$ + 3 ML H	0 ML H* + 1 ML V_O + 1 ML H_2O + 1 ML H$\star_{\text{hollow}}$	-17.43	12.00	2.06	-7.50	-0.08

Table 7.2

List of adsorption reactions employed to construct the surface Pourbaix diagram of the CFO(0001) surface. For each reaction, the ΔG is computed according to Eq.(7.13). Each coverage value is related to the total number of active sites per surface.

We considered the following reactions:

- r0 represents the reference state, in which the pristine surface does not adsorb hydrogen atoms and the ΔG is obviously 0.

- r1-r4 represent the adsorption of one hydrogen atom on O sites up to the full coverage, whose structure is reported in Figure 7.7(b).

- r5 represents the reaction in which an extra hydrogen atom is added on top of the surface with full H^* coverage, forming a water molecule with a surface hydroxyl. The water molecule desorbs from the slab, forming an oxygen vacancy on the surface. Whenever a molecule of water is desorbed, we assume that it migrates into a reservoir of gaseous water at room temperature and pressure 0.035 bar.

- In r6 we extended the condition of r5 to half of the surface oxygen atoms, as shown in Figure 7.7(c).

- r7 and r8 represent two different final states, starting from the same initial state, in which the number of hydrogen atoms is twice the number of oxygen active sites. In r7 all the oxygen sites at the surface accommodate two hydrogen atoms, desorbing from the slab as water molecules. In r8 half of the oxygen atoms at the surface desorbs from the slab, but the remaining hydrogen atoms, instead of forming other water molecules with the surface hydroxyls, occupy the hollow positions of the missing oxygen atom, in the center of the triangle formed by the three undercoordinated Fe ions, as shown in Figure 7.7(c). We found this configuration more stable than the configuration with the extra hydrogen on top of one Fe atom or in a bridging position between two atoms.

- r9 and r10 represent the limit situations in which, upon the adsorption of hydrogen atoms, all the oxygen in the external layer are desorbed from the surface and further H atoms occupy hollow sites, with a coverage of 0.5 ML H_{hollow} (r9) or 1 ML $_{\text{hollow}}$ (r10), as shown in Figure 7.7(d).

The lateral interaction between the adsorbates is not negligible, since the free energy per hydrogen atom goes from -1.63 eV at low-coverage conditions to -0.95 eV at full coverage. When oxygen vacancies begin to form on the surface, the entropic contribution of desorbed water molecules becomes significant. Nevertheless, the ΔE contribution makes the free energy of r8 lower than r7 and thus the formation of hollow H^* more convenient than the formation of further water molecules.

However, the values of ΔG reported in Table 7.2 do not take into account the electrochemical conditions, which are included into the V_{RHE} term in Eq.(7.12). In order to determine the most stable adsorption state, we plot in Figure 7.8 the ΔG of each reaction as a function of the V_{RHE} potential, according to Eq.(7.12). For each point,

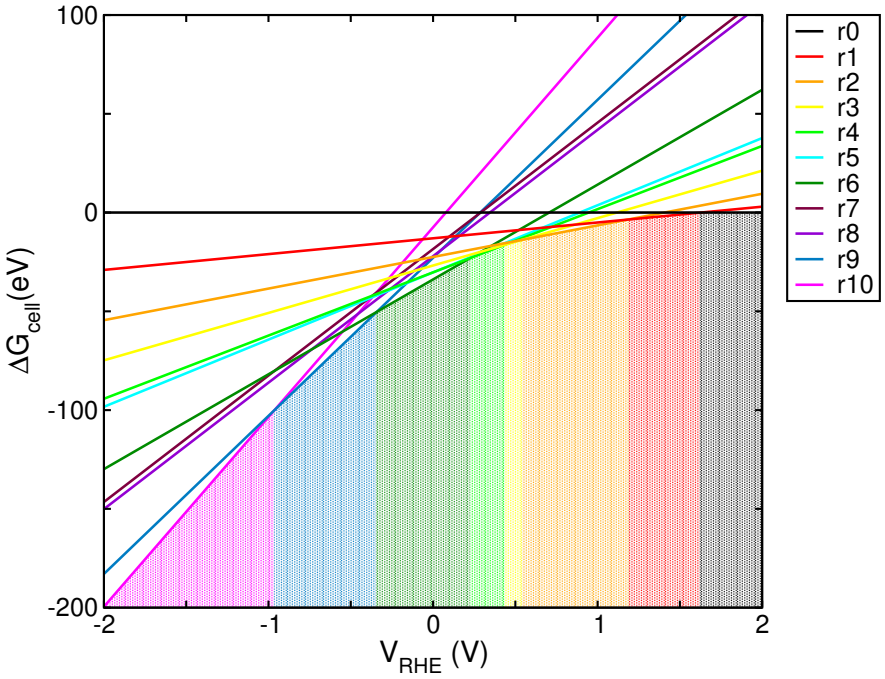

Figure 7.8

ΔG of the reactions listed in Table 7.2 as a function of the RHE potential V_{RHE} of the electrons. The colored areas indicate the reaction with the lowest ΔG for each value of V_{RHE}

.

the final state of the reaction with the lowest ΔG represents the most favorable adsorption state for that specific electrochemical conditions, generating the surface Pourbaix diagram.

In a similar fashion, we constructed the surface Pourbaix diagram for the $(11\bar{2}0)$ surface, using the reaction written in Table 7.3. The pristine $(11\bar{2}0)$ surface exposes undercoordinated Fe and O atoms that may host the hydrogen adsorption. However, the binding energy is extremely different in the two cases. While hydrogen atoms are strongly bound when adsorbed to the oxygen sites, -1.25 eV, the adsorption on Fe sites is highly unfavored, 0.78 eV. For this reason, we investigated the relative stability of adsorption on oxygen atoms only, with coverage of 0 ML, 1/3 ML, 1/2 ML, 2/3 ML and 1 ML H^*. In analogy with the (0001) termination, we investigated the formation of oxygen vacancies at the surface after the complete hydrogenation of the oxygen sites.

- r0 represents the reference state, in which the pristine surface does not adsorb hydrogen atoms and the ΔG is obviously 0.

- r1-r4 represent the adsorption of one hydrogen atom on O sites until the full coverage, whose geometry is reported in Figure 7.9(a).

- r5 represents the reaction in which an extra hydrogen atom is added on top of the surface, forming a water molecule with a surface hydroxyl. The water molecules desorbs from the slab and leaves the system with an oxygen vacancy and with undercoordinated Cu and Fe atoms on the surface. Moreover, during the geometry relaxation an oxygen from the subsurface layer moves towards the surface, as shown in Figure 7.9(b).

- In r6 an extra hydrogen atom is adsorbed in a bridging position between the undercoordinated Cu and Fe. This configuration was the most stable among those in which one hydrogen atom is adsorbed close to the oxygen vacancy. In particular, we investigated the adsorption on top of the undercoordinated cations and the subsurface oxygen.

- r7 represents the configuration in which, starting from the structure determined in r6, an hydrogen atom is adsorbed on the subsurface oxygen atom which migrated towards the surface.

- In r8-r9 additional oxygen vacancies are created on the surface, with densities of 1/4 and 1/2 ML. This last geometry is shown in Figure 7.9(c).

- r10-r12 represent three different ways to add 0.5 ML of hydrogen atoms on top of the surface with 1/2 ML of oxygen vacancies. In r10, they form water molecules with the hydroxyl groups already present on the surface and desorb from the slab and leaving the system with 1 ML of oxygen vacancies. In r11, they are adsorbed in the bridging Cu-Fe positions, close to the oxygen vacancies, while in r12 the adsorption sites are half the subsurface oxygen atoms which were pushed towards the surface.

- In r13 all the subsurface oxygen atoms of the surface with 0.5 ML of oxygen vacancies are passivated with hydrogen atoms, as shown in Figure 7.9(d).

- Finally, in r14, we added 0.5 ML of H to the structure defined by r13, assuming that they form water molecules with the hydroxyl groups initially belonging to the surface layer, thus forming further oxygen vacancies.

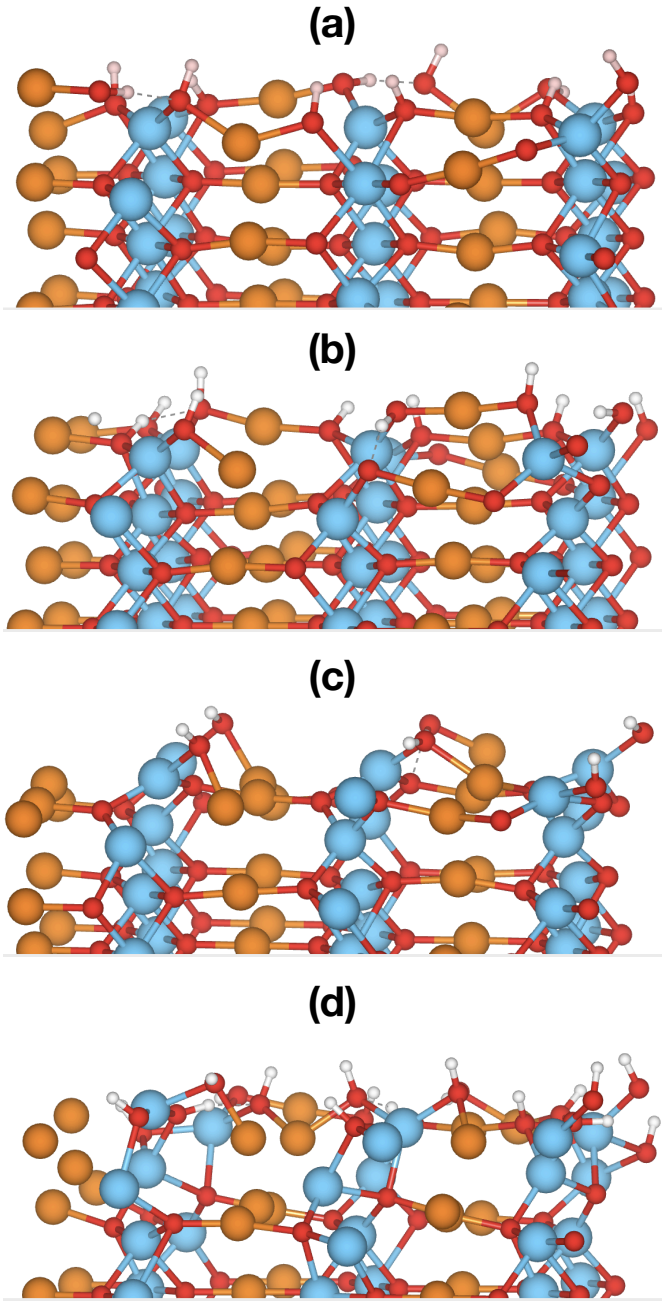

Figure 7.9

Side view of four different adsorption states employed in the construction of the surface Pourbaix diagram for the $(11\bar{2}0)$ surface. 1 ML H* (a), 11/12 ML H* + 1/12 ML V_O (b), 0.5 ML H* + 0.5 ML V_O (c), 1.5 ML H* + 0.5 ML V_O (d). Red, blue, orange and white spheres represent oxygen, iron, copper and hydrogen atoms, respectively.

.

	Initial state	Final state	ΔE(eV) per cell	ΔZPE(eV) per cell	TΔS(eV) per cell	$\Delta G^{form}_{N_{H^*},N_v}$(eV) per cell	per H
r0	$\star$	$\star$	0	0	0	0	0
r1	$\star$ + 1/3 ML H	1/3 ML H*	-9.91	1.32	-1.62	-6.97	-0.87
r2	$\star$ + 1/2 ML H	1/2 ML H*	-14.83	1.98	-2.42	-10.43	-0.87
r3	$\star$ + 2/3 ML H	2/3 ML H*	-16.20	2.64	-3.23	-10.33	-0.65
r4	$\star$ + 1 ML H	1 ML H*	-20.22	3.96	-4.85	-11.41	-0.48
r5	$\star$ + 13/12 ML H	11/12 ML H* + 1/12 ML V_O + 1/12 ML H_2O	-18.67	4.21	-3.99	-10.46	-0.40
r6	$\star$ + 14/12 ML H	11/12 ML H* + 1/12 ML V_O + 1/12 ML H_2O 1/12 ML H$\star_{\text{bridge}}$	-19.77	4.38	-4.31	-11.08	-0.40
r7	$\star$ + 15/12 ML H	1 ML H* + 1/12 ML V_O + 1/12 ML H_2O 1/12 ML H$\star_{\text{bridge}}$	-20.32	4.71	-4.72	-10.89	-0.36
r8	$\star$ + 15/12 ML H	9/12 ML H* + 3/12 ML V_O + 3/12 ML H_2O	-16.22	4.71	-2.04	-9.48	-0.32
r9	$\star$ + 1.5 ML H	1/2 ML H* + 1/2 ML V_O + 1/2 ML H_2O	-12.66	5.46	0.77	-7.97	-0.22
r10	$\star$ + 2 ML H	0 ML H* + 1 ML V_O + 1 ML H_2O	-4.98	6.96	6.39	-4.41	-0.09
r11	$\star$ + 2 ML H	1/2 ML H* + 1/2 ML V_O + 1/2 ML H_2O 1/2 ML H$\star_{\text{bridge}}$	-13.95	6.48	-1.65	-5.82	-0.12
r12	$\star$ + 2 ML H	1 ML H* + 1/2 ML V_O + 1/2 ML H_2O	-19.10	7.44	-1.65	-10.02	-0.20
r13	$\star$ + 2.5 ML H	3/2 ML H* + 1/2 ML V_O + 1/2 ML H_2O	-24.97	9.42	-4.07	-11.48	-0.18
r14	$\star$ + 3 ML H	1 ML H* + 1 ML V_O + 1 ML H_2O	-11.62	10.92	-1.55	-2.25	-0.03

Table 7.3

List of adsorption reactions employed to construct the surface Pourbaix diagram of the CFO($11\bar{2}0$) surface. For each reaction, the ΔG is computed according to Eq.(7.13).

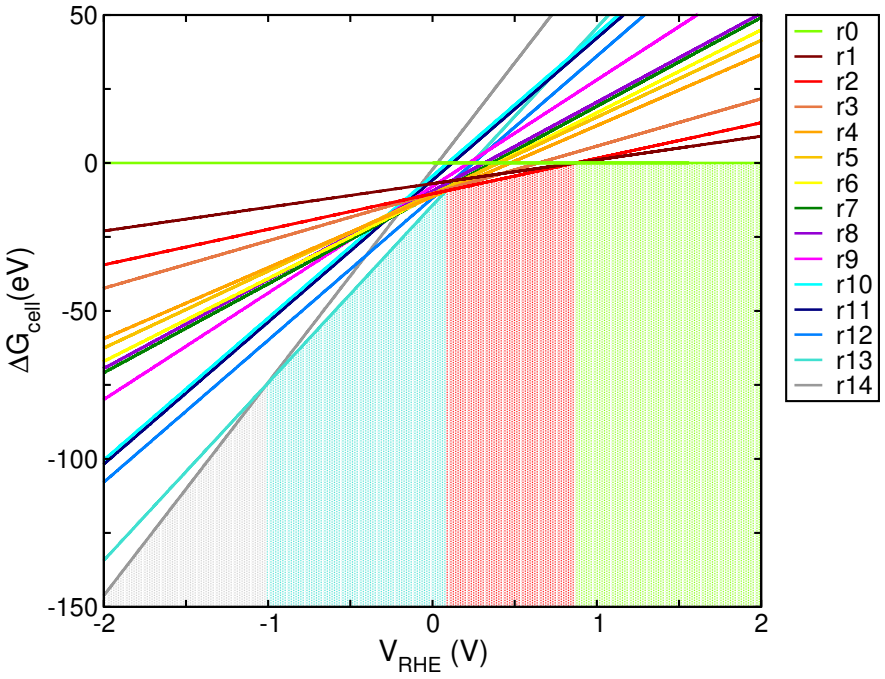

Figure 7.10

ΔG of the reactions listed in Table 7.3 as a function of the RHE potential V_{RHE} of the electrons. The colored areas indicate the reaction with the lowest ΔG for each value of V_{RHE}

.

As it was previously done for the (0001) surface, we report in Figure 7.10 the ΔG of the reactions listed in Table 7.3 as a function of V_{RHE}.

The surface Pourbaix diagrams of the (0001) and the $(11\bar{2}0)$ surfaces are shown in Figure 7.11. When the coverage of the H* on the (0001) surface is less than 0.5 ML, the hydrogen atoms supply the missing charge due to the Cu-deficiency of the slab, saturating all the holes for $\theta = 0.5$ ML. Further hydrogen atoms added on the surface reduce Fe^{3+} ions on the outermost layer into Fe^{2+}. The threshold at which the reduction processes begin to take place is 0.54 V versus RHE, corresponding to the transition between 0.5 ML H* and 0.75 ML H*. This value compares favorably with a recent measurement in which a polaronic Fe^{3+}/Fe^{2+} charge transition level has been observed at 0.7 V versus RHE, inducing Fermi level pinning and limiting the performance of CFO as a photocathode [12]. The presence of a state inducing Fermi level pinning at this potential was previously reported and attributed to the formation of a surface metal hydroxide [11].

We then considered the possibility of further increasing the number of hydrogen atoms added into the system, allowing the adsorption of two hydrogen atoms on the

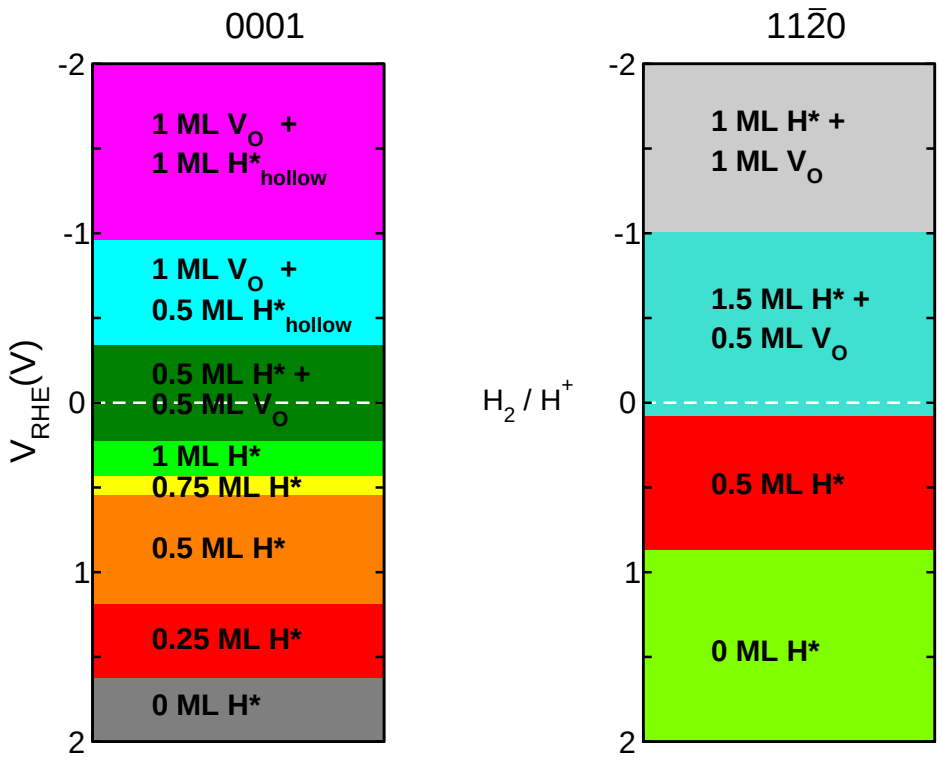

Figure 7.11

Surface Pourbaix diagram of the CFO(0001) (left) and CFO(11$\bar{2}$0) (right) surfaces, showing the potential-dependent surface coverage.

same oxygen site. In this case, a water molecule forms at the active site and desorbs from the surface leaving one oxygen vacancies on the slab. In principle, the creation of oxygen vacancies could be possible also before the full H* coverage, since the interaction between the OH groups could make the absorption of a second hydrogen more favorable on the hydroxyl top site than on another oxygen on the surface. [214] However, in this situation, the second hydrogen atom spontaneously moves towards an empty oxygen site, rather than creating a water molecule and desorbing from the surface.

We investigated different coverages of oxygen vacancies, ranging from a single vacancy in a large supercell to the full oxygen depletion in the outermost layer. Moreover, additional hydrogen atoms can be adsorbed on the hollow sites formed by oxygen vacancies, with a bond length of ~ 2 Å with the three surrounding Fe ions. This configuration is more favorable than the absorption on top of undercoordinated Fe sites or in a bridging position between two sites.

When a hydrogen atom is nearby a surface already containing oxygen vacancies, there is a competition between the creation of a new vacancy or the adsorption on a hollow site. In the former case, the entropic contribution of desorbed water molecule becomes significant in the Gibbs free energy, while the latter entails a gain in the enthalpic term. The upper part of the Pourbaix diagram reveals that a high density of oxygen vacancies, from 0.5 to 1 ML, is expected on the surface for negative values of V_{RHE}, while the adsorption of hydrogen atoms on hollow sites is thermodynamically stable for V_{RHE} more negative than -0.34 V. In contrast with the adsorption of the H^* on the oxygen sites, in which the thermodynamically stable structures show an increasing coverage, there is a net transition between the configuration with 0.5 ML H^* + 0.5 ML V_O (dark green) and that with 1 ML V_O + 0.5 ML H^*_{hollow} (cyan).

Only four phases are thermodynamically stable in the surface Pourbaix diagram of CFO($11\bar{2}0$). First, the pristine surface is the most stable configuration for V_{RHE} more positive than 0.87 V. The surface with 0.5 ML H^* occupies the portion between 0.87 V and 0 V. Among the different ways to adsorb on half of the oxygen sites, the configuration with the lowest energy is the one with an alternate arrangement, in such a way that the hydroxyls have the maximum possible distance among them, hence the lowest repulsion. At half coverage conditions, the Fe ions in the outermost layer are completely reduced to Fe^{2+}.

For negative values of V_{RHE}, the thermodynamically stable phases contain oxygen vacancies. When a single oxygen vacancy is created, one subsurface oxygen atom breaks a O-Fe bond and migrates towards the surface. A second hydrogen atom could now be adsorbed either on this oxygen site or in a bridging position between the undercoordinated cations. Alternatively, it can create a second oxygen vacancy, being adsorbed on another hydroxyl group. According to the free energies reported in Table 7.3, the adsorption in a bridging site between undercoordinated Cu and Fe ions is favored for a low density of oxygen vacancies, in which there is a negligible interaction among them. However, this configuration is not a thermodynamically stable phase in the Pourbaix diagram.

Indeed, the most stable surface between 0 and -1 V, shown in Figure 7.9(d) and corresponding to the turquoise area in Figure 7.11, has a higher density (0.5 ML) of oxygen vacancies on the surface. In this configuration, the cations on the surface move towards the second layer, forming a single, Cu- and Fe-rich layer, in which the subsurface oxygen atoms are now exposed to the vacuum and host the hydrogen adsorption. For such a significant density, the adsorption on bridging sites is no longer energetically relevant. Above 1 V, an additional 0.5 ML of hydrogen atoms are adsorbed on the

hydroxyl groups formed by the oxygen sites which were originally present on the surface, forming water molecules which desorb from the surface.

The Pourbaix diagrams in Figure 7.11 describe the coverage of the adsorbates depending on V_{RHE}, which was treated as an independent variable between -2 and 2 V. However, in order to study the properties of the semiconducting electrode under operating conditions, V_{RHE} must be set to the appropriate value, corresponding to the chemical potential of the electron reservoir, the Fermi level in dark conditions and the electron quasi-Fermi level under illumination.

7.6 Band alignment in dark conditions

When the electrode is not illuminated (dark conditions) and under flatband conditions, the Fermi level of the semiconductor corresponds to the flatband potential, which is approximately equal to 1 V for CFO [7]. Under this potential, the most stable phases in the Pourbaix diagram are the pristine $(11\bar{2}0)$ and the surface with 0.5 ML H^* for the (0001), which are those with all the atoms in the same charge state as in the bulk, consistently with the fact that in dark conditions no reduction processes occur on the surface.

A favorable alignment of the CBM edge with the redox potentials of water is a key thermodynamic requirement to enable the light-driven HER. We calculated the alignment of the energy levels in the absence of illumination, interfacing with the water the most stable structures in the Pourbaix diagram at the potential corresponding to the flatland potential.

Among the different methods proposed to predict the band alignment from *ab-initio* calculations [117–123], we follow herein the approach of Guo et al. [123], which consists in three independent steps, as it was also reported in earlier studies [118, 120, 121]. As described in Sect.4.4, an accurate description of the band edges of the bulk material is required, in order to align them to the average electrostatic potential in the unit cell. We have reported in Chapter 5 that the hybrid PBE0 functional provides the best description of the electronic structure of bulk CFO, when the fraction of exact exchange is properly set up. We replicated these calculations with the `CP2K` code, using a hexagonal $4 \times 4 \times 1$ supercell, containing 192 atoms, sampling the BZ only at the Γ point. We found that, for a fraction of exact exchange equal to 0.20, the valence band maximum (VBM) and the conduction band minimum (CBM) of CFO lie 5.25 eV

and 6.71 eV above the average electrostatic potential, with a band gap in line with the experimental values. Second, we adopted the values reported by Ambrosio et al. for the alignment between the SHE with the average electrostatic potential of water, when this specific computational setup is used [125]. In particular, the vacuum level lies 3.69 eV higher in energy than the average electrostatic potential of water, and the SHE 4.56 eV below the vacuum level [125], Finally, the electrostatic potential difference across the CFO/water interface, which depends on the specific surface termination considered, must be computed through the analysis of several snapshots of AIMD simulations.

7.6.1 Band alignment of the (0001) surface

As reported in the previous section, when the CFO(0001) surface is put in contact with an electrolyte and, in dark conditions, the Fermi level coincides with the flatband potential, the thermodynamically favorable coverage is the one with 0.5 ML of H^* adsorbed on the oxygen sites, in which all the atoms are in the same charge state as in the bulk. However, we have shown that the same charge state can be obtained, in vacuum, by creating oxygen vacancies with a density equal to 1/4 of the total surface oxygen. The two configurations give the same results even in presence of few water molecules on top of them. On the one hand, the surface with half H^* coverage has no undercoordinated metal binding site and therefore the interaction with water occurs mainly via hydrogen bonding, as in the O_3-Fe-Fe- termination of the (0001) surface of hematite [215]. On the other hand, in the defective surface, the oxygen vacancy leaves three undercoordinated Fe atoms that could act as active sites for water adsorption or dissociation. We have added three water molecules nearby the three undercoordinated Fe atoms, which could be adsorbed molecularly or dissociatively, and we perform a static geometry optimization. However, in both cases, during the relaxation the system moves spontaneously into the configuration in which one water molecule dissociates and the OH group takes the place of the missing oxygen, while the hydrogen is adsorbed on one oxygen site of the slab, in the same configuration as the surface with 0.5 ML H^* coverage.

We performed the AIMD simulation interfacing this latter configuration with 15 Å thick slab of water. The side view of the interface is reported in the top panel of Figure 7.12. During the AIMD the first two O-Fe-O layers and the first Cu layer are fixed, while the others, closer to the interface with water, are allowed to move.

In the middle panel of Figure 7.12, we show the average density distribution of water molecules as a function of the position z in the direction perpendicular to the surface.

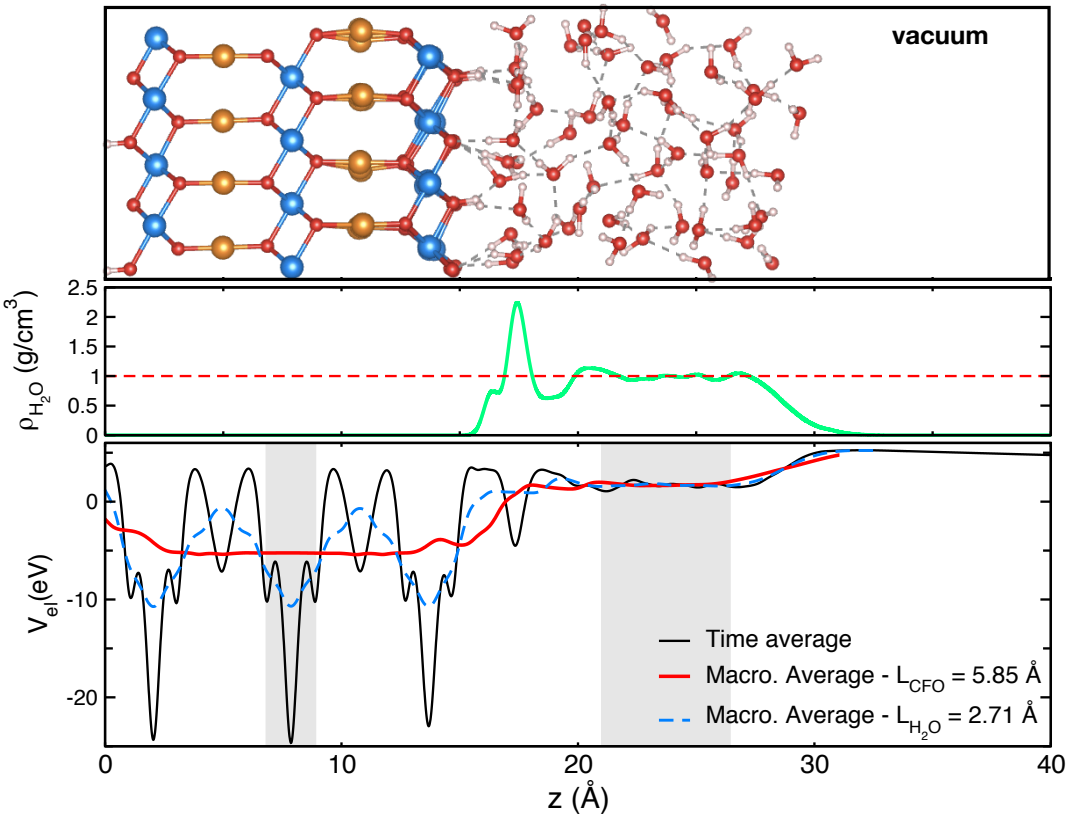

Figure 7.12

Interface between the (0001) surface and water (top panel), water density profile (middle panel) and electrostatic potential across the interface (bottom panel). The grey areas indicate the regions from which we extracted the average electrostatic potential of CFO and water.

Two different regions are easily distinguished: a first peak, corresponding to a layer of water molecules accumulated close to the CFO surface and a bulk-like region, in which the density of water oscillates around 1 g/cm^3. In hydroxylated surfaces in contact with water, the formation of an interfacial layer with higher density than bulk water has been observed. [216–218] In this interfacial layer, whose thickness is $\sim$ 3 Å, the water molecules form an interplay of hydrogen bonds with the undercoordinated oxygen atoms of the substrate and among themselves.

In order to examine the orientation of the water molecules during the AIMD simulations, we analyzed the distribution of the angle between the dipole of each molecule and the z axis. When the angle is 90°, the dipole and the H-O-H plane lie perpendicular to the z axis, while when the angle is 0° (180°), the dipole is parallel (antiparallel) to the z axis, with the hydrogen atoms of the molecules pointing towards (outside) the surface.

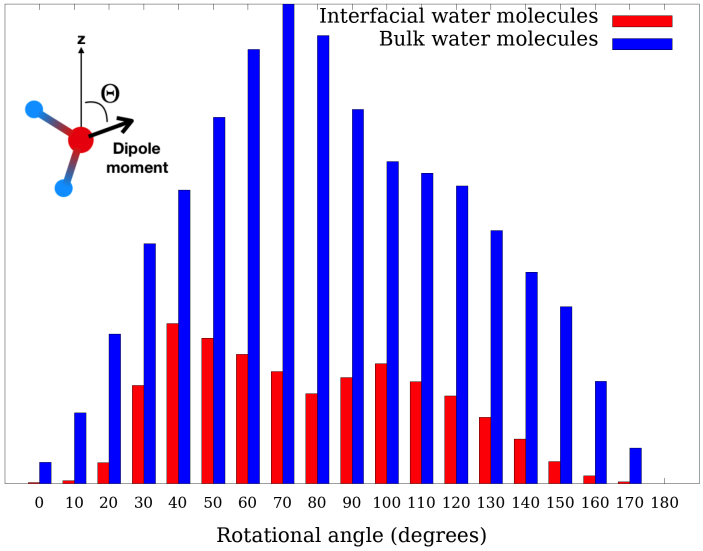

Figure 7.13

Histogram of the distribution of the angle between the dipole moment of water molecules and the z axis (see inset) for the interfacial (red) and bulk (blue) water molecules, computed from the molecular dynamics simulation of the CFO(0001) interfaced with water.

We analyzed the orientation of the molecules every 10 fs after the equilibration time and we constructed the histograms reported in Figure Figure 7.13 using bins of 10°.

According to the distance from the surface, we separated the contributions of the bulk-like water molecules from the interfacial ones, the latter being those within the first density peak. The main peak of the interfacial molecules occurs for 40°, corresponding to water molecules whose hydrogen atoms point towards the surface, to form hydrogen bonds with the undercoordinated oxygen atoms at the surface. The histogram of the interfacial and the bulk water molecules is almost symmetric around 90°, which means that, on average, for each molecule there is another one that brings an opposite dipole moment.

The time average of the electrostatic potential profile is shown in the bottom panel of Figure 7.12. Each point along the z direction, perpendicular to the interface, represents the planar average in the corresponding xy plane. We performed a macroscopic average of the potential profile to compute the potential drop at the CFO-water interface [219, 220]. The macroscopic average was computed with two different periods to reduce the oscillations in the CFO or in the water side of the interface. The red curve in Figure 7.12 represents the macroscopic average in which the period, 5.85 Å, corresponds to the periodicity of the CFO slab in the z direction. The period of the blue dashed line,

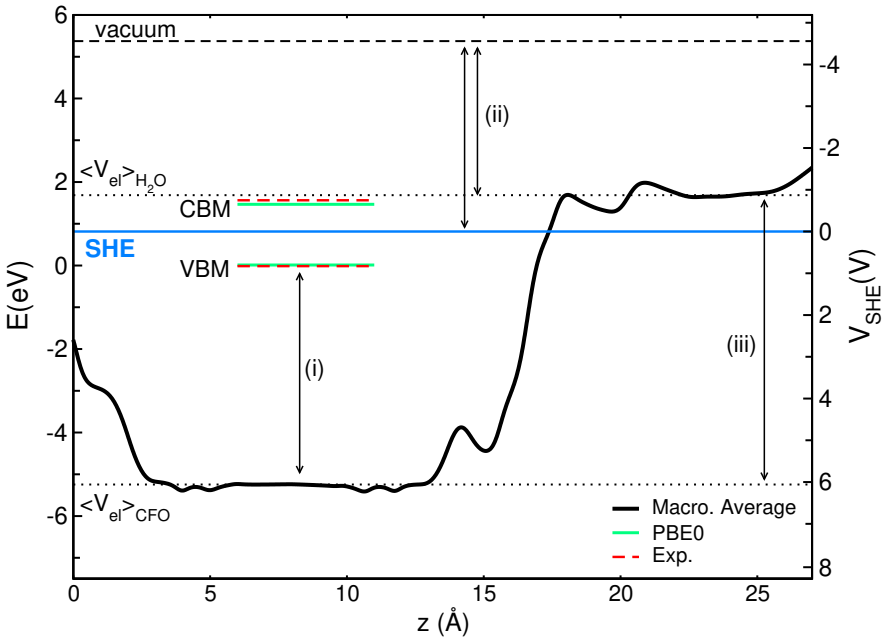

Figure 7.14

Band edges alignment of CFO w.r.t. the SHE, when the (0001) surface is interfaced with liquid water. The band edges at point (i) are those of the bulk delafossite phase of CFO, computed at the PBE0 level. The position of the vacuum and the SHE level w.r.t. the average electrostatic potential of water (ii) were taken from the literature [218], while the alignment of the electrostatic potentials (iii) was computed via an AIMD simulation.

2.71 Å, corresponds to the peak of the O-O radial distribution function of bulk water. We computed the potential drop across the interface as the difference between the average of the red curve in the center of the slab and the average of the blue one in the bulk-like region of water, as indicated by the grey areas in Figure 7.12. In Figure 7.14 we report the alignment procedure, in which the difference between the electrostatic potentials (iii), equal to 6.92 eV, is combined with the bulk PBE0 band edges (i) and the computational SHE (ii). It's worth noticing that, although the band edges of CFO were computed with the hybrid PBE0 functional, we performed the AIMD simulation with the PBE+U approach, since it has been shown that the electrostatic alignment is weakly dependent on the employed functional, with discrepancies of the order of 0.01 eV. [123]

To make a direct comparison with the experimental data, we should keep in mind that the AIMD simulations are equivalent to experiments performed at the pH corresponding to the point of zero charge (PZC). According to the PEC measurements of Prévot et al. [7], performed in alkaline conditions at pH = 13.6, the VBM and the CBM of CFO, at

flatband conditions, lie −0.32 V and +1.26 V versus the reversible hydrogen electrode (RHE), respectively. These values are easily referred to the SHE using Eq.(7.11) and then shifted to the PZC, assuming that the bands have a Nernstian dependence on the pH [5, 126]:

$$V_{\mathrm{SHE}}(\mathrm{pH_{PZC}}) = V_{\mathrm{SHE}}(\mathrm{pH}) - (0.059\ \mathrm{V}) \times (\mathrm{pH_{PZC}} - \mathrm{pH}) \quad . \tag{7.14}$$

The PZC of CFO corresponds to a pH of 7.36 [59] and the resulting band edges, depicted with the red dashed lines in Figure, lie −0.75 V and +0.83 V versus the SHE. Our predicted values for the CBM and VBM are -0.65 ± 0.02 V and $+0.82 \pm 0.02$ V versus SHE, in excellent agreement with the experiments.

The uncertainty we reported above for the calculated band edges is directly related to the statistical error in the alignment of the electrostatic potential in the bulk region of CFO with respect to the bulk region of water. For each snapshot, we computed this alignment as the difference between the macroscopic averages in the center of the CFO slab and inside the bulk-region of water. We then computed the statistical error of the set of these data as $\epsilon = \sigma/\sqrt{N}$, where σ is the standard deviation and N the number of data in the set, obtaining $\epsilon = 0.02$ eV. Within this uncertainty, the VBM is in excellent agreement with the experimental value, while the position of the CBM is slightly underestimated. This is due to the fact that with our description of the electronic structure of the system (PBE0 with a fraction of exact exchange equal to 0.20) the gap is slightly underestimated.

7.6.2 Band alignment of the $(11\bar{2}0)$ surface

The pristine surface is the thermodynamically stable phase of the $(11\bar{2}0)$ termination of CFO in an electrolyte in dark conditions under flatband potential. The surface exposes active sites that could be highly reactive in contact with water. In particular, the two-fold undercoordinated Fe atoms could act as active sites to adsorb up to two water molecules, either molecularly or dissociatively, with an exposed oxygen atom acting as proton acceptor. We investigated the most energetically favorable adsorption state in static conditions in vacuum, by evaluating the adsorption energy of water molecules on a single Fe site and for full coverage as:

$$E_{ads} = \frac{1}{N_{\mathrm{H_2O}}} \left[E_{\mathrm{slab}+N_{\mathrm{H_2O}}} - (E_{\mathrm{slab}} + N_{\mathrm{H_2O}} E_{\mathrm{H_2O}}) \right] \quad , \tag{7.15}$$

where $E_{\mathrm{slab}+N_{\mathrm{H_2O}}}$ is the energy of the slab with $N_{\mathrm{H_2O}}$ adsorbed water molecules, E_{slab} is the energy of the pristine slab and $E_{\mathrm{H_2O}}$ the energy an isolated water molecule. The

Configuration		E_{ads} (eV)		
Water molecules per Fe site	Adsorption	Single site	Two sites	Full coverage
1	Molecular	−0.56	−0.54	−0.55
1	Dissociative	−0.86	−0.81	−0.77
2	Molecular	−0.71	−0.73	−0.77
2	Dissociative	−0.64	−0.60	−0.59
2	Mixed	−0.67	−0.71	−0.77

Table 7.4

Adsorption energies of a single and two water molecules on the CFO pristine $(11\bar{2}0)$ surface.

adsorption energies for water molecules adsorbed on a different number of sites are reported in Table 7.4.

We found that the dissociative adsorption is energetically favored for a single water molecule per Fe site, with an average adsorption energy $0.2 - 0.3$ eV lower than the molecular adsorption, depending on the coverage. The bond length between the molecularly adsorbed water and the Fe site is 2.2 Å, compatible with the chemisorption range, while in the dissociative case the distance between the Fe ion and the hydroxyl group is 1.9 Å. The fact that the dissociative adsorption of water is energetically favored on Fe^{3+} sites and the bond lengths between the sites and the adsorbates is in line with what has been reported for hematite [215].

When two water molecules are added on the system, it is energetically favorable for them to dissociate at two different sites rather than being adsorbed simultaneously on the same site. However, when the number of water molecules exceeds the number of Fe sites, the dissociative adsorption of two water molecules on the same site becomes energetically unfavorable and the molecules are adsorbed either both molecularly or in a mixed way, one molecularly and one dissociatively, with a very similar adsorption energy. In the mixed case, which has been reported also for the $(11\bar{2}0)$ surface of cobalt oxides [221], the hydroxyl groups and the water molecules are connected through a network of hydrogen bonds, reported in Figure 7.15(c), while the slab with two adsorbed water molecules is shown in Figure 7.15(d). The adsorption of the second water molecule on each Fe atom is energetically and geometrically convenient, in order to achieve an octahedral ligand shell that resembles the bulk-like structure.

The adsorption mechanism could alter significantly the electrostatic potential alignment across the AIMD simulation [218]. We created two different interface models: one in which one layer of molecularly adsorbed water molecules is added by hand on top of

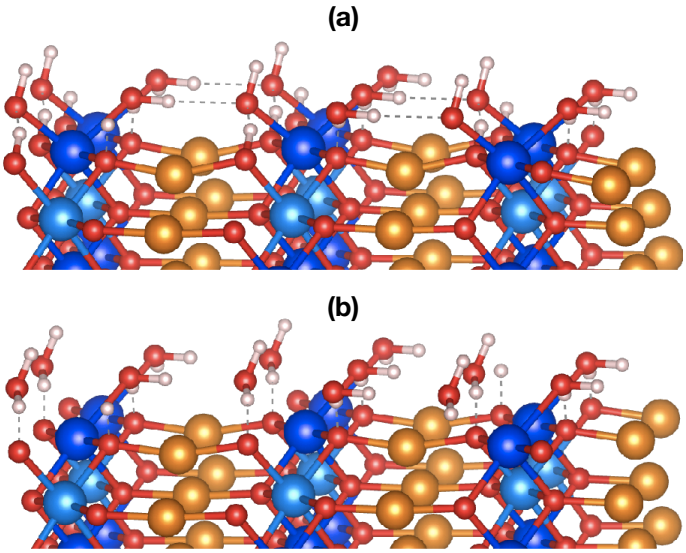

Figure 7.15

Mixed (a) and molecular (b) adsorbtion model of water on the $(11\bar{2}0)$ surface.

the surface, such that two molecules are adsorbed on each Fe site, and another one with a mixed adsorption on each Fe site. We run two different AIMD simulations, monitoring the number of dissociated water molecules on the surface to study the most favorable absorption state.

In the top panel of Figure 7.16 we report the percentage η of dissociated water molecules, among those added manually on the surface, as a function of the time of the simulation. The mixed adsorption model is stable along the simulation, without any occurrence of a second dissociation on any site, in agreement with the static calculations. Conversely, in the model with two molecularly adsorbed water molecules, the number of dissociated molecules increases over time, tending towards the mixed absorption condition. This indicates that the barrier to dissociate water at the surface is very small and that the mixed absorption is energetically favorable, despite the static calculations in vacuum provide similar absorption energies for the two models.

To further confirm this last statement, we computed the total energies of the two simulations as a function of time of the simulation. In the bottom panel, the total energies of the two simulations as a function of time are reported. The zero of the energy is set on the average energy of the mixed model along the simulation, neglecting the first 3 ps of equilibration. The average energy of the model with two adsorbed molecules is higher than the mixed model, and the difference becomes thinner as the simulation proceeds, as the two structures become more and more similar. In particular,

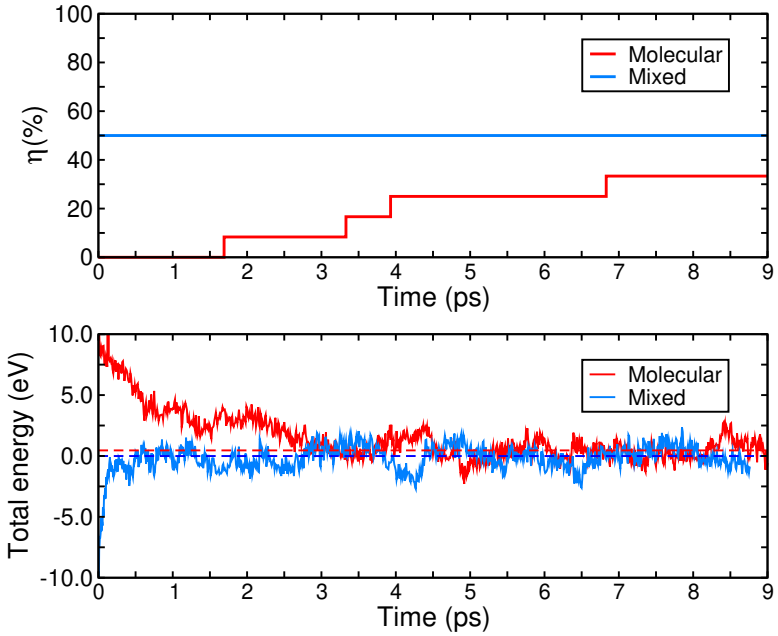

Figure 7.16

Fraction of dissociated water molecules at the CFO($11\bar{2}0$) surface (top panel) and total energy (bottom panel) for two different adsorption models as a function of the simulation time

.

considering the range between 3 and 9 ps, the average energy difference between the two models is 0.46 eV, with an uncertainty of 0.01 eV. Therefore, we considered the mixed adsorption model as representative of the interaction between the ($11\bar{2}0$) surface of CFO and water.

The histogram relative to the dipole distribution is reported in Figure 7.17. We further separate the contribution of the adsorbed and the dissociated water molecules, in this last case the dipole is referred to the OH^* group. The dipole of the molecularly adsorbed water molecules forms angles larger than 90° with the z axis, indicating that in this case the hydrogen atoms point away from the surface, bringing a dipole moment opposite to that of the (0001). Conversely, the two yellow peaks at 60° and 70°, corresponding to the dissociated water molecules, indicate that the hydrogen of the OH groups are mainly directed toward the surface.

The average electrostatic potential profile is reported in Figure 7.18. We found an electrostatic potential difference across the interface of 6.77 ± 0.03 eV, which is 0.15 eV lower than the value obtained for the (0001) surface. Consequently, the alignment procedure, reported in Figure 7.19 provides values of the VBM and the CBM 0.15 eV higher than before, namely at $+0.67 \pm 0.03$ V and -0.80 ± 0.02 V versus SHE, respectively.

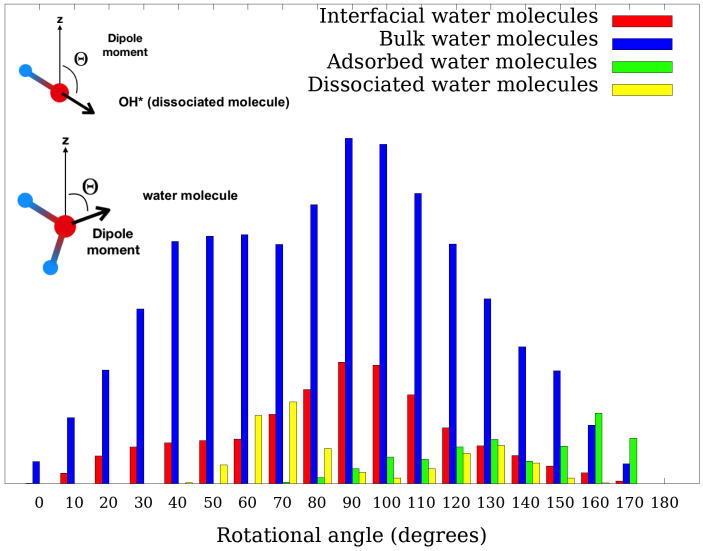

Figure 7.17

Histogram of the distribution of the angle between the dipole moment of water molecules and the z axis (see inset) for the interfacial (red), bulk (blue), molecularly (green) and dissociatively (yellow) adsorbed water molecules, computed from the molecular dynamics simulation of the CFO($11\bar{2}0$) interfaced with water.

.

Comparing the position of the band edges obtained from the two simulations, the band edges relative to the ($11\bar{2}0$) are 0.15 eV higher in energy, then an electron in the CBM would have a larger overpotential to drive the HER. However, if the electrode exposes different facets, this difference in the position of the band edges could result in an anisotropic charge separation, with the photogenerated charge carriers that migrate towards a surface with a lower CBM [222]. It has been reported that a gradient of 0.2 eV in the workfunction between two different facets is sufficient to drive the anisotropic charge separation [222]. This means that a photoexcited electron will likely tend to move towards the (0001) termination, discouraging the ($11\bar{2}0$).

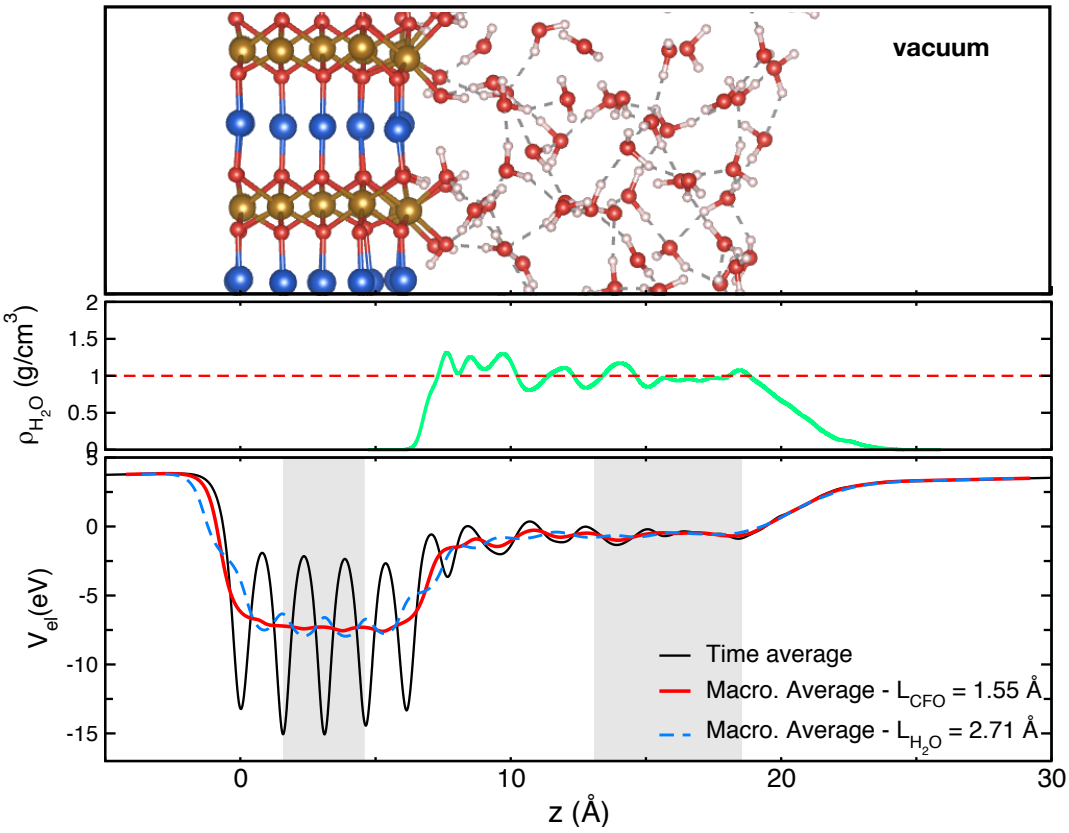

Figure 7.18

Interface between the $(11\bar{2}0)$ surface and water with the mixed adsorption state (top panel), Water density profile (middle panel) and electrostatic potential across the interface (bottom panel). The grey areas indicate the regions from which we extracted the average electrostatic potential of CFO and water.

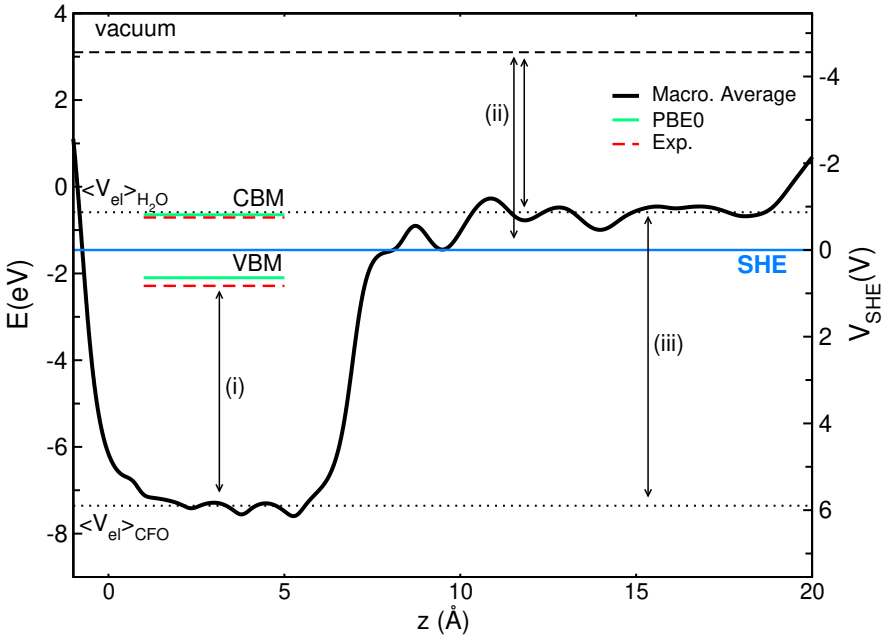

Figure 7.19

Band edges alignment of CFO w.r.t. the SHE, when the $(11\bar{2}0)$ surface is interfaced with liquid water. The band edges at point (i) are those of the bulk delafossite phase of CFO, computed at the PBE0 level. The position of the vacuum and the SHE level w.r.t. the average electrostatic potential of water (ii) were taken from the literature [218], while the alignment of the electrostatic potentials (iii) was computed via an AIMD simulation.

.

7.7 Band alignment under illumination

After the investigation of the surface in contact with water in dark conditions, the aim of this section is to predict a thermodynamically stable surface coverage under illumination. To this end, we introduce a simple model to link the stable phases in the Pourbaix diagram with the chemical potential of the electrons under illumination.

First of all, we assume that the electron-hole pairs are generated by the absorption of photons in the bulk region and the holes recombine with electrons coming from the external circuit, while the photoexcited electrons drift towards the surface, driven by the band bending. When the electrons reach the surface, their potential corresponds to the potential of the CBM at the interface with the electrolyte, i.e. the conduction band edge. In practical calculations, we cannot simulate the band bending, so we just assume to have a reservoir of electrons at the potential of the conduction band edge, which is the same throughout the slab. In doing this approximation, we are neglecting the possible formation of polaronic states in the gap and we are implicitly considering a high density of photogenerated electrons, such that the electron quasi-Fermi level is at the potential of the CBM. In the best case scenario, all the photogenerated electrons are able to reach the surface without recombination and they interact with protons present in solution to form adsorbates in compliance with the Pourbaix diagram. These electrochemical reactions involving electrons and protons, have been modelled with the CHE approach. [108]

The adsorption of H^* creates surface dipoles which could modify the electrostatic potential alignment between CFO and water. Consequently, the potential of the CBM could change in such a way to allow a transition in another phase of the Pourbaix diagram. In order to find a thermodynamically stable phase under illumination, we looked for self-consistency between the position of the CBM relative to a specific phase and the stability of that specific phase, as predicted by the Pourbaix diagram at the potential corresponding to the CBM. Once the self-consistency is achieved, the CBM does not have enough overpotential to absorb further hydrogen atoms and switch to a different absorption state. However, this model, based on thermodynamics considerations, neglects any kinetic component, which play a fundamental role in the adsorption processes and the presence of high barriers may inhibit some transitions.

The conduction band minima computed for selected phases following the method outlined in the previous section are reported in the small boxes beside each Pourbaix

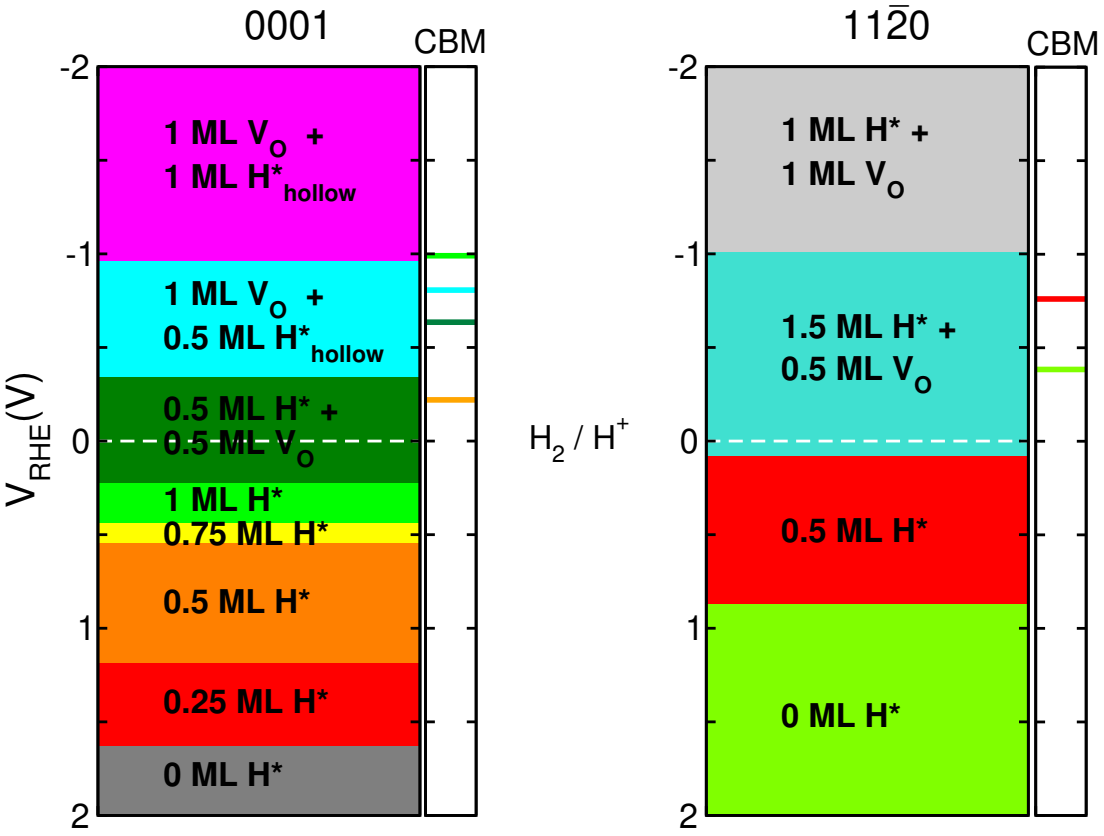

Figure 7.20

Surface Pourbaix diagram of the CFO(0001) (left) and CFO(11$\bar{2}$0) (right) surfaces, showing the potential-dependent surface coverage. The small box beside each diagram represents the position of the CBM of selected structures, shown using the same color-code as the main diagram.

diagram in Figure 7.20, using the same color code as in the main diagram, while a comparison between the bands in vacuum and in water is shown in Figure 7.21.

The CBM of the (0001) surface in dark conditions (orange line) has enough overpotential to drive the adsorption of a full ML of H* and then to create 0.5 ML of oxygen vacancies. However, this surface (dark green) does not reach the required self-consistency, as its conduction band lies in correspondence with the stability region of the surface with a 1 ML of oxygen vacancies and 0.5 ML of hydrogen adsorbed on the hollow sites. The CBM of this configuration complies with the self-consistency criterion, as the conduction band falls within the range of potentials in which the surface is stable. The thermodynamically stable surface under illumination predicted by this model differs from the surface in dark conditions by the presence of 1 ML of oxygen vacancies, and by the adsorption of hydrogen atoms in these vacancy sites (hollow sites with respect to the three surrounding Fe atoms). The main difference between the hydrogen

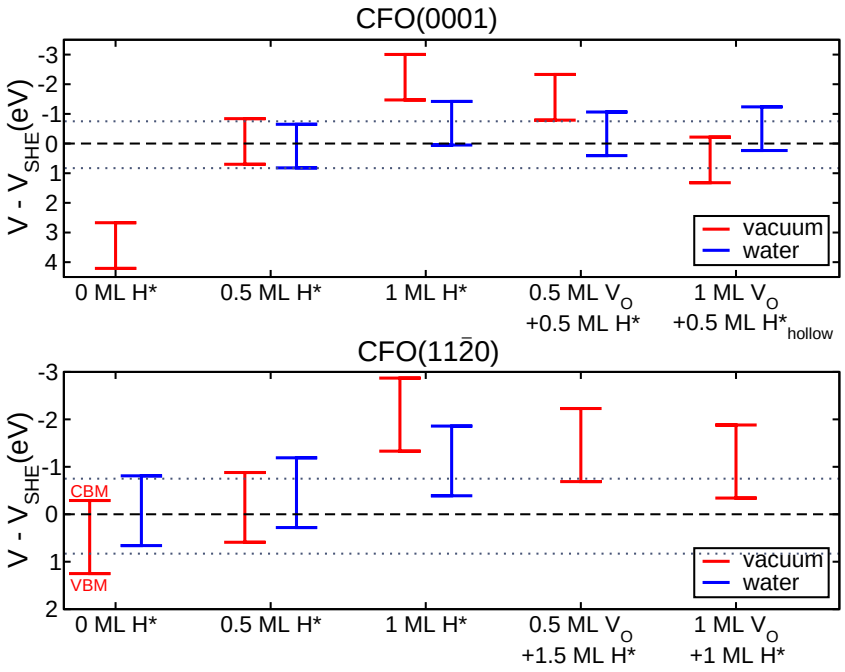

Figure 7.21

Band edges position in vacuum and in water at different adsorption states for the CFO(0001)(top panel) and CFO(11$\bar{2}$0) (bottom panel) surface. The horizontal lines indicate the position of the valence and conduction band and the vertical line the energy gap. The dashed and the dotted lines represent the SHE level and the experimental band edges at flatband conditions, respectively.

.

atoms in the hydroxyl groups and in the hollow sites resides in their charge state. While the Bader charge of the hydrogen atoms adsorbed on the oxygen sites is 0.00 (H^+), the charge of the hydrogen in the hollow sites is 1.49, indicating that the latter are negatively charged hydride species (H^-). Hydride species formed at the oxygen vacancy site were predicted theoretically and observed experimentally on Rh-doped TiO_2[223], with values of Bader charge on H^-, 1.34, in line with our results. The formation of negatively charged hydrogen adsorbates is particularly intriguing, since hydride species could lead to facile H_2 production, reacting with a proton in solution ($H^- + H^+ \rightarrow H_2$).

The CBM of the (11$\bar{2}$0) surface with 0 and 0.5 ML H* falls within the stability region of the configuration with 0.5 ML of oxygen vacancies and full coverage of the surface and subsurface oxygen. However, we did not run the AIMD simulations for the (11$\bar{2}$0) surface with oxygen vacancies to reach the self-consistency, as the highly distorted structure and the huge number of possible ways of orienting the water molecules would require a large

structural prediction work and a long AIMD simulation in order to adequately sample the canonical ensemble. However, we can make quantitative considerations based on the trend of the bands in vacuum and in the (0001) surface, reported in Figure 7.21.

The highest CBM energy is obtained for the full coverage of H^*, and the value tends to decrease as the density of oxygen vacancies increases. The two stable phases at negative potential have a similar distorted structure, in which the surface cations, due to oxygen vacancies, migrate towards the subsurface layer, and a high H^* coverage, differing for a 0.5 ML of OH groups. Given the high number of OH groups, and related dipoles, on the surface with 0.5 ML V_O and 1.5 ML H^*, one can imagine that the CBM lies higher than the boundaries of the stability region of the surface, -1 V, considering also that in vacuum the CBM lies at 2 eV. In this case, the surface with 1 ML V_O and 1 ML H^* would be the self-consistent one, provided that its conduction band is in a favorable position. If the CBM falls below -1 V, following the trend of the bands in the vacuum, there would be a continuous evolution between the two surfaces.

7.8 Incremental Gibbs free energy of adsorption of atomic hydrogen

One of the critical factors determining the catalytic activity of a material for a specific reaction is the binding energy of reaction intermediates. [224] According to the Sabatier principle [224], if an intermediate state binds too weakly, it will be difficult to activate the reaction, and if, conversely, it binds too strongly, there will be a high barrier to overcome to go from the intermediate to the final state. In the case of HER, a good descriptor of catalytic activity of an electrode is thus the incremental Gibbs free energy for hydrogen adsorption:

$$\Delta G^{\text{incr}}_{H^*} = G_{\text{slab}+(N+1)H} - \left(G_{\text{slab}+NH} + \frac{1}{2} G_{H_2,\text{mol}} \right) , \tag{7.16}$$

which provides a measure of the energy cost/gain to add one extra hydrogen adsorbate to the surface. In a metallic electrode at zero potential the initial state ($H^+ + e^-$) and the final state ($\frac{1}{2}H_2$) have the same free energy and a good catalysts should create an intermediate state with $\Delta G^{\text{incr}}_{H^*} \sim 0$, [225] in order not to create thermodynamic barriers for the adsorption or the desorption process. The catalytic activity plotted as a function of the binding energy gives rise to the well-known volcano-plot, in which platinum lies on top, with $\Delta G^{\text{incr}}_{H^*} \sim 0$ and the highest activity. [110, 226, 227]

The main difference between metallic electrodes and semiconducting photoelectrodes

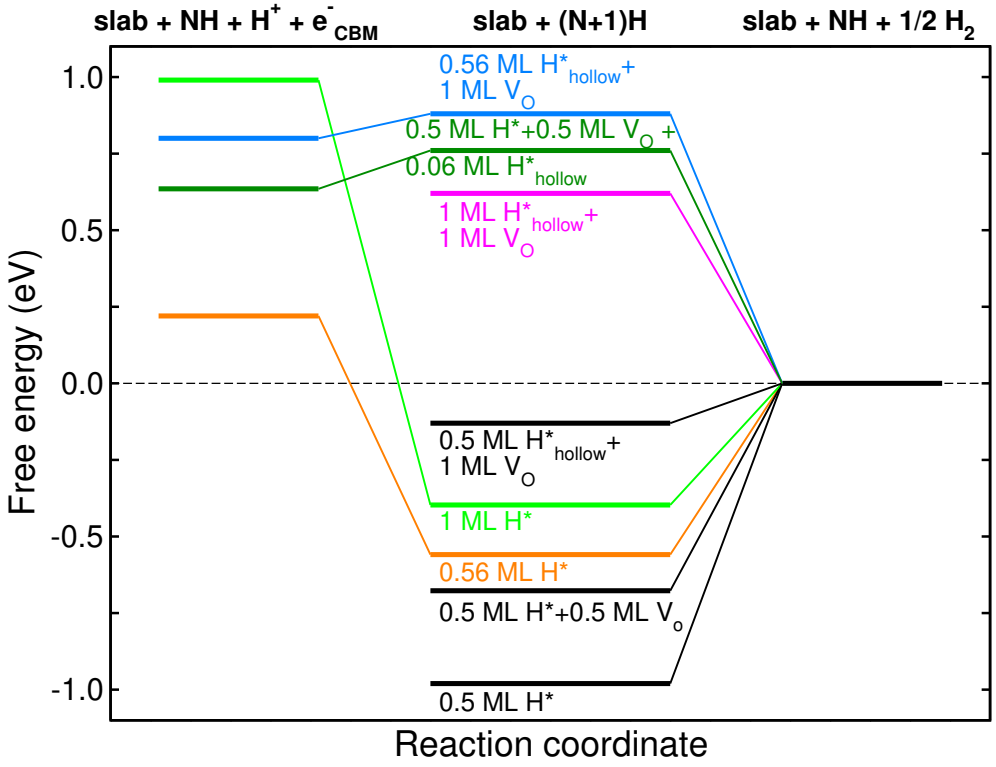

Figure 7.22

Free-energy diagram for hydrogen evolution on the CFO(0001) surface. The color code of the initial state is the same as in Figure 7.20, namely: 0.5 ML H* (orange), 1 ML H* (green), 0.5 ML H* + 0.5 ML V_O (dark green), 0.5 ML H_{hollow} + 1 ML V_O (light blue).

resides in the relative free energy of the states involved in the HER reaction. In a semiconducting photoelectrode, the free energy of the initial state, in which the electron lies at the conduction band, is higher than the one of the final state by a quantity $e\,V_{CBM}$(RHE). In this case, a good photocatalysts is the one that creates an intermediate state whose incremental free energy lies between the potential of the conduction band and zero, in such a way that no thermodynamic barriers are created.

We computed the incremental free energies $\Delta G^{\text{incr}}_{H^*}$ adding one hydrogen atom to the stable phases of the Pourbaix diagrams, and the resulting values are used to construct the free energy diagrams in Figure 7.22 (0001) and Figure 7.23 ($11\bar{2}0$).

The reaction coordinate describes the energetics of the proton discharge (Volmer step) followed by the desorption of molecular hydrogen. In the initial state, we considered a proton in solution and an electron lying in the CBM of the structures computed in the previous section, which are reported with the same color code as in Figure 7.11. In the intermediate state, an additional hydrogen atom is adsorbed on the surface, with

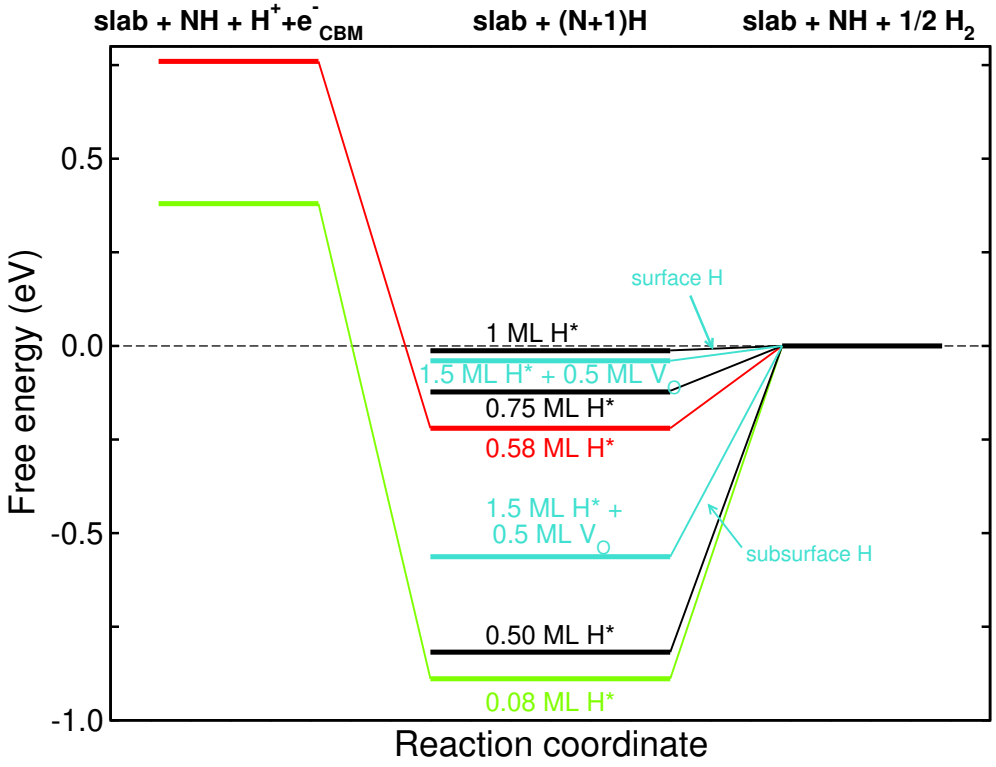

Figure 7.23

Free-energy diagram for hydrogen evolution on the CFO($11\bar{2}0$) surface. The color code of the initial state is the same as in Figure 7.20, namely: 0 ML H* (green), 0.5 ML H* (red), 1.5 ML H* + 0.5 ML V_O (turquoise).

a corresponding variation in coverage of 0.06 ML and 0.08 ML for the (0001) and the ($11\bar{2}0$) surface, and in the final state it desorbs from the surface in the form of 1/2 H_2. At this stage, we investigated the desorption also from additional coverage conditions, removing one hydrogen atom from structures for which we did not compute the potential of the CBM. We set the free energies of the final state of each configuration to zero, in such a way that the free energy of the intermediate state is $\Delta G^{\text{incr}}_{H^*}$, according to Eq.(7.16), while the free energy of the initial state, if present, is $e\,V_{CBM}$(RHE).

When the H* coverage of the intermediates on the (0001) surface is lower than 0.5 ML there is a large barrier for hydrogen desorption, due to the strong O-H bond, indicating that the low-coverage configurations are not effective for the hydrogen production. In particular, $\Delta G^{\text{incr}}_{H^*}$ at half coverage conditions is about -1 eV for the (0001) surface and even lower for lower H* coverage.

The half coverage condition guarantees the maximum possible spacing between the hydroxyls and an additional hydrogen atom adsorbed on the surface will necessarily feel

the repulsion of the neighboring adsorbates, reducing its binding strength. Moreover, the addition of a hydrogen atom causes the reduction of a surface Fe^{3+} to Fe^{2+} and the consequent electrostatic interaction. Indeed, there is a variation of ~ 0.5 eV in $\Delta G^{\text{incr}}_{H^*}$ when the H* coverage of the intermediates changes from 0.5 ML to 0.56 ML.

The orange path in Figure 7.22 represents the free energy path of the HER on the (0001) surface starting from half coverage conditions. The proton discharge is energetically favorable with a free energy variation of -0.77 eV, yet the hydrogen desorption is still the limiting step, with a free energy cost of 0.55 eV. The same situation also occurs for a full H* coverage (green line), for which $\Delta G^{\text{incr}}_{H^*}$ is -0.4 eV. In this case, we have assumed that the potential of the CBM does not change appreciably for small coverage variations, hence the CBM of the initial state, with 0.94 ML H*, is taken as the CBM computed for the structure with 1 ML H*.

The hydrogen in the surface hydroxyl groups are then bound too strongly and therefore introduce a sizable barrier for desorption of H_2 on the (0001) surface, even in the presence of oxygen vacancies as in the 0.5 ML H* + 0.5 ML V_O surface. In this specific case the hydrogen in the OH group is even more bound compared to the full H* condition, due to the presence of a smaller number of adsorbates.

Conversely, the hydrogen atoms adsorbed on the hollow sites show better catalytic activity. Indeed, the proton discharge on a hollow site on the surface with 0.5 ML H* + 0.5 ML V_O (dark green path) exhibits a free energy difference of 0.15 eV, while the desorption of H_2 is thermodynamically downhill. Similarly, on the surface with 1 ML V_O and 0.5 ML H^*_{hollow} (light-blue path) there is an energetic cost of 0.1 eV for the Volmer step, and a favorable desorption free energy, -0.88 eV. Moreover, considering this surface as the intermediate state, the incremental free energy of removing one hydrogen is -0.13 eV, thus indicating the presence of a weak bond that creates a small thermodynamic barrier for the desorption. The hydrogen atoms adsorbed in the hollow sites do not have a strong bond as in the OH group and the fact that the thermodynamically stable surface under illumination, with 1 ML V_O and 0.5 ML H^*_{hollow}, has also a favorable kinetics is encouraging for using CFO as a photocathode. We also computed $\Delta G^{\text{incr}}_{H^*}$ for full H^*_{hollow} conditions, obtaining 0.62 eV, yet the stability region of this surface lies higher in the Pourbaix diagram.

In Figure 7.23, the green path represents the HER on the pristine $(11\bar{2}0)$ surface. The hydrogen desorption is still the limiting step also for this surface, with a thermodynamic barrier of 0.9 eV. Under the same stoichiometric conditions, $\Delta G^{\text{incr}}_{H^*}$ of the (0001) surface at 0.56 ML H* is -0.55 eV, indicating a stronger binding energy in the $(11\bar{2}0)$ surface.

When the H* coverage exceeds 0.5 ML, $\Delta G^{\text{incr}}_{H^*}$ lies between -0.25 eV, 0.58 ML, and

-0.01 eV, at full H* coverage conditions. Oppositely to the (0001), in the $(11\bar{2}0)$ surface the hydrogen atoms in the OH groups have a suitable $\Delta G_{H^*}^{\text{incr}}$ to drive the HER since they do not introduce large thermodynamic barriers neither for adsorption of H*, nor for desorption of H_2. Beside the repulsion between the adsorbates, a possible source of this low $\Delta G_{H^*}^{\text{incr}}$ is the energy cost to reduce the Fe^{3+} ions in the subsurface layers into Fe^{2+} after the complete reduction of the surface Fe ions at half coverage conditions.

In the surface with 0.5 ML of oxygen vacancies and 1.5 ML of H*, the catalytically active hydrogen atoms are bound to surface oxygen with a binding energy of -0.03 eV, while those bound to the subsurface oxygen have a higher binding energy (-0.57 eV). The binding energy of the remaining structure in the Pourbaix diagram, with 1 ML of oxygen vacancies and a full H* coverage, lies around 2 eV and it is not reported in the free energy diagram.

This approach allowed us to calculate which are the most catalytically active hydrogen atoms in the HER process. According to this model, the photo-driven HER on the thermodynamically stable surface of CFO takes place through H* intermediates that display close to ideal $\Delta G_{H^*}^{\text{incr}}$. This suggests that the catalytic step of HER might not be the culprit for the poor performance of CFO as a photocatalyst for HER.

A possible limitation of this model concerns the fact that we have considered the CBM as the potential at which the photogenerated electrons lie in the initial state. In the presence of polaronic or defect states within the energy gap, the photoexcited electrons may lie in these states rather than in the CBM, thus providing a lower overpotential for drive the HER. Polaronic states originating from Fe^{3+}/Fe^{2+} reduction have indeed been suggested as limiting factors in CFO [12], leading to Fermi level pinning in the bulk. In this case, the photovoltage would be lower compared to the one estimated from the position of the CBM, and the band bending would be reduced, hindering the charge carriers separation.

Moreover, the incremental free energies were calculated by removing a hydrogen atom from the surface exposed to the vacuum, thus neglecting the effect of the solvent. Although it is common to use the free energy differences computed in vacuum [228], the solvent could have a small but not negligible effect in the calculation of the binding energies. [109]

7.9 Summary

In summary, we found that the pristine $(11\bar{2}0)$ is the surface with the lowest surface energy in the region in which the bulk delafossite phase of CFO is stable. We characterized the structural properties and the electronic structure of the most stable surfaces in the phase diagram, highlighting the mechanisms of stabilization of the polar (0001) termination.

We constructed the surface Pourbaix diagram, to study the coverage of adsorbed hydrogen atoms as a function of the electrochemical potential of the electron reservoir, from which we predicted the most stable adsorption states in dark conditions and under illumination.

We analyzed the explicit interface with water through AIMD simulations, from which we gained information about the water orientation and the electrostatic potential difference. Finally, from the free energy diagram we determined the catalytically active hydrogen on the two surfaces.

8

Conclusions and outlooks

In this thesis we have performed a theoretical characterization, in the framework of DFT, of the delafossite $CuFeO_2$ as a photocathode in PEC water splitting cells.

We characterized the electronic structure of CFO showing the pros and the cons of the adopted exchange-correlation functionals. First, we have verified the well known failure of PBE in reproducing the semiconducting character of CFO. Then, we added the Hubbard U correction in the exchange-correlation functional, computing the self-consistent value using the linear response approach, in order to remove any arbitrariness in the choice of the parameter. Overall, this approach recovers the semiconducting character of the material, yet it underestimates the bandgap and predicts an unphysical collapsing of the Fe 3d t_{2g}-e_g manifolds in the conduction band. Finally, we employed hybrid functionals, finding that PBE0 reproduces correctly the electronic structure of CFO when the fraction of exact exchange is set to its optimal value, which corresponds to the reciprocal of the dielectric constant.

We characterized the thermodynamic stability of bulk CFO combining the DFT+U formalism with the *ab-initio* thermodynamic approach. We determined a range of chemical potentials of the three constituent elements for which CFO is stable against the decomposition into other Cu- or Fe-based compounds. The allowed range of chemical potentials corresponds to high temperature and low pressure conditions, far from the ambient conditions, in which CFO exists in a metastable phase. We characterized the native point defects within the stability region of the phase diagram. The most interesting finding is the prediction of a very small formation energy for the Cu antisite defect, which is consistent with the experimental coexistence with $CuFe_2O_4$ and which could be responsible for detrimental electron/hole recombination, introducing mid-gap states.

Since CFO operates as a photocathode, it is important to have a detailed understanding of its behaviour in an electrochemical environment. We found that CFO is remarkably stable in aqueous solution and that the experimental conditions of applied potential and pH for which CFO does not show decomposition signs are consistent with the boundaries of its thermodynamic stability region.

We performed a thermodynamic screening and characterization of the (0001) and the $(11\bar{2}0)$ facets of CFO, considering different terminations and evaluating the phase diagram, from which we identified the surfaces with the lowest formation energy, compatibly with the stability region of the bulk phase. Among them, the pristine $(11\bar{2}0)$ and a Fe/O terminated (0001) surface represent our best candidates for modelling CFO as a photoelectrode.

We first investigated the interaction of these surfaces with the electrolyte in terms of hydrogen adsorption, as an intermediate step of the HER. From the surface Pourbaix diagrams we inferred the most stable adsorption states in dark conditions under flatband potential. The AIMD simulations proposed in this work provide a realistic description of the dynamics at the interface. We investigated quantities that are not directly experimentally accessible, such as the structure of the double layer formed at the interface. While the interaction between water and the (0001) surface occurs mainly via hydrogen bond, on the $(11\bar{2}0)$ termination the undercoordinated Fe atoms adsorb two water molecules according to a mixed molecular-dissociative adsorption. The band-edge positions for both surfaces were in line with the experimental measurements at flatband potential.

We predicted a thermodynamically stable adsorption state under illumination, looking for self-consistency between the CBM of a specific structure and the stability of the structure in the Pourbaix diagram. The most stable surfaces predicted by our model under illumination differ from those in dark conditions for a different hydrogen coverage. Finally, as a descriptor of the catalytic activity, we computed the binding energy of hydrogen atoms adsorbed on the surfaces at different coverage conditions. In the (0001) surface the hydrogen atoms adsorbed on the oxygen sites are strongly bound, hence not catalytically active, while those adsorbed as hydride species on the hollow sites in presence of oxygen vacancies have a favorable kinetics, with a small barrier only for the adsorption process. Measurements able to detect these changes in oxidation state, such as *in-operando* core-level X-ray spectroscopy, would be instrumental in validating our findings. Hydrides were detected on Rh-doped TiO_2 using vibrational spectroscopy [223], suggesting that this technique could be applicable to CFO as well.

Conversely, in the $(11\bar{2}0)$ the hydrogen in the surface hydroxyl groups are catalytically active, with a binding energy around zero. The fact that the thermodynamically stable surfaces under illumination have also a favorable catalytic activity is a promising result which deserves to be further explored.

First of all, we are currently investigating how the presence of at least one layer

of explicit solvent changes the incremental Gibbs free energy for hydrogen adsorption/desorption.

Moreover, the hydrogen adsorption may introduce mid-gap states that generate Fermi-level pinning. We cannot directly simulate the Fermi-level pinning effect but, in this sense, static hybrid functional calculations performed on top of the relaxed geometries should give better insights than DFT+U on the electronic structure and the density of states within the gap.

The study of the kinetics of the processes is another key factor for a complete picture of the HER on CFO. Our model is based only on thermodynamic considerations, and we just introduced the incremental Gibbs free energy as a kinetic descriptor. However, a measure of kinetic barriers through NEB calculations is a more solid factor in determining the catalytic activity. The activation barriers can also be employed in microkinetic models to investigate which are the limiting processes.

We also plan to employ NEB or metadynamics calculations to study which HER mechanism among the Volmer-Heyrovsky and Volmer-Tafel is kinetically favorable on CFO surfaces.

Bibliography

[1] M. Ferri, J. Elliott, M. Farnesi Camellone, S. Fabris, S. Piccinin, *The Journal of Physical Chemistry C* **2019**, *123*, 29589–29598.

[2] M. Ferri, J. Elliott, S. Fabris, S. Piccinin, *Phys. Rev. B* **2020**, *101*, 155201.

[3] N. S. Lewis, G. Crabtree, A. J. Nozik, M. R. Wasielewski, P. Alivisatos, H. Kung, J. Tsao, E. Chandler, W. Walukiewicz, M. Spitler, R. Ellingson, R. Overend, J. Mazer, M. Gress, J. Horwitz, C. Ashton, B. Herndon, L. Shapard, R. M. Nault, *Office of Science U.S. Department of Energy* **2005**, DOI `10.2172/899136`.

[4] M. Grætzel, *Nature* **2001**, *414*, 338–334.

[5] A. J. Nozik, *Annual Review of Physical Chemistry* **1978**, *29*, 189–222.

[6] C. G. Read, Y. Park, K.-S. Choi, *The Journal of Physical Chemistry Letters* **2012**, *3*, 1872–1876.

[7] M. S. Prévot, N. Guijarro, K. Sivula, *ChemSusChem* **2015**, *8*, 1359–1367.

[8] M. S. Prévot, Y. Li, N. Guijarro, K. Sivula, *J. Mater. Chem. A* **2016**, *4*, 3018–3026.

[9] Y. J. Jang, Y. B. Park, H. E. Kim, Y. H. Choi, S. H. Choi, J. S. Lee, *Chemistry of Materials* **2016**, *28*, 6054–6061.

[10] C.-M. Jiang, S. E. Reyes-Lillo, Y. Liang, Y.-S. Liu, G. Liu, F. M. Toma, D. Prendergast, I. D. Sharp, J. K. Cooper, *Chemistry of Materials* **2019**, *31*, 2524–2534.

[11] M. S. Prévot, X. A. Jeanbourquin, W. S. Bouree, F. Abdi, D. Friedrich, R. van de Krol, N. Guijarro, F. Le Formal, K. Sivula, *Chemistry of Materials* **2017**, *29*, 4952–4962.

[12] Y. Hermans, A. Klein, H. P. Sarker, M. N. Huda, H. Junge, T. Toupance, W. Jaegermann, *Advanced Functional Materials* **2020**, *30*, 1910432.

[13] E. Becquerel, *Compt. Rend. Acad. Sci. Paris* **1839**, *9*, 561.

[14] W. H. Brattain, C. G. B. Garrett, *Bell System Technical Journal* **1955**, *34*, 129–176.

[15] H. Gerischer, *Adv. Electrochem. and electrochem. Eng.* **1961**, *1*, 139.

[16] A. Fujishima, K. Honda, *Nature* **1972**, *238*, 37–38.

[17] L. M. Peter in *Photocatalysis: Fundamentals and Perspectives*, The Royal Society of Chemistry, **2016**, pp. 1–28.

[18] B. O'Regan, M. Grätzel, *Nature* **1991**, *353*, 737–740.

[19] M. G. Walter, E. L. Warren, J. R. McKone, S. W. Boettcher, Q. Mi, E. A. Santori, N. S. Lewis, *Chemical Reviews* **2010**, *110*, 6446–6473.

[20] T. Reier, H. N. Nong, D. Teschner, R. Schögl, P. Strasser, *Advanced Energy Materials* **2017**, *7*, 1601275.

[21] S. Trasatti, *Journal of Electroanalytical Chemistry and Interfacial Electrochemistry* **1980**, *111*, 125–131.

[22] M. W. Kanan, D. G. Nocera, *Science* **2008**, *321*, 1072–1075.

[23] Z. Chen, X. Duan, W. Wei, S. Wang, B.-J. Ni, *J. Mater. Chem. A* **2019**, *7*, 14971–15005.

[24] B. Ruqia, S.-I. Choi, *ChemSusChem* **2018**, *11*, 2643–2653.

[25] Y. Wang, L. Chen, X. Yu, Y. Wang, G. Zheng, *Advanced Energy Materials* **2017**, *7*, 1601390.

[26] A. Hagfeldt, M. Gratzel, *Accounts of Chemical Research* **2000**, *33*, 269–277.

[27] K. Sivula, R. van de Krol, *Nature Reviews Materials* **2016**, *1*, 15010.

[28] S. Chen, L.-W. Wang, *Chemistry of Materials* **2012**, *24*, 3659–3666.

[29] W. A. Smith, I. D. Sharp, N. C. Strandwitz, J. Bisquert, *Energy Environ. Sci.* **2015**, *8*, 2851–2862.

[30] M. S. Prévot, K. Sivula, *The Journal of Physical Chemistry C* **2013**, *117*, 17879–17893.

[31] M. T. Mayer, *Current Opinion in Electrochemistry* **2017**, *2*, 104–110.

[32] H. Gerischer, *Journal of Electroanalytical Chemistry and Interfacial Electrochemistry* **1983**, *150*, Electronic and Molecular Structure of Electrode-Electrolyte Interface, 553–569.

[33] A. J. Bard, A. B. Bocarsly, F. R. F. Fan, E. G. Walton, M. S. Wrighton, *Journal of the American Chemical Society* **1980**, *102*, 3671–3677.

[34] S. Trasatti, *Journal of Electroanalytical Chemistry and Interfacial Electrochemistry* **1986**, *209*, 417–428.

[35] M. Kapilashrami, Y. Zhang, Y.-S. Liu, A. Hagfeldt, J. Guo, *Chemical Reviews* **2014**, *114*, 9662–9707.

[36] C. Di Valentin, G. Pacchioni, A. Selloni, *Chemistry of Materials* **2005**, *17*, 6656–6665.

[37] C. Janaky, K. Rajeshwar, N. de Tacconi, W. Chanmanee, M. Huda, *Catalysis Today* **2013**, *199*, Catalysis Today Focus Issue: Solar Fuels, 53–64.

[38] R. van de Krol, Y. Liang, J. Schoonman, *J. Mater. Chem.* **2008**, *18*, 2311–2320.

[39] D. Barreca, P. Fornasiero, A. Gasparotto, V. Gombac, C. Maccato, A. Pozza, E. Tondello, *Chemical Vapor Deposition* **2010**, *16*, 296–300.

[40] A. Kudo, K. Ueda, H. Kato, I. Mikami, *Catalysis Letters* **1998**, *53*, 229–230.

[41] Y. Matsumoto, M. Omae, K. Sugiyama, E. Sato, *The Journal of Physical Chemistry* **1987**, *91*, 577–581.

[42] J. Zhao, T. Minegishi, L. Zhang, M. Zhong, Gunawan, M. Nakabayashi, G. Ma, T. Hisatomi, M. Katayama, S. Ikeda, N. Shibata, T. Yamada, K. Domen, *Angewandte Chemie International Edition* **2014**, *53*, 11808–11812.

[43] L. Zhang, T. Minegishi, J. Kubota, K. Domen, *Phys. Chem. Chem. Phys.* **2014**, *16*, 6167–6174.

[44] W. Septina, Gunawan, S. Ikeda, T. Harada, M. Higashi, R. Abe, M. Matsumura, *The Journal of Physical Chemistry C* **2015**, *119*, 8576–8583.

[45] X. Yu, M. S. Prévot, N. Guijarro, K. Sivula, *Nature Communications* **2015**, *6*, 7596.

[46] M. Hara, T. Kondo, M. Komoda, S. Ikeda, J. N. Kondo, K. Domen, M. Hara, K. Shinohara, A. Tanaka, *Chem. Commun.* **1998**, 357–358.

[47] P. E. de Jongh, D. Vanmaekelbergh, J. J. Kelly, *Chem. Commun.* **1999**, 1069–1070.

[48] L. Y. Isseroff, E. A. Carter, *Phys. Rev. B* **2012**, *235142*, 1–7.

[49] S. Nandy, A. Banerjee, E. Fortunato, R. Martins, *Reviews in Advanced Sciences and Engineering* **2013**, *2*, 273–304.

[50] J. Gu, Y. Yan, J. W. Krizan, Q. D. Gibson, Z. M. Detweiler, R. J. Cava, A. B. Bocarsly, *Journal of the American Chemical Society* **2014**, *136*, 830–833.

[51] I. Sullivan, B. Zoellner, P. A. Maggard, *Chemistry of Materials* **2016**, *28*, 5999–6016.

[52] S. Brahms, S. Nikitine, J. Dahl, *Physics Letters* **1966**, *22*, 31–33.

[53] A. Paracchino, V. Laporte, K. Sivula, M. Grætzel, E. Thimsen, *Nature Materials* **2011**, *10*, 456–461.

[54] A. Muir, H. Wiedersich, *Journal of Physics and Chemistry of Solids* **1967**, *28*, 65–71.

[55] M. Mekata, N. Yaguchi, T. Takagi, S. Mitsuda, H. Yoshizawa, *Journal of Magnetism and Magnetic Materials* **1992**, *104-107*, Proceedings of the International Conference on Magnetism, Part II, 823–824.

[56] T.-r. Zhao, M. Hasegawa, H. Takei, *Journal of Crystal Growth* **1996**, *166*, 408–413.

[57] S. Mitsuda, N. Kasahara, T. Uno, M. Mase, *Journal of the Physical Society of Japan* **1998**, *67*, 4026–4029.

[58] W. S. Bouree, M. S. Prévot, X. A. Jeanbourquin, N. Guijarro, M. Johnson, F. L. Formal, K. Sivula, *Advanced Materials* **2016**, *28*, 9308–9312.

[59] S. Omeiri, B. Bellal, A. Bouguelia, Y. Bessekhouad, M. Trari, *Journal of Solid State Electrochemistry* **2008**, *13*, 1395–1401.

[60] T. Joshi, T. R. Senty, R. Trappen, J. Zhou, S. Chen, P. Ferrari, P. Borisov, X. Song, M. B. Holcomb, A. D. Bristow, A. L. Cabrera, D. Lederman, *Journal of Applied Physics* **2015**, *117*, 013908.

[61] P. Hohenberg, W. Kohn, *Phys. Rev.* **1964**, *136*, B864–B871.

[62] W. Kohn, L. J. Sham, *Phys. Rev.* **1965**, *140*, A1133–A1138.

[63] A. D. Becke, *The Journal of Chemical Physics* **2014**, *140*, 18A301.

[64] M. Born, R. Oppenheimer, *Annalen der Physik* **1927**, *389*, 457–484.

[65] R. Feynman, *Statistical mechanics: a set of lectures by R. P. Feynman*, Notes taken by R. Kikuchi and H. A. Feiveson. Edited by Jacob Shaham, **1972**, pp. xii + 354.

[66] D. C. Langreth, M. J. Mehl, *Phys. Rev. B* **1983**, *28*, 1809–1834.

[67] J. P. Perdew, K. Burke, M. Ernzerhof, *Phys. Rev. Lett.* **1996**, *77*, 3865–3868.

[68] A. D. Becke, *Phys. Rev. A* **1988**, *38*, 3098–3100.

[69] Y. Wang, J. P. Perdew, *Phys. Rev. B* **1991**, *43*, 8911–8916.

[70] J. P. Perdew, K. Burke, Y. Wang, *Phys. Rev. B* **1996**, *54*, 16533–16539.

[71] H. J. Monkhorst, J. D. Pack, *Phys. Rev. B* **1976**, *13*, 5188–5192.

[72] D. R. Hamann, M. Schlüter, C. Chiang, *Phys. Rev. Lett.* **1979**, *43*, 1494–1497.

[73] L. Kleinman, D. M. Bylander, *Phys. Rev. Lett.* **1982**, *48*, 1425–1428.

[74] D. Vanderbilt, *Phys. Rev. B* **1990**, *41*, 7892–7895.

[75] P. E. Blöchl, *Phys. Rev. B* **1994**, *50*, 17953–17979.

[76] D. R. Hamann, *Phys. Rev. B* **2013**, *88*, 085117.

[77] M. Schlipf, F. Gygi, *Computer Physics Communications* **2015**, *196*, 36–44.

[78] A. J. Cohen, P. Mori-Sanchez, W. Yang, *Chemical Reviews* **2012**, *112*, 289–320.

[79] J. P. Perdew, R. G. Parr, M. Levy, J. L. Balduz, *Phys. Rev. Lett.* **1982**, *49*, 1691–1694.

[80] J. P. Perdew, M. Levy, *Phys. Rev. Lett.* **1983**, *51*, 1884–1887.

[81] M. Cococcioni, S. de Gironcoli, *Phys. Rev. B* **2005**, *71*, 035105.

[82] V. I. Anisimov, I. V. Solovyev, M. A. Korotin, M. T. Czy żyk, G. A. Sawatzky, *Phys. Rev. B* **1993**, *48*, 16929–16934.

[83] S. L. Dudarev, G. A. Botton, S. Y. Savrasov, C. J. Humphreys, A. P. Sutton, *Phys. Rev. B* **1998**, *57*, 1505–1509.

[84] J. F. Janak, *Phys. Rev. B* **1978**, *18*, 7165–7168.

[85] H. J. Kulik, M. Cococcioni, D. A. Scherlis, N. Marzari, *Phys. Rev. Lett.* **2006**, *97*, 103001.

[86] A. D. Becke, *The Journal of Chemical Physics* **1993**, *98*, 1372–1377.

[87] S. Kümmel, L. Kronik, *Rev. Mod. Phys.* **2008**, *80*, 3–60.

[88] K. Kim, K. D. Jordan, *The Journal of Physical Chemistry* **1994**, *98*, 10089–10094.

[89] P. J. Stephens, F. J. Devlin, C. F. Chabalowski, M. J. Frisch, *The Journal of Physical Chemistry* **1994**, *98*, 11623–11627.

[90] J. P. Perdew, M. Ernzerhof, K. Burke, *The Journal of Chemical Physics* **1996**, *105*, 9982–9985.

[91] C. Adamo, V. Barone, *The Journal of Chemical Physics* **1999**, *110*, 6158–6170.

[92] T. Yanai, D. P. Tew, N. C. Handy, *Chemical Physics Letters* **2004**, *393*, 51–57.

[93] J. Heyd, G. E. Scuseria, M. Ernzerhof, *The Journal of Chemical Physics* **2003**, *118*, 8207–8215.

[94] A. V. Krukau, O. A. Vydrov, A. F. Izmaylov, G. E. Scuseria, *The Journal of Chemical Physics* **2006**, *125*, 224106.

[95] J. Heyd, G. E. Scuseria, M. Ernzerhof, *The Journal of Chemical Physics* **2006**, *124*, 219906.

[96] A. Alkauskas, P. Broqvist, F. Devynck, A. Pasquarello, *Phys. Rev. Lett.* **2008**, *101*, 106802.

[97] Z. D. Pozun, G. Henkelman, *The Journal of Chemical Physics* **2011**, *134*, 224706.

[98] A. Alkauskas, P. Broqvist, A. Pasquarello, *physica status solidi (b)* **2011**, *248*, 775–789.

[99] L. Hedin, *Phys. Rev.* **1965**, *139*, A796–A823.

[100] J. H. Skone, M. Govoni, G. Galli, *Phys. Rev. B* **2014**, *89*, 195112.

[101] K. Reuter, M. Scheffler, *Phys. Rev. B* **2001**, *65*, 035406.

[102] K. Reuter, M. Scheffler, *Phys. Rev. B* **2003**, *68*, 045407.

[103] J. Rogal, K. Reuter in, **2007**.

[104] National Institute of Standard and Technology, U.S. Department of Commerce, NIST-JANAF Thermochemical Tables, `https://janaf.nist.gov/`, **accessed November 12, 2019**.

[105] S. B. Zhang, J. E. Northrup, *Phys. Rev. Lett.* **1991**, *67*, 2339–2342.

[106] C. G. Van de Walle, J. Neugebauer, *Journal of Applied Physics* **2004**, *95*, 3851–3879.

[107] H.-P. Komsa, T. T. Rantala, A. Pasquarello, *Phys. Rev. B* **2012**, *86*, 045112.

[108] J. K. Nørskov, J. Rossmeisl, A. Logadottir, L. Lindqvist, J. R. Kitchin, T. Bligaard, H. Jónsson, *The Journal of Physical Chemistry B* **2004**, *108*, 17886–17892.

[109] J. A. Gauthier, C. F. Dickens, L. D. Chen, A. D. Doyle, J. K. Nørskov, *The Journal of Physical Chemistry C* **2017**, *121*, 11455–11463.

[110] J. K. Nørskov, T. Bligaard, A. Logadottir, J. R. Kitchin, J. G. Chen, S. Pandelov, U. Stimming, *Journal of The Electrochemical Society* **2005**, *152*, J23.

[111] H. A. Hansen, I. C. Man, F. Studt, F. Abild-Pedersen, T. Bligaard, J. Rossmeisl, *Phys. Chem. Chem. Phys.* **2010**, *12*, 283–290.

[112] M. García-Mota, M. Bajdich, V. Viswanathan, A. Vojvodic, A. T. Bell, J. K. Nørskov, *The Journal of Physical Chemistry C* **2012**, *116*, 21077–21082.

[113] M. Bajdich, M. García-Mota, A. Vojvodic, J. K. Nørskov, A. T. Bell, *Journal of the American Chemical Society* **2013**, *135*, 13521–13530.

[114] J. Chen, A. Selloni, *The Journal of Physical Chemistry C* **2013**, *117*, 20002–20006.

[115] X. Nie, G. L. Griffin, M. J. Janik, A. Asthagiri, *Catalysis Communications* **2014**, *52*, 88–91.

[116] H. H. Pham, M.-J. Cheng, H. Frei, L.-W. Wang, *ACS Catalysis* **2016**, *6*, 5610–5617.

[117] Y. Wu, M. K. Y. Chan, G. Ceder, *Phys. Rev. B* **2011**, *83*, 235301.

[118] J. Cheng, M. Sprik, *Phys. Chem. Chem. Phys.* **2012**, *14*, 11245–11267.

[119] I. E. Castelli, T. Olsen, S. Datta, D. D. Landis, S. Dahl, K. S. Thygesen, K. W. Jacobsen, *Energy Environ. Sci.* **2012**, *5*, 5814–5819.

[120] T. A. Pham, D. Lee, E. Schwegler, G. Galli, *Journal of the American Chemical Society* **2014**, *136*, 17071–17077.

[121] N. Kharche, J. T. Muckerman, M. S. Hybertsen, *Phys. Rev. Lett.* **2014**, *113*, 176802.

[122] V. Stevanović, S. Lany, D. S. Ginley, W. Tumas, A. Zunger, *Phys. Chem. Chem. Phys.* **2014**, *16*, 3706–3714.

[123] Z. Guo, F. Ambrosio, W. Chen, P. Gono, A. Pasquarello, *Chemistry of Materials* **2018**, *30*, 94–111.

[124] N. G. Hörmann, Z. Guo, F. Ambrosio, O. Andreussi, A. Pasquarello, N. Marzari, *npj Computational Materials* **2019**, *5*, 100.

[125] F. Ambrosio, G. Miceli, A. Pasquarello, *The Journal of Chemical Physics* **2015**, *143*, 244508.

[126] S. S. Kocha, *Journal of The Electrochemical Society* **1995**, *142*, L238.

[127] G. H. Wannier, *Phys. Rev.* **1937**, *52*, 191–197.

[128] N. Marzari, D. Vanderbilt, *Phys. Rev. B* **1997**, *56*, 12847–12865.

[129] I. Souza, N. Marzari, D. Vanderbilt, *Phys. Rev. B* **2001**, *65*, 035109.

[130] A. Scaramucci, J. Ammann, N. A. Spaldin, C. Ederer, *Journal of Physics: Condensed Matter* **2015**, *27*, 175503.

[131] D. Pasquier, O. V. Yazyev, *2D Materials* **2019**, *6*, 025015.

[132] V. R. Galakhov, a. I. Poteryaev, E. Z. Kurmaev, V. I. Anisimov, S. Bartkowski, M. Neumann, Z. W. Lu, B. M. Klein, T.-R. Zhao, *Phys. Rev. B* **1997**, *56*, 4584–4591.

[133] M. Malvestuto, F. Bondino, E. Magnano, T. T. A. Lummen, P. H. M. Van Loosdrecht, F. Parmigiani, *Phys. Rev. B - Condensed Matter and Materials Physics* **2011**, *83*, 1–5.

[134] K. P. Ong, K. Bai, P. Blaha, P. Wu, *Chemistry of Materials* **2007**, *19*, 634–640.

[135] H. Hiraga, T. Makino, T. Fukumura, H. Weng, M. Kawasaki, *Phys. Rev. B - Condensed Matter and Materials Physics* **2011**, *84*, 2–5.

[136] V. Eyert, R. Frésard, A. Maignan, *Phys. Rev. B* **2008**, *78*, 052402.

[137] Y. Zhang, E. Kan, M. H. Whangbo, *Chemistry of Materials* **2011**, *23*, 4181–4185.

[138] J. Husek, A. Cirri, S. Biswas, A. Asthagiri, L. R. Baker, *The Journal of Physical Chemistry C* **2018**, *122*, 11300–11304.

[139] P. Giannozzi, S. Baroni, N. Bonini, M. Calandra, R. Car, C. Cavazzoni, D. Ceresoli, G. L. Chiarotti, M. Cococcioni, I. Dabo, A. Dal Corso, S. de Gironcoli, S. Fabris, G. Fratesi, R. Gebauer, U. Gerstmann, C. Gougoussis, A. Kokalj, M. Lazzeri, L. Martin-Samos, N. Marzari, F. Mauri, R. Mazzarello, S. Paolini, A. Pasquarello, L. Paulatto, C. Sbraccia, S. Scandolo, G. Sclauzero, A. P. Seitsonen, A. Smogunov, P. Umari, R. M. Wentzcovitch, *Journal of Physics: Condensed Matter* **2009**, *21*, 395502 (19pp).

[140] P. Giannozzi, O. Andreussi, T. Brumme, O. Bunau, M. B. Nardelli, M. Calandra, R. Car, C. Cavazzoni, D. Ceresoli, M. Cococcioni, N. Colonna, I. Carnimeo, A. D. Corso, S. de Gironcoli, P. Delugas, R. A. DiStasio, A. Ferretti, A. Floris, G. Fratesi, G. Fugallo, R. Gebauer, U. Gerstmann, F. Giustino, T. Gorni, J. Jia, M. Kawamura, H.-Y. Ko, A. Kokalj, E. Küçükbenli, M. Lazzeri, M. Marsili, N. Marzari, F. Mauri, N. L. Nguyen, H.-V. Nguyen, A. Otero-de-la-Roza, L. Paulatto, S. Poncé, D. Rocca, R. Sabatini, B. Santra, M. Schlipf, A. P. Seitsonen, A. Smogunov, I. Timrov, T. Thonhauser, P. Umari, N. Vast, X. Wu, S. Baroni, *Journal of Physics: Condensed Matter* **2017**, *29*, 465901.

[141] J. Heyd, G. E. Scuseria, *The Journal of Chemical Physics* **2004**, *120*, 7274–7280.

[142] A. A. Mostofi, J. R. Yates, G. Pizzi, Y.-S. Lee, I. Souza, D. Vanderbilt, N. Marzari, *Computer Physics Communications* **2014**, *185*, 2309–2310.

[143] S. Mitsuda, H. Yoshizawa, N. Yaguchi, M. Mekata, *Journal of the Physical Society of Japan* **1991**, *60*, 1885–1889.

[144] F. Ye, Y. Ren, Q. Huang, J. A. Fernandez-Baca, P. Dai, J. W. Lynn, T. Kimura, *Phys. Rev. B* **2006**, *73*, 220404.

[145] G. Quirion, M. J. Tagore, M. L. Plumer, O. A. Petrenko, *Phys. Rev. B* **2008**, *77*, 094111.

[146] R. D. Shannon, D. B. Rogers, C. T. Prewitt, *Inorganic Chemistry* **1971**, *10*, 713–718.

[147] P. H. Sit, R. Car, M. H. Cohen, A. Selloni, *Inorganic Chemistry* **2011**, *50*, 10259–10267.

[148] D. M. Sherman, *Physics and Chemistry of Minerals* **1985**, *12*, 161–175.

[149] D. S. M. Dunn, Thomas M., R. G. Pearson, *Some aspects of crystal field theory*, Harper and Row, N.Y., **1965**.

[150] Z. Fang, I. V. Solovyev, H. Sawada, K. Terakura, *Phys. Rev. B* **1999**, *59*, 762–774.

[151] M.-T. Nguyen, N. Seriani, S. Piccinin, R. Gebauer, *The Journal of Chemical Physics* **2014**, *140*, 064703.

[152] L. Wang, T. Maxisch, G. Ceder, *Phys. Rev. B* **2006**, *73*, 195107.

[153] N. J. Mosey, P. Liao, E. A. Carter, *The Journal of Chemical Physics* **2008**, *129*, 014103.

[154] S. Piccinin, *Phys. Chem. Chem. Phys.* **2019**, *21*, 2957–2967.

[155] J. K. Shenton, D. R. Bowler, W. L. Cheah, *Journal of Physics: Condensed Matter* **2017**, *29*, 445501.

[156] M. Wu, Z. Li, T. Cao, S. Louie, *Nature Communications* **2019**, *10*, 2371.

[157] Y.-C. Wang, Z.-H. Chen, H. Jiang, *The Journal of Chemical Physics* **2016**, *144*, 144106.

[158] I. Solovyev, N. Hamada, K. Terakura, *Phys. Rev. B* **1996**, *53*, 7158–7170.

[159] W. E. Pickett, S. C. Erwin, E. C. Ethridge, *Phys. Rev. B* **1998**, *58*, 1201–1209.

[160] V. L. C. Jr, M. Cococcioni, *Journal of Physics: Condensed Matter* **2010**, *22*, 055602.

[161] S. Baroni, S. de Gironcoli, A. Dal Corso, P. Giannozzi, *Rev. Mod. Phys.* **2001**, *73*, 515–562.

[162] J. Sun, A. Ruzsinszky, J. P. Perdew, *Phys. Rev. Lett.* **2015**, *115*, 036402.

[163] G. Sai Gautam, E. A. Carter, *Phys. Rev. Materials* **2018**, *2*, 095401.

[164] K. T. Jacob, K. Fitzner, C. B. Alcock, *Metallurgical Transactions B* **1977**, *8*, 451–460.

[165] H.-Y. Chen, G.-W. Fu, *Applied Surface Science* **2014**, *288*, 258–264.

[166] D. Kramer, G. Ceder, *Chemistry of Materials* **2009**, *21*, 3799–3809.

[167] S. Kim, M. Aykol, C. Wolverton, *Phys. Rev. B* **2015**, *92*, 115411.

[168] R. E. Warburton, H. Iddir, L. A. Curtiss, J. Greeley, *ACS Applied Materials & Interfaces* **2016**, *8*, 11108–11121.

[169] A. Jain, G. Hautier, S. P. Ong, C. J. Moore, C. C. Fischer, K. A. Persson, G. Ceder, *Phys. Rev. B* **2011**, *84*, 045115.

[170] O. Kubaschewski, C. B. Alcock, P. J. Spencer, *Materials thermochemistry*, 6th ed., rev. and enl, Rev. ed. of: Metallurgical thermochemistry. 5th ed., rev. and enl. 1979, Oxford ; New York : Pergamon Press, **1993**.

[171] National Institute of Standard and Technology, U.S. Department of Commerce, NIST Chemistry WebBook, `https://webbook.nist.gov/chemistry/`, **accessed November 12, 2019**.

[172] J. E. Saal, S. Kirklin, M. Aykol, B. Meredig, C. Wolverton, *JOM* **2013**, *65*, 1501–1509.

[173] A. V. Khvan, O. B. Fabrichnaya, G. Savinykh, R. Adam, H. J. Seifert, *Journal of Phase Equilibria and Diffusion* **2011**, *32*, 498–511.

[174] J. Schorne-Pinto, L. Cassayre, L. Presmanes, A. Barnabe, *Inorganic Chemistry* **2019**, *58*, 6431–6444.

[175] E. A. Fugate, S. Biswas, M. C. Clement, M. Kim, D. Kim, A. Asthagiri, L. R. Baker, *Nano Research* **2019**, *12*, 2390–2399.

[176] J. Lee, S. Han, *Phys. Chem. Chem. Phys.* **2013**, *15*, 18906–18914.

[177] J. Lento, J. L. Mozos, R. Nieminen, *Journal of Physics: Condensed Matter* **2002**, *14*, 2637.

[178] T. Kimura, J. C. Lashley, A. P. Ramirez, *Phys. Rev. B* **2006**, *73*, 220401.

[179] Z. Zhou, J. Liu, R. Long, L. Li, L. Guo, O. V. Prezhdo, *Journal of the American Chemical Society* **2017**, *139*, 6707–6717.

[180] S. Kasamatsu, T. Tada, S. Watanabe, *Solid State Ionics* **2011**, *183*, 20–25.

[181] M. Sachs, E. Pastor, A. Kafizas, J. R. Durrant, *The Journal of Physical Chemistry Letters* **2016**, *7*, 3742–3746.

[182] T. Zhang, M.-Y. Wu, D.-Y. Yan, J. Mao, H. Liu, W.-B. Hu, X.-W. Du, T. Ling, S.-Z. Qiao, *Nano Energy* **2018**, *43*, 103–109.

[183] F. Lei, Y. Sun, K. Liu, S. Gao, L. Liang, B. Pan, Y. Xie, *Journal of the American Chemical Society* **2014**, *136*, 6826–6829.

[184] J. Bao, X. Zhang, B. Fan, J. Zhang, M. Zhou, W. Yang, X. Hu, H. Wang, B. Pan, Y. Xie, *Angewandte Chemie International Edition* **2015**, *54*, 7399–7404.

[185] N. Ansari, K. Ulman, M. Farnesi Camellone, N. Seriani, R. Gebauer, S. Piccinin, *Phys. Rev. Materials* **2017**, *1*, 035404.

[186] M. Pourbaix, *Atlas of Electrochemical Equilibria in Aqueous Solutions*, National Association of Corrosion Engineers, Houston, Tex, **1974**.

[187] L.-F. Huang, J. M. Rondinelli, *Journal of Physics: Condensed Matter* **2017**, *29*, 475501.

[188] D. Cubicciotti, *Corrosion* **1988**, *44*, 875–880.

[189] K. A. Persson, B. Waldwick, P. Lazic, G. Ceder, *Phys. Rev. B* **2012**, *85*, 235438.

[190] L.-F. Huang, M. J. Hutchison, R. J. Santucci, J. R. Scully, J. M. Rondinelli, *The Journal of Physical Chemistry C* **2017**, *121*, 9782–9789.

[191] X. Yang, E. A. Fugate, Y. Mueanngern, L. R. Baker, *ACS Catalysis* **2017**, *7*, 177–180.

[192] J. VandeVondele, M. Krack, F. Mohamed, M. Parrinello, T. Chassaing, J. Hutter, *Computer Physics Communications* **2005**, *167*, 103–128.

[193] S. Goedecker, M. Teter, J. Hutter, *Phys. Rev. B* **1996**, *54*, 1703–1710.

[194] O. A. Vydrov, T. Van Voorhis, *The Journal of Chemical Physics* **2010**, *133*, 244103.

[195] R. Sabatini, T. Gorni, S. de Gironcoli, *Phys. Rev. B* **2013**, *87*, 041108.

[196] G. Miceli, S. de Gironcoli, A. Pasquarello, *The Journal of Chemical Physics* **2015**, *142*, 034501.

[197] K. Ulman, E. Poli, N. Seriani, S. Piccinin, R. Gebauer, *The Journal of Chemical Physics* **2019**, *150*, 041707.

[198] G. Bussi, D. Donadio, M. Parrinello, *The Journal of Chemical Physics* **2007**, *126*, 014101.

[199] D. H. Choi, S. J. Moon, J. S. Hong, S. Y. An, I.-B. Shim, C. S. Kim, *Thin Solid Films* **2009**, *517*, The proceedings of the 1st International Conference on Microelectronics and Plasma Technology (ICMAP 2008), 3987–3989.

[200] S. Li, J. Liu, X. Wang, B. Yan, H. Li, J. Liu, *Physica B: Condensed Matter* **2012**, *407*, 2412–2415.

[201] K. Kim, H. C. Choi, B. I. Min, *Phys. Rev. B* **2009**, *80*, 035116.

[202] A. P. Amrute, Z. Łodziana, C. Mondelli, F. Krumeich, J. Pérez-Ramírez, *Chemistry of Materials* **2013**, *25*, 4423–4435.

[203] Q.-J. Liu, Z.-T. Liu, *Vacuum* **2014**, *107*, 90–98.

[204] C. Dai, X. Tian, Y. Nie, H.-M. Lin, C. Yang, B. Han, Y. Wang, *Environmental Science & Technology* **2018**, *52*, 6518–6525.

[205] P. W. Tasker, *Journal of Physics C: Solid State Physics* **1979**, *12*, 4977–4984.

[206] C.-L. Jiang, Q.-J. Liu, F.-S. Liu, Z.-T. Liu, *Current Applied Physics* **2017**, *17*, 126–129.

[207] C. Noguera, *Journal of Physics: Condensed Matter* **2000**, *12*, R367–R410.

[208] Y. Mastrikov, E. Heifets, E. Kotomin, J. Maier, *Surface Science* **2009**, *603*, 326–335.

[209] X. Li, Q. Hui, D.-Y. Shao, J.-J. Chen, C.-M. Li, N.-P. Cheng, *Comput. Mater. Sci.* **2016**, *112*, 8–17.

[210] H. Widjaja, H. A. Miran, M. Altarawneh, I. Oluwoye, H. N. Lim, N. M. Huang, Z.-T. Jiang, B. Z. Dlugogorski, *Mater. Chem. Phys.* **2017**, *201*, 241–250.

[211] Y. Jiang, Y. Shi, X. Xiang, J. Qi, Y. Han, Z. Liao, T. Lu, *Phys. Rev. Applied* **2019**, *11*, 054088.

[212] L. Wang, F. Zhou, Y. S. Meng, G. Ceder, *Phys. Rev. B* **2007**, *76*, 165435.

[213] C. Tsai, K. Chan, J. K. Nørskov, F. Abild-Pedersen, *Surface Science* **2015**, *640*, Reactivity Concepts at Surfaces: Coupling Theory with Experiment, 133–140.

[214] X. Sun, W. Zhu, D. Wu, C. Li, J. Wang, Y. Zhu, X. Chen, J. A. Boscoboinik, R. Sharma, G. Zhou, *Nature Communications* **2020**, *11*, 305.

[215] M.-T. Nguyen, N. Seriani, R. Gebauer, *The Journal of Chemical Physics* **2013**, *138*, 194709.

[216] G. Cicero, J. C. Grossman, A. Catellani, G. Galli, *Journal of the American Chemical Society* **2005**, *127*, 6830–6835.

[217] N. Kharche, M. S. Hybertsen, J. T. Muckerman, *Phys. Chem. Chem. Phys.* **2014**, *16*, 12057–12066.

[218] F. Ambrosio, Z. Guo, A. Pasquarello, *The Journal of Physical Chemistry Letters* **2018**, *9*, 3212–3216.

[219] C. G. Van de Walle, R. M. Martin, *Phys. Rev. B* **1987**, *35*, 8154–8165.

[220] A. Baldereschi, S. Baroni, R. Resta, *Phys. Rev. Lett.* **1988**, *61*, 734–737.

[221] J. T. Mefford, Z. Zhao, M. Bajdich, W. C. Chueh, *Energy Environ. Sci.* **2020**, *13*, 622–634.

[222] T. Takata, J. Jiang, Y. Sakata, M. Nakabayashi, N. Shibata, V. Nandal, K. Seki, T. Hisatomi, K. Domen, *Nature* **2020**, *581*, 411–414.

[223] S. Ida, K. Sato, T. Nagata, H. Hagiwara, M. Watanabe, N. Kim, Y. Shiota, M. Koinuma, S. Takenaka, T. Sakai, E. Ertekin, T. Ishihara, *Angewandte Chemie International Edition* **2018**, *57*, 9073–9077.

[224] P. Sabatier, *Berichte der deutschen chemischen Gesellschaft* **1911**, *44*, 1984–2001.

[225] R. Parsons, *Trans. Faraday Soc.* **1958**, *54*, 1053–1063.

[226] B. E. Conway, J. O. Bockris, *The Journal of Chemical Physics* **1957**, *26*, 532–541.

[227] J. Greeley, T. F. Jaramillo, J. Bonde, I. Chorkendorff, J. K. Nørskov, *Nature Materials* **2006**, *5*, 909–913.

[228] Q. Tang, D.-e. Jiang, *ACS Catalysis* **2016**, *6*, 4953–4961.